NASA Contractor Report 165544

SOLUTE TRANSPORT DURING THE CYCLIC OXIDATION OF Ni-Cr-Al ALLOYS

James A. Nesbitt

Michigan Technological University
Houghton, Michigan

May 1982

Prepared for

NATIONAL AERONAUTICS AND SPACE ADMINISTRATION
Lewis Research Center
Under Grant NSG-3215

TABLE OF CONTENTS

		Page
I.	INTRODUCTION	1
	Thermal Fatigue	2
	Oxidation Protection	2
	Philosophy and Approach	19
	Purpose	20
II.	EXPERIMENTAL RESULTS	22
	Procedure	22
	Experimental Results	36
	Summary	67
III.	NUMERICAL MODELING RESULTS AND DISCUSSION	69
	Numerical Modeling	69
	Results and Discussion	73
	Summary	88
IV.	CONCLUSIONS	90
APPENDICES		91
	Appendix A: Technique of Quantitative Electron Microscopy	91
	Appendix B: Effective NiCrAl Phase Diagram at 1200°C	95
	Appendix C: Diffusion Coefficients	100
	Appendix D: The Numerical Model	118
REFERENCES		134

Solute Transport During the Cyclic Oxidation of Ni-Cr-Al Alloys

by James A. Nesbitt

Michigan Technological University
Houghton, Michigan

INTRODUCTION

Most superalloys require protective surface coatings to achieve practical component lives in high-temperature, oxidizing, and corrosive environments. Continued advances in the high-temperature mechanical properties of Ni and Co based superalloys have increased their possible operating temperature to 1200°C (1). Ni or Co alone do not form oxides capable of surface protection at the elevated temperatures (2). In the past, many superalloys contained sufficient quantities of Cr to provide protective Cr_2O_3 oxide scales whereas the recent advances in the mechanical properties have come mainly at the expense of the Cr content (3). The result has been an increase in the structural stability of superalloys while the surface stability has decreased (2).

Protective coatings are generally of two types, aluminide diffusion coatings and overlay coatings. Currently, the most promising overlay coatings are alloys in the NiCrAl and CoCrAl systems (1). Both coating types provide high-temperature oxidation protection by the selective oxidation of Al. α-Al_2O_3, the high-temperature oxide phase, allows minimal transport of Al^{3+} and O^{2-} ions, thereby providing sufficient oxide protection between the metal and the environment. In general, the most important requirements for protective coatings for gas turbine superalloys are (1):

1. resistance to oxidation accompanied by thermal cycling,
2. resistance to thermal fatigue cracking, and
3. resistance to hot corrosion (for specific applications and environments).

The bulk of this report will deal with resistance to oxidation accompanied by thermal cycling. The resistance to thermal fatigue cracking will be briefly discussed below. The resistance to hot corrosion will not be considered.

Thermal Fatigue

Thermal fatigue results from mechanical strains induced in superalloy components undergoing thermal cycling. Many superalloy applications, such as jet engine turbine components, entail thermal cycling during normal use. The danger of thermal fatigue is component cracking, especially in brittle surface coatings (4). The strains are typically great enough to propagate cracks into the superalloy component (1) resulting in catastrophic failure. Hence, some ductility is required in protective coatings to resist thermal fatigue cracking.

Two-phase overlay coatings are capable of greater ductility than aluminide diffusion coatings. The surface phase of aluminide coatings is based on the intermetallic NiAl (CoAl) phase. It is unfortunate that the NiAl phase is quite brittle below approximately 700 - 900°C depending on the exact Al concentration (3,4). For many advanced airfoil designs, thermal strains can peak at low temperatures, and brittle coatings can prove to be inadequate for some applications (1). In comparison, two-phase NiCrAl (CoCrAl) overlay coatings combine the oxidation resistance of the brittle NiAl (CoAl) phase with the ductility of the Ni (Co) solid solution phase. Naturally, the ductility of the two-phase structure is dependent on the amount of the NiAl (CoAl) phase present. Therefore, two-phase overlay coatings sacrifice Al content (less NiAl phase) for the required greater ductility (1).

Oxidation Protection

Oxide protection by overlay coatings depends on the ability of the coating to supply continuously the Al necessary for Al_2O_3 formation and growth. When the Al_2O_3 oxide scale is adherent and intact, the slow ionic transport in the scale is the rate-controlling step (5), thereby fixing the overall rate of Al consumption. The ionic transport, or diffusion, in the oxide scale is dependent on the diffusivities of the ions, the interface concentrations at the

gas/oxide and oxide/metal boundaries, and the thickness of the oxide scale (6). As the scale thickens, the ions must travel greater distances, and the rate of Al consumption decreases.

Control of the oxidation rate by diffusion in the scale allows definition of a specific flux or delivery rate of Al, viz., the requisite flux. The requisite flux is the specific delivery rate of Al from the metal to the oxide required for exclusive formation and continued growth of an Al_2O_3 oxide scale.† As so defined, the requisite flux is equal to the rate of Al consumption (7) as controlled by diffusion in the oxide scale and is therefore dependent on the oxide scale thickness. When the oxide scale is thin, the requisite flux will be great; as the oxide scale thickens, the requisite flux will decrease. Oxide protection by the overlay coating is afforded when the flux of Al from the coating substrate to the oxide scale is equal to the requisite flux.

Overlay coatings when bonded to superalloy substrates undergo loss of Al by interdiffusion with the substrate (1,9). Al diffusion into the superalloy substrate effectively reduces the Al content of the coating. The degree of interdiffusion will depend on the diffusivity of Al in the superalloy substrate (9,10). If the Al diffusivity is high, more Al can be lost to the substrate than is consumed in the formation and growth of the Al_2O_3 oxide scale (11). As the Al reserves in the coating are depleted, the coating will be unable to supply the requisite flux to the oxide/coating interface, and the coating may cease to provide adequate protection (10,11).

The diffusional processes involved with the oxidation of coated superalloys may be divided into two related studies: the diffusional transport of Al to the oxide/coating interface, and the interdiffusion of Al between the coating and

---

†The requisite flux as defined above is equivalent to the ionic flux designated S as used by Wagner (8) and the "flux of Al consumed due to oxidation, J^{Al}_{oxide}" as discussed by Pettit (7).

superalloy substrate. This thesis will deal mainly with the former study, viz., the diffusion of Al to the oxide/metal interface, specifically in two-phase NiCrAl alloys.

Thermal cycling of NiCrAl alloys results in cracking and spalling of the protective Al_2O_3 oxide scale (12). The oxide cracking and spalling is a consequence of mismatch between the coefficients of thermal expansion of the oxide and the metal substrate (13,14).† Since the requisite flux is greater for thin oxide scales, the requisite flux associated with oxide spallation will be greater than if the oxide scale had remained adherent and intact. As a result, the rate of Al consumption will also be greater when cracking and spalling of the oxide scale occurs (3,15). The danger of a higher rate of Al consumption is a more rapid depletion of the Al reservoir in the two-phase region. When the alloy is unable to supply the requisite Al flux to the oxide/metal interface, the poorly protective oxides of Ni, Co, or Cr will form (7,15). This failure of the protective oxide scale is commonly referred to as breakaway oxidation (6) and occurs in many alloys where a reactive metal (as Cr, Si, or Al) is selectively oxidized to form a protective oxide scale (16,17).

The ability of the alloy to supply the requisite flux is dependent on the solute diffusivity and the concentration gradients near the oxide/metal interface. The effect of the diffusivity and the bulk alloy composition (with regard to the phase diagram) on the ability to supply the requisite flux in two-phase alloys can be illustrated most simply by reference to three theoretical binary alloys. Assume that all three alloys form the same solute oxide at the same rate so that the amount of solute consumed at any time will be the same. For simplicity, imagine the oxide to remain at a constant thickness

†In the remainder of this report, metal, metal substrate, and alloy will refer to the coating alloy unless otherwise specified.

(as results from oxide volatization or spallation occurring at the same rate as oxide growth). Therefore, the requisite flux for each alloy is constant and equal.

For the first alloy (alloy 1), consider a slab of a $\gamma + \beta$, A - B alloy where β is the B rich solute phase, and γ is the A rich solvent phase. If a slab of alloy 1 is oxidized, B will diffuse to the oxide/metal interface where it is oxidized, and a γ layer depleted of the β phase will grow inward from the metal surface. A schematic drawing of the B concentration/distance profile for two oxidation times, $t < t^*$ and $t = t^*$, is shown in Figures 1a and 1b. The initial solute concentration, C_o, and the maximum B solubility in the γ phase, $C_{\gamma\beta}$, are shown in a possible A - B phase diagram in Figure 1e. For simplicity only, the B concentration profiles in the near-surface γ layer have been drawn as straight lines. The total amount of B consumed after t^* hours can be determined as the difference between the initial B concentration profile and the B concentration profile at $t = t^*$, indicated by the cross-hatched area in Figure 1b.

The B concentration gradients at $t < t^*$ and $t = t^*$ (Figures 1a and 1b) are equal because at both times the alloy is supplying the constant requisite flux. Up to the time $t = t^*$, as the width of the layer increased, the B concentration at the oxide/metal interface could decrease, maintaining a constant B concentration gradient and supplying the constant requisite flux. But at $t = t^*$, the B concentration at the oxide/metal interface has decreased to zero (Figure 1b). As the γ-layer width continued to increase ($t > t^*$), the B concentration gradient must decrease, alloy 1 would no longer be capable of supplying the requisite flux, and the B oxide scale would fail; i.e., oxides of the solvent A would begin to form.[†]

[†]Basic thermodynamic considerations show that the A oxides begin to form

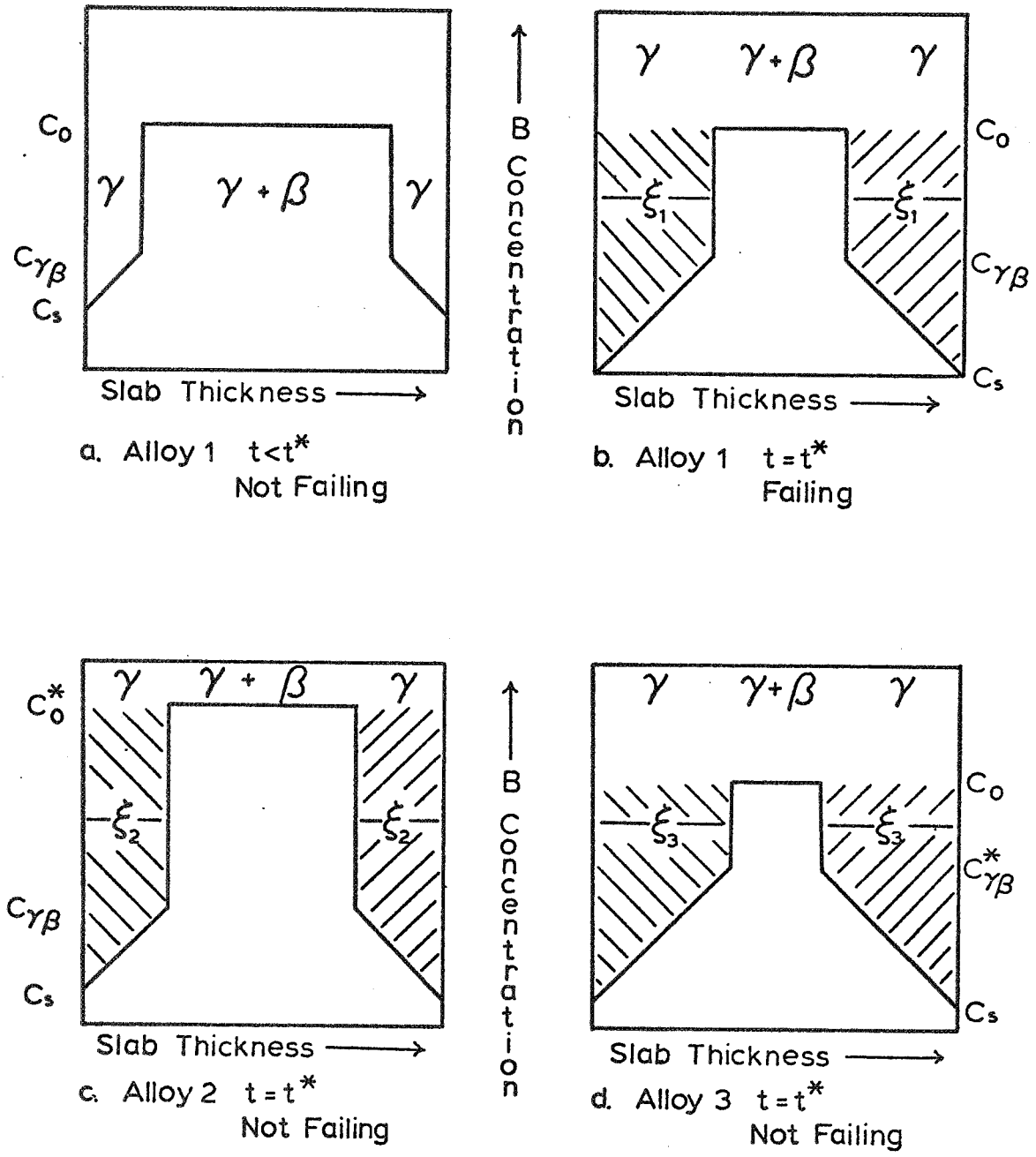

Figure 1. Oxidation of $\gamma+\beta$ Binary Alloys

All alloys form the same solute oxide at the same rate. a. Alloy 1, $t<t^*$ (C_0, $C_{\gamma\beta}$, D_1); b. Alloy 1, failing at $t=t^*$ (C_0, $C_{\gamma\beta}$, D_1); c. Alloy 2, not failing at $t=t^*$ ($C_0^*>C_0$, $C_{\gamma\beta}$, D_1); d. Alloy 3, not failing at $t=t^*$ (C_0, $C^*_{\gamma\beta}>C_{\gamma\beta}$, D_1); (cross hatched areas in b,c, and d are equal).

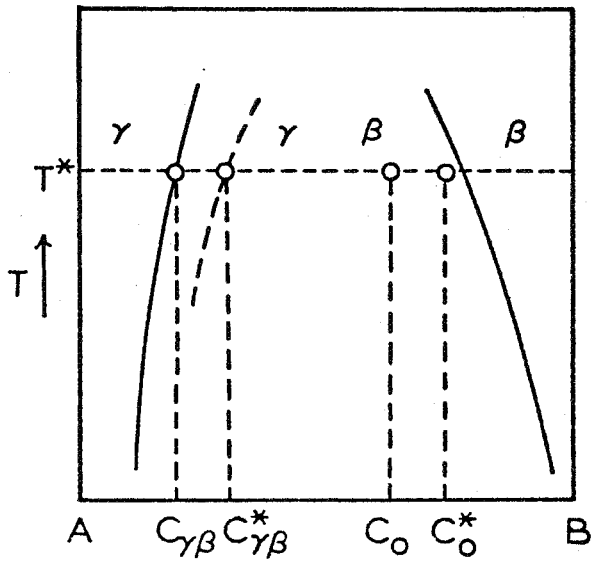

e.

Figure 1 cont.
Phase diagram for A-B binary alloys.

Increasing the diffusivity enables alloy 1 to continue to supply the requisite flux and provide a protective B oxide scale for a longer time ($t > t^*$). Doubling the diffusivity of alloy 1 would allow the B concentration gradient to be reduced by a half and yet still supply the requisite flux. At $t = t^*$, the γ-layer width of alloy 1 with twice the diffusivity would be slightly greater than that shown in Figure 1b, but the B concentration at the oxide/metal interface would be significantly greater than zero (due to the lower concentration gradient). Hence, increasing the diffusivity increases the ability of an alloy to supply the requisite flux. The drawback to an increased diffusivity is the rapid loss of solute from a coating to the metal substrate, more rapidly depleting the coating and possibly resulting in an earlier oxide scale failure ($t < t^*$).

The effect of the initial solute concentration on the solute flux can be illustrated by considering a second $\gamma + \beta$ alloy (alloy 2) with a greater B content ($C_0^* > C_0$; D, $C_{\gamma\beta}$ same as alloy 1) oxidized for t^* hours. The resulting B concentration/distance profile is shown in Figure 1c. Since the amount of B consumed is controlled by the requisite flux of the oxide scale, both alloys 1 and 2 have equal concentration gradients in the γ layer and also have lost the same amount of B at $t = t^*$ (the cross-hatched areas in Figures 1b and 1c are equal). Since ξ_2, the γ-layer width in alloy 2, is less than ξ_1, the γ-layer width in alloy 1, the B concentration at the oxide/metal interface in alloy 2 is greater than zero. Hence at $t = t^*$, alloy 2 does not exhibit breakaway oxidation but is still able to supply the requisite flux to the oxide. Therefore, increasing the solute concentration increases the protective life of

---

before the B concentration at the oxide/metal interface is equal to zero. But, for a solute with a very high affinity for oxygen (as in the case of Al in Ni or Co), the same thermodynamic considerations show that the solute concentration at the interface is many orders of magnitude less than the solvent concentration at the same interface (i.e., 1 ppm Al in Ni) (7) and may therefore be approximated as zero.

oxide scales on binary alloys.

A third alloy (alloy 3) with the same B concentration but a greater B solubility in the γ phase ($C^*_{\gamma\beta} > C_{\gamma\beta}$; C_0, D same as alloy 1) can be used to illustrate the beneficial effect of the greater B solubility. After oxidation for t^* hours, alloy 3 is still able to supply the requisite flux. The B concentration gradients in the γ layer of both alloys are equal, but the B concentration at the oxide/metal interface in alloy 3 is greater than zero (Figure 1d). The detrimental effect of the opposite change from that illustrated above for C_0, $C_{\gamma\beta}$ or D could be similarly reasoned. In a ternary alloy system, the initial solute concentration (C_0), the maximum solute concentration in the solvent phase ($C_{\gamma\beta}$), and the diffusivity (D) may all vary at the same temperature. The detrimental effect of two of the above parameters could overcome the beneficial effect of the third. For example, it is possible to envision a ternary alloy with a greater initial solute concentration failing before another ternary alloy with a lower initial solute concentration.

Oxidation studies can be arbitrarily divided into two overlapping categories, isothermal oxidation and oxidation accompanied by thermal cycling. The main emphasis of this report concerns the latter category dealing with the Al diffusion in two-phase NiCrAl alloys during oxidation accompanied by thermal cycling. Since isothermal oxidation studies provide insight to the oxidation behavior observed during the more complex cyclic oxidation,[†] the pertinent isothermal oxidation studies will be briefly reviewed before considering cyclic oxidation.

[†]Cyclic oxidation will hereafter refer to oxidation accompanied by thermal cycling.

Isothermal Oxidation

Experimental. High temperature isothermal oxidation of (Ni,Co,Fe)CrAl alloys results in the selective oxidation of Al (5,18,19). Alloys containing greater than 4 - 6 wt.%Al form external Al_2O_3 oxide scales which generally thicken parabolically with time (5,18). Since the oxide growth is controlled by diffusion in the oxide itself, there is little difference between the growth rates of external Al_2O_3 oxide scales on various base alloys (Ni,Co, or Fe) (18) or alloy composition. The differences appear negligible in comparison with the growth rates of other possible oxides (NiO, CoO, or Cr_2O_3) (3,5,18,20).

After short oxidation periods, transient oxides of Ni, Co, Fe, or Cr typically appear on the alloy surface (5,21-23). The greater the Al concentration of the alloy, the quicker the replacement of transient oxides by a continuous Al_2O_3 oxide scale. For alloys with low (less than 4 wt.%) Al concentrations, the less-protective oxides may never be fully replaced by a continuous Al_2O_3 oxide scale. When the less-protective oxides remain on the alloy surface, oxygen diffusing into the alloy internally oxidizes the Al with the resultant growth of a subscale of Al_2O_3 precipitates below the sample surface (5,18).

The transition from transient oxide formation to a continuous Al_2O_3 oxide scale and the absence of such a transition is directly related to the diffusion in the near-surface region. Alloys with high Al concentrations are rapidly able to develop large Al concentration gradients and supply the relatively high Al flux necessary to establish an external scale of Al_2O_3. In comparison, alloys with less than 4 - 6 wt.%Al cannot develop the flux necessary for formation of an external layer of Al_2O_3. Internal oxidation of Al occurs below the less-protective oxides (5,18). The denser the Al_2O_3 precipitation in the subscale layer, the more tortuous the path the incoming oxygen must travel,

and the greater the chance of formation of a continuous Al_2O_3 layer below the subscale region. If a significantly large volume fraction of Al_2O_3 precipitates is deposited at the subscale/metal interface, the Al_2O_3 precipitates may "link up," forming a continuous Al_2O_3 layer (5,24). If a continuous layer of Al_2O_3 is not formed, continued internal oxidation essentially depletes the alloy of free Al. The resulting oxidation rate is relatively high, being associated with the less protective oxides Cr_2O_3, NiO, CoO (5,18), etc. Oxide maps, experimentally determined, indicate regions of specific oxide control on isotherms of the ternary phase diagram. Oxide maps for the NiCrAl system at 1200°C (5) showing regions of Al_2O_3, Cr_2O_3, NiO, and spinel oxide formation are shown in Figure 2.

Small additions of reactive metals (as Y and Zr) greatly increase the Al_2O_3 oxide scale adherence of (Ni,Co,Fe)CrAl alloys (19,25-27). Most proposed coating alloys for high-temperature use, therefore, contain various amounts (< 1 wt.%) of these metal additions. Various proposed mechanisms to account for the increased adherence have been discussed elsewhere (19,25,28-31). Numerous isothermal oxidation tests have shown that the reactive metal additions can significantly affect the oxidation rate (19,25,27). Oxide stringers growing from the oxide scale into the metal substrate are observed on oxidized alloys containing reactive metal additions. The origin or cause of the oxide stringers is unclear for Zr-containing alloys where no enrichment of Zr is observed (27). The oxide stringers observed in Y-containing alloys are attributed to the preferential oxidation of grain boundary yttrides (19,25,28,29).

Theoretical. A theoretical solute concentration/distance profile for oxidized alloys can be predicted by an appropriate solution to Fick's second law subject to two boundary conditions. One boundary condition may be the initial solute concentration in single-phase alloys or an interface

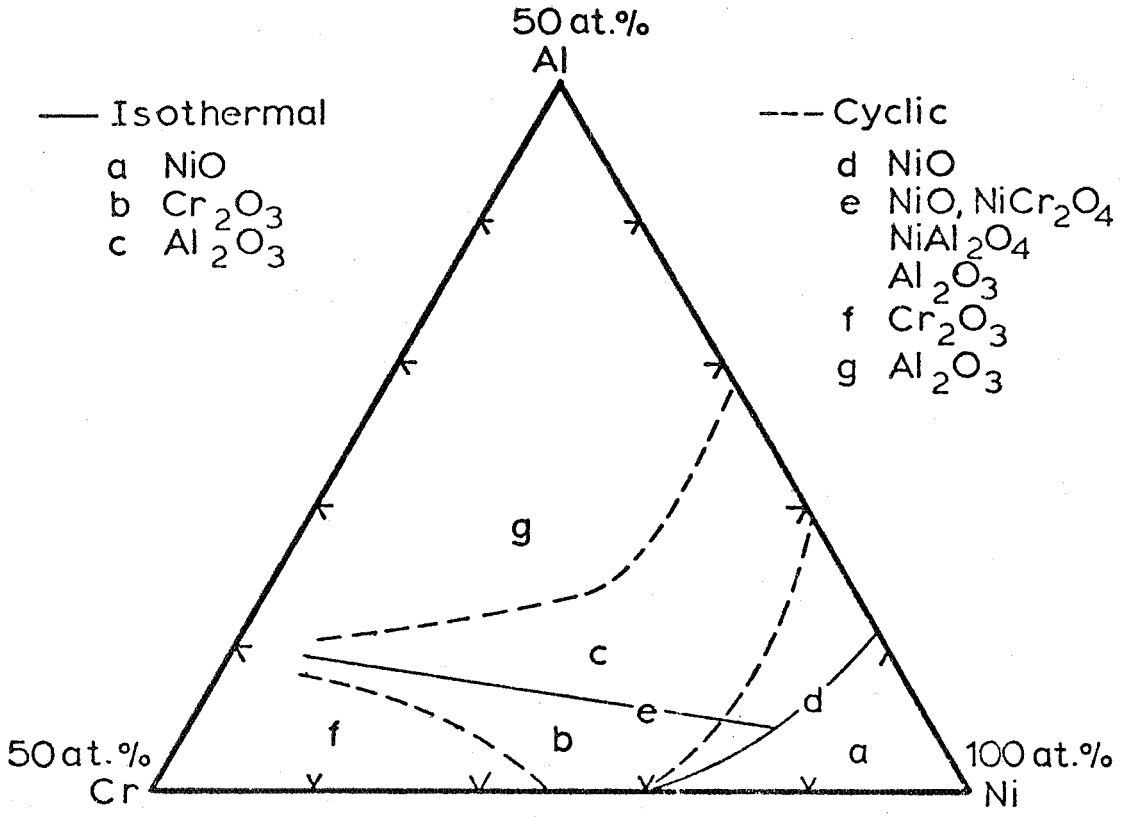

Figure 2 Oxide maps for the isothermal and cyclic oxidation of NiCrAl alloys at 1200°C. Solid lines indicate limits for isothermal oxidation, dashed lines indicate limits for cyclic oxidation. References 5 and 12.

concentration when a second-phase is involved. The second boundary condition at the oxide/metal interface may be either a solute concentration or a flux condition. For predicting the solute concentration/distance profiles after oxidation of $\gamma + \beta$ alloys, sufficient boundary conditions would be the initial solute concentration ($C_0(t)$) and the maximum solute solubility ($C_{\gamma\beta}(t)$) at the $\gamma/\gamma + \beta$ interface, and either the requisite flux ($J(t)$) or the solute concentration ($C_s(t)$) at the oxide/metal interface (see Figure 1). Wagner (8) has shown that the solute concentration at the oxide/metal interface is not sufficiently determined by thermodynamic considerations alone, but may be found by equating the solute flux in the alloy with the ionic solute flux in the oxide. Wagner has also shown that when the oxidation rate is controlled by diffusion in the oxide, the solute concentration in the alloy at the oxide/metal interface is non-zero. Ku (32) has shown that if the oxide scale grows parabolically, the oxide/metal interface concentration is independent of time.† The time-independent solute concentration at the oxide/metal interface during parabolic oxidation can be compared with the time-dependent solute concentration at the same interface during oxidation when the oxide scale thickness and requisite flux are constant, as shown in Figure 1. Bastow et al. (33) have predicted time-dependent interface concentrations during the transient oxidation period when non-parabolic rate laws apply.

Various researchers have applied a diffusional analysis to predict the concentration/distance profiles of binary alloys exhibiting parabolic oxidation

---

†Parabolic oxidation, parabolic oxidation behavior, and parabolic oxidation kinetics will refer hereafter to oxidation which results in a parabolic growth of the oxide scale ($\Delta X_{oxide} = k_1\sqrt{t}$), a parabolic decrease in the requisite flux ($J_{req} = k_2/\sqrt{t}$), a time-independent solute concentration at the oxide/metal interface ($C_s = k_3$), and for $\gamma + \beta$ type alloys, a parabolic growth of the near-surface γ layer ($\Delta X_\gamma = k_4\sqrt{t}$).

kinetics. FeCr (33-36) and NiCr (37,38) alloys have received the bulk of the research. A paucity of the necessary thermodynamic and diffusion data has precluded a diffusional analysis of the oxidation of ternary alloys.

Cyclic Oxidation

Experimental. Cyclic oxidation studies have concentrated on two areas: investigating the various parameters affecting oxide spallation, and determining the effect of oxide spallation on the overall oxidation and metal consumption rate. Early studies (20) have shown $Al_2O_3/NiAl_2O_4$ oxides or certain Cr_2O_3 oxides to possess the best cyclic oxidation resistance, i.e., to be the most adherent scales. However, Cr_2O_3 oxide scales are not considered practical due to transformation of Cr_2O_3 to CrO_3, highly volatile at temperatures in excess of 1100°C (2,3). The excessive volatization which occurs with high gas velocities or low pressures could lead to early breakaway oxidation (20). Alumina-forming alloys have been chosen as the best candidates for cyclic applications at temperatures in excess of 1100°C. An oxide map indicating the regions of Al_2O_3, Cr_2O_3, NiO, and spinel oxide formation during cyclic oxidation of NiCrAl alloys at 1200°C (12) is shown in Figure 2.

Numerous investigations have shown oxide spallation to be affected significantly by several parameters. Those parameters include cooling rates (39), quench temperature (40), oxide dispersions in the alloy (41-43), and the cycle frequency (the duration of the heating and cooling cycle) (17,44). Small additions of Pt to the alloy, or the presence of Pt in the furnace, have also been observed to increase the oxide adherence (45-47). Probably the most significant and beneficial effect is that produced by small additions of reactive metals. Zr was found to improve significantly the scale adherence of alumina-forming NiCrAl (12,48) and CoCrAl (44) alloys, and chromia-forming FeCr (41) and Cr stainless steels (49). Y has also been found to increase the scale

adherence of Al_2O_3 on NiCrAl (19,25,30), CoCrAl (19,50), and FeCrAl (26,28,29, 51) alloys. In addition, Sc (28), Th (25), and Hf (50) have been shown to exhibit a beneficial effect on scale adherence.

Evaluation of various alloys and active metal additions is typically accomplished by comparison of sample weight change measurements† made during cyclic oxidation. During the high-temperature portion of a thermal cycle, the sample weight increases parabolically with time as the oxide scale thickens. Upon cooling, patches of oxide spall non-uniformly, decreasing the weight of the sample. Depending on the scale adhesion, the overall weight change will eventually become negative. When the oxide growth is approximately equal to the oxide loss during each cycle, the weight change will decrease linearly with increasing oxidation cycles. Alloys undergoing cyclic oxidation accompanied by scale spallation are said to exhibit "paralinear-type" (6) oxidation behavior, descriptive of the weight change when plotted as a function of time as shown in Figure 3 (alloy 5A). (Paralinear-type oxidation behavior is in contrast to the parabolic weight increases observed during isothermal oxidation.) When breakaway oxidation occurs, the less protective oxides which form tend to spall at greatly accelerated rates causing an even more rapid decrease in the weight change (17), also shown in Figure 3 (alloy 14).

Theoretical. Two modeling techniques are typically employed to determine the weight of metal consumed during cyclic oxidation. The two techniques are:

1. Macroscopic spalling models, and
2. Microscopic diffusion models.

Macroscopic spalling models predict the total weight of oxide formed, the weight of the oxide which has spalled, and the weight of oxide remaining

---

†For comparison of various sample sizes, the weight change is typically divided by the total sample surface area (mg/cm^2).

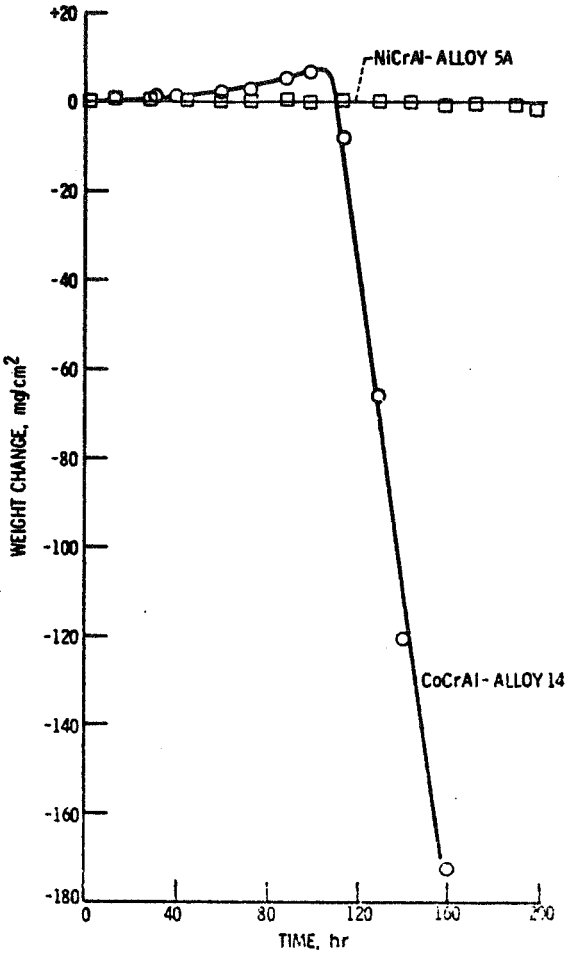

Figure 3. Comparison of the cyclic oxidation behavior of CoCrAl alloy 14 (Co-18.93at.%Cr-23.25at.%Al) and NiCrAl alloy 5A (Ni-14.35at.%Cr-23.65at.%Al) at 1200° C for 2000 0.1 hour exposure cycles. 5A data are paralinear in nature with scale of Al_2O_3 nickel aluminate plus ZrO_2 detected. Alloy 14 data break at close to 115 hour due to CoO buildup and subsequent spalling (Reference 44).

intact on the sample surface. Input to most spalling models consists of an oxide growth constant and various spalling parameters to govern the amount of oxide which spalls each cycle. Various models have been proposed for Al_2O_3 spallation from NiAl (52) and NiCrAl (53) alloys, and for the analogous case of oxide volatization from Cr_2O_3-forming alloys (54).

Microscopic diffusion models simulate the solute diffusion to the oxide/metal interface. The instantaneous solute flux at the oxide/metal interface is either known, and input to the model as a boundary condition, or can be determined from the solute concentration/distance profiles predicted by the model. From the instantaneous solute flux, and the predicted concentration/distance profiles, a diffusion model has the inherent capability to predict both the weight of solute consumed as oxide and the time to the onset of breakaway oxidation.

The solute concentration/distance profiles during cyclic oxidation are described by a solution to Fick's second law subject to two boundary conditions, the same as for the case of isothermal oxidation. The inner boundary condition is also the same as that for isothermal oxidation, viz., either an initial solute concentration or interface concentration for one-phase or multiphase alloys, respectively. The significant difference in predicting the concentration/distance profiles during cyclic oxidation and isothermal oxidation is the nature of the boundary condition at the oxide/metal interface.

The boundary condition at the oxide/metal interface during cyclic oxidation is critically dependent on the extent of oxide spallation. As previously stated, the requisite solute flux is inversely related to the oxide scale thickness. The thinner the oxide scale, the greater the requisite solute flux. During cyclic oxidation accompanied by oxide spallation, the average oxide thickness will always be less than if the scale had been fully intact. As a

result, the requisite flux† of alloys undergoing oxide spallation during thermal cycling will always be greater than the requisite flux associated with intact, adherent scales. The greater the extent of oxide spallation, the greater the requisite flux.

An alloy must supply the requisite flux if the oxide scale is to remain protective during cyclic oxidation. For the case of parabolic oxidation of a single-phase binary alloy, Wagner (8) and others (33,35-37) have shown that balancing the ionic flux in the oxide with the solute flux in the alloy results in a solute concentration at the oxide/metal interface less than the initial bulk solute concentration of the alloy. Therefore, a solute concentration gradient is established which supplies solute from the metal substrate to the oxide. The solute concentration at the oxide/metal interface remains constant as long as the oxide scale thickens parabolically (32). But, if during isothermal oxidation all or part of the oxide scale were to spall off, rebalancing the ionic oxide flux and the solute alloy flux would result in a further decrease in the solute concentration at the oxide/metal interface. Whittle (55) has derived an approximate equation describing the solute concentration in a single-phase binary alloy after total spallation of the oxide scale. The solute concentration at the oxide/metal interface, as calculated by Whittle, is always less than the interfacial solute concentration before the oxide scale was lost.

Cyclic oxidation results in repeated oxide growth followed by total, or partial, oxide spallation. Repeated application of the previous argument would indicate a discontinuous decrease in the solute concentration at the oxide/metal interface during cyclic oxidation accompanied by scale spallation.

---

†Due to non-uniform oxide spallation, the requisite flux during cyclic oxidation will always be considered as an average flux evaluated across a sample surface.

The extent of the decrease in the interfacial solute concentration would be expected to depend on whether all, or only a portion, of the oxide scale spalled. Similarly, the previous statements could be extended to predict a decreasing interfacial solute concentration during the cyclic oxidation of two-phase alloys.

The solute concentration at the oxide/metal interface must not be depleted below that for thermodynamic stability of the solute oxide if the alloy is to continue to provide a protective oxide scale (55). Stated otherwise, breakaway oxidation occurs during cyclic oxidation when the interfacial solute concentration has decreased to approximately zero. Time-dependent interfacial solute concentrations resulting in breakaway oxidation were shown schematically in Figures 1a and 1b.

Some researchers have predicted time-dependent oxide/metal interface concentrations by assuming various oxide growth rate laws. Most of the predictions involve the non-parabolic oxidation rates associated with the initial transient oxidation of binary alloys (56). Bastow et al. (33) have extended the analysis to include the prediction of breakaway oxidation in a CoCr alloy exhibiting paralinear oxidation behavior. The decrease in the Cr concentration at the oxide/metal interface was predicted as a result of the non-parabolic requisite flux associated with Cr_2O_3 volatization.

Philosophy and Approach

The cyclic oxidation of $\gamma + \beta$, NiCrAlZr(Y) alloys results in the selective oxidation of Al to form a protective Al_2O_3 oxide scale. A γ-phase subsurface layer thickens with time as Al is transported to the growing oxide. Active metal additions affect the rate of oxide spallation which governs the requisite Al flux for the sole formation and growth of Al_2O_3. The requisite Al flux fixes the Al transport in the γ-phase layer which controls

the growth of the layer. The ability of the alloy to supply the requisite flux is dependent on the diffusivity of the particular alloy, the maximum possible Al gradient in the γ layer, and the effect of the Cr concentration profile on the diffusion of Al. The maximum possible Al gradient is a function of the alloy composition with respect to the NiCrAl ternary phase diagram. Hence, varying the Y or Zr content of the alloys affects the rate of oxide spallation, which in turn affects the requisite Al flux, and therefore the Al transport and growth rate of the γ-phase subsurface layer.

Purpose

Verification

The first goal of this study was to verify the effect of various requisite flux conditions on the Al transport in $\gamma + \beta$, NiCrAlZr(Y) alloys undergoing cyclic oxidation. The $\gamma + \beta$ alloys were chosen so as to allow examination of the effect of various concentrations, various maximum solubilities of Al in the γ phase, and various diffusivities on the diffusional transport of Al and on the ability of each alloy to avoid breakaway oxidation. Varying the Zr or Y content of the alloys was used to induce differing oxide spallation characteristics. The effect of the above parameters was examined by optical microscopy and quantitative electron microscopy of the alloys after various cyclic oxidation exposures. X-ray diffraction of the oxide scale retained on the sample surface was used to identify the oxide phases.

Prediction

The second goal of this study was development of a numerical model to simulate the Al transport during the cyclic oxidation of $\gamma + \beta$, NiCrAlZr(Y) alloys. Diffusion models are capable of predicting concentration/distance profiles and phase layer widths (in multiphase applications). Diffusion

models typically require the input of boundary conditions and diffusivities specific to each alloy. The accuracy and validity of the predictions by the diffusion model would be ascertained by a direct comparison with the results from the experimental analysis of the cyclically oxidized alloys.

EXPERIMENTAL RESULTS

Procedure

Three alloy compositions were chosen for examination of the Al transport during the cyclic oxidation of $\gamma + \beta$ NiCrAl alloys at 1200°C. Two alloy compositions contained approximately the same Al concentration but different Ni and Cr concentrations, whereas the third alloy composition contained a greater Al concentration but lower Ni and Cr concentrations. Different Zr contents were added to each of the alloys to effect various oxide spalling characteristics. The Zr was added by one of two techniques. One technique consisted of induction melting the metallic elemental constituents Ni, Cr, Al, and Zr in alumina crucibles. In the second technique, metallic Ni, Cr, and Al were induction melted in zirconia crucibles which permitted Zr to be leached from the crucible. The longer the melt was held in the zirconia crucible, the greater the Zr content of the resulting alloy. One alloy composition was alloyed with Zr by both techniques to examine the effect of the Zr content and alloying technique on the oxidation behavior. The same alloy composition[†] was also alloyed with Y to allow a specific comparison of the effect of Y and Zr on the diffusional transport of Al during cyclic oxidation. Following the induction melting, all the alloy melts were poured into zirconia leaf molds. Very little Zr was leached from these molds (57). The compositions of the alloys and the method of alloying are listed in Table I.

The alloys were fabricated and oxidized at the Lewis Research Center of the National Aeronautics and Space Administration. The alloys were oxidized in the cast state without previous heat treatments. Isothermal oxidation was

---

[†]Different alloying techniques and different alloy additions (Zr or Y) to the same alloy composition resulted in variations in the Al and Cr concentration (of 1 - 2 at.%) between the alloys.

TABLE I

ALLOY COMPOSITIONS

Alloy Designation	Composition (at.%) Ni	Cr	Al	Zr(Y)	Alloying Technique
Ni-13Cr-25Al-0.05Zr	61.95	13.26	24.73	0.054	a
Ni-14Cr-25Al-0.07Zr	61.92	14.35	23.66	0.066	b
Ni-14Cr-25Al-0.12Y	61.16	13.75	24.97	0.12Y	a
Ni-19Cr-24Al-0.04Zr	57.37	19.00	23.59	0.038	b
Ni-17Cr-28Al-0.18Zr	54.41	17.06	28.35	0.18	b

a. Alloyed with Zr or Y by induction melting of the elemental, metallic constituents in an alumina crucible.

b. Alloyed with Zr by induction melting metallic Ni, Cr, and Al in a zirconia crucible allowing Zr to be leached from the crucible.

performed at 1200°C in still air. Cyclic oxidation testing consisted of a one-hour exposure at 1200°C in still air followed by a minimum cooling period of twenty minutes at approximately room temperature, also in air. The oxidation/cooling cycle was repeated various times for each of the alloys.† The change in weight per unit sample area was measured during both the isothermal and cyclic oxidation tests. Paralinear weight change curves of the four Zr-containing alloys indicate a significant range in the oxide spalling characteristics between the alloys. The weight change curves are shown in Figure 4. At longer times, the Ni-13Cr-25Al-0.05Zr and Ni-17Cr-28Al-0.18Zr alloys exhibit the most rapid weight loss, indicating poor scale adherence. In comparison, the Ni-19Cr-24Al-0.04Zr and the Ni-14Cr-24Al-0.07Zr alloys exhibit a much lower weight loss, indicating better scale adherence. Further details of alloy fabrication, the oxidation equipment, and testing procedures are given elsewhere (12,27,48).

The three alloys containing 24 - 25 at.%Al initially possess very similar $\gamma + \beta$ microstructures with 0.6 - 0.75 volume fraction of the β phase present. The Ni-17Cr-28Al-0.18Zr alloy initially contains approximately 0.96 volume fraction of the β phase. (The volume fractions of the β phase decrease after long cyclic oxidation exposures. The microstructural changes during cyclic oxidation will be discussed shortly.) The microstructures of the four alloys and the alloy position in the $\gamma + \beta$ field of the NiCrAl ternary diagram at 1200°C are shown in Figure 5. The dendritic β phase (dark phase in the micrographs of Figure 5) has the NiAl (or CsCl) type crystal structure. The γ phase (light phase in the micrographs of Figure 5) is a Ni solid solution with an FCC

---

†The cyclic oxidation time referred to in this report will only account for the high-temperature period of each cycle. Hence, cyclically oxidized for 800 hours refers to 800 cycles, each consisting of one hour at 1200°C followed by a minimum of 20 minutes at room temperature.

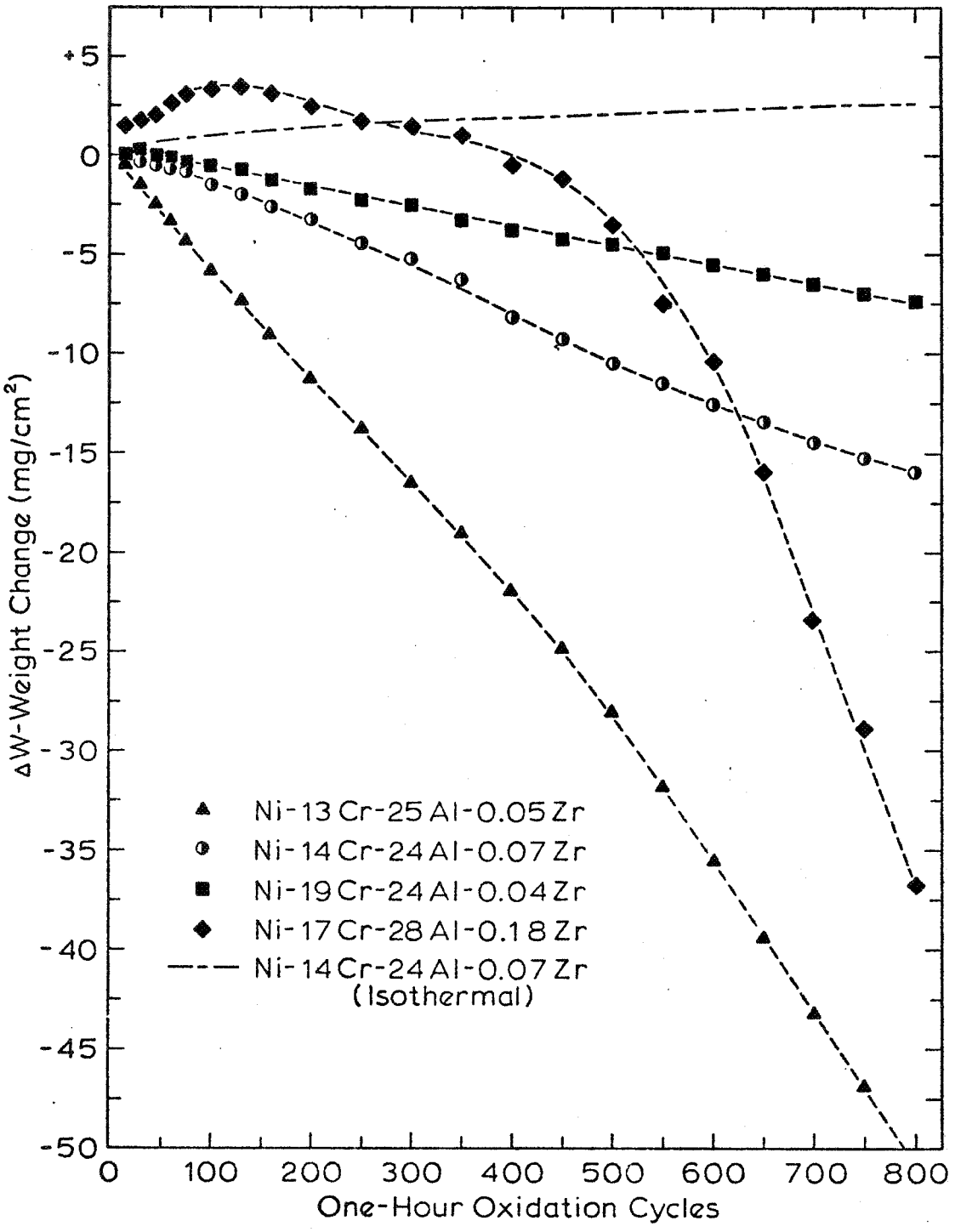

Figure 4. Paralinear weight change curves for the Zr-containing alloys during cyclic oxidation. Parabolic weight gains during isothermal oxidation of the Ni-14Cr-24Al-0.07Zr alloy is also shown.

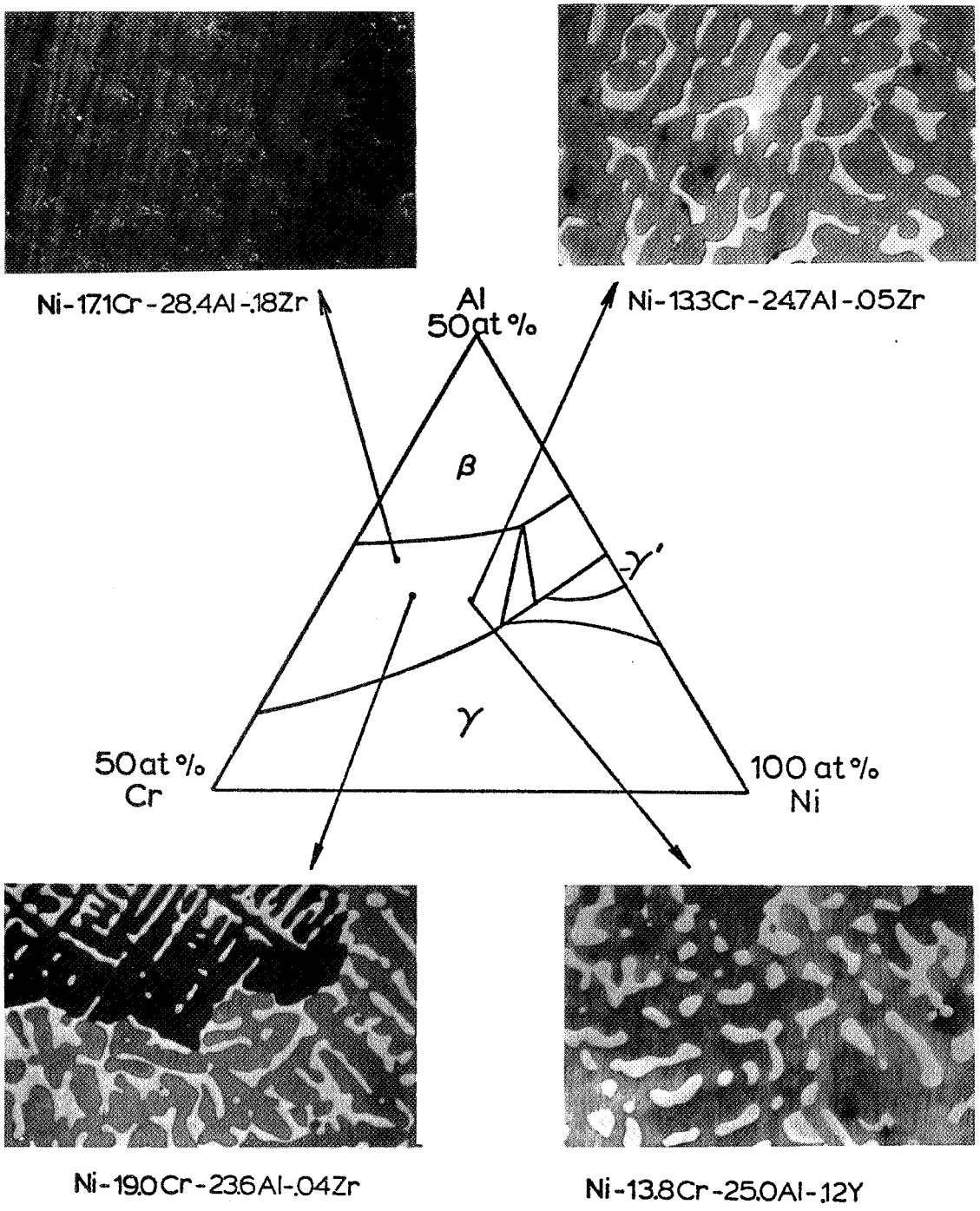

Figure 5. Microstructures of the four, γ+β NiCrAl alloys examined in this study.

type crystal structure. No enrichment of Zr was detected by optical metallography, x-ray mapping on the electron microscope, or by x-ray diffraction of the three alloys containing Zr. The Y-containing alloy contained a low volume fraction of a Ni and Y enriched phase at the boundaries between the γ and β phases, most probably Ni yttrides (19,25,28,29). Hence, the solubility limit of Y was exceeded but the solubility limit of Zr was not, in accordance with previous studies (19,25,27,30).

The oxide phases retained on the surface of each oxidized alloy were determined by x-ray diffraction. The intensities of the oxide and metal substrate peaks were ranked to indicate the proportion of each of the oxide phases present. The oxide and metal phases detected are listed and ranked in Table II. The Ni-14Cr-24Al-0.07Zr and Ni-19Cr-24Al-0.04Zr alloys show the strongest Al_2O_3 presence through 800 hours. Both alloys exhibited good oxide spalling characteristics evident from the weight change data in Figure 4. The Ni-13Cr-25Al-0.05Zr and Ni-17Cr-28Al-0.18Zr alloys show considerable spinel formation after 500 hours of cyclic oxidation exposure. Both alloys exhibit poor oxide spalling characteristics, also evident from the weight change data in Figure 4. Continuous formation of Al_2O_3 results in the best oxide spalling characteristics.

The oxide morphologies of the four alloys are as varied as the paralinear weight change data of Figure 4. The oxide morphologies differ between alloys and with increasing oxidation time. Examples of the various morphologies are shown in Figure 6. The oxide morphologies range from relatively flat (Figure 6a) to rough and porous (Figures 6b and 6g). Oxide spallation from a sample surface does not occur uniformly but from random, discrete sections on the sample surface. The sample surface of the Ni-14Cr-25Al-0.12Y alloy, shown in Figure 7, illustrates the random oxide spallation. The light areas in

TABLE II

OXIDE PHASES PRESENT AFTER CYCLIC OXIDATION

Alloy	Time (hrs)	Ni Solid Soln.	Al_2O_3	Spinel (a_o)	Other
Ni-13Cr-25Al-0.05Zr	100	vs	m		
	200	vs	s	vw (8.06-8.09)	
	500	vs	w	vw 8.09	
	800	vs	w	m 8.06-8.09	Cr_2O_3 (vw)
Ni-14Cr-24Al-0.07Zr	800	vs	w	w 8.06	
Ni-14Cr-25Al-0.12Y	100	vs	m		
	200	vs	w	vw 8.09	
	500	vs	m	vw 8.09-8.10	YAG (vw) Yttrogarnet ($3Y_2O_3 \cdot 5Al_2O_3$)
	1000	vs	vs	s (8.09)	
Ni-19Cr-24Al-0.04Zr	100	vs	s	vw (8.06)	
	500	s	vs	w (8.06)	
	800	m	vs	vw (8.06)	
	1600	m	vs	m (8.06)	
Ni-17Cr-28Al-0.18Zr	200	s	vs	m (8.09)	ZrO_2 (w) monoclinic and cubic
	500		s	vs (8.06)	Cr_2O_3 (w), NiO(w), ZrO_2(vw)
	800		m	vs (8.06)	Cr_2O_3 (w)

The oxide and metal phases were ranked by normalizing the largest peak for each phase to the largest peak measured on that particular sample. The normalized peaks were ranked as 0.8-1.0, very strong (vs); 0.5-0.8, strong (s); 0.2-0.5, medium (m); 0.1-0.2, weak (w); and o.1, very weak, (vw).

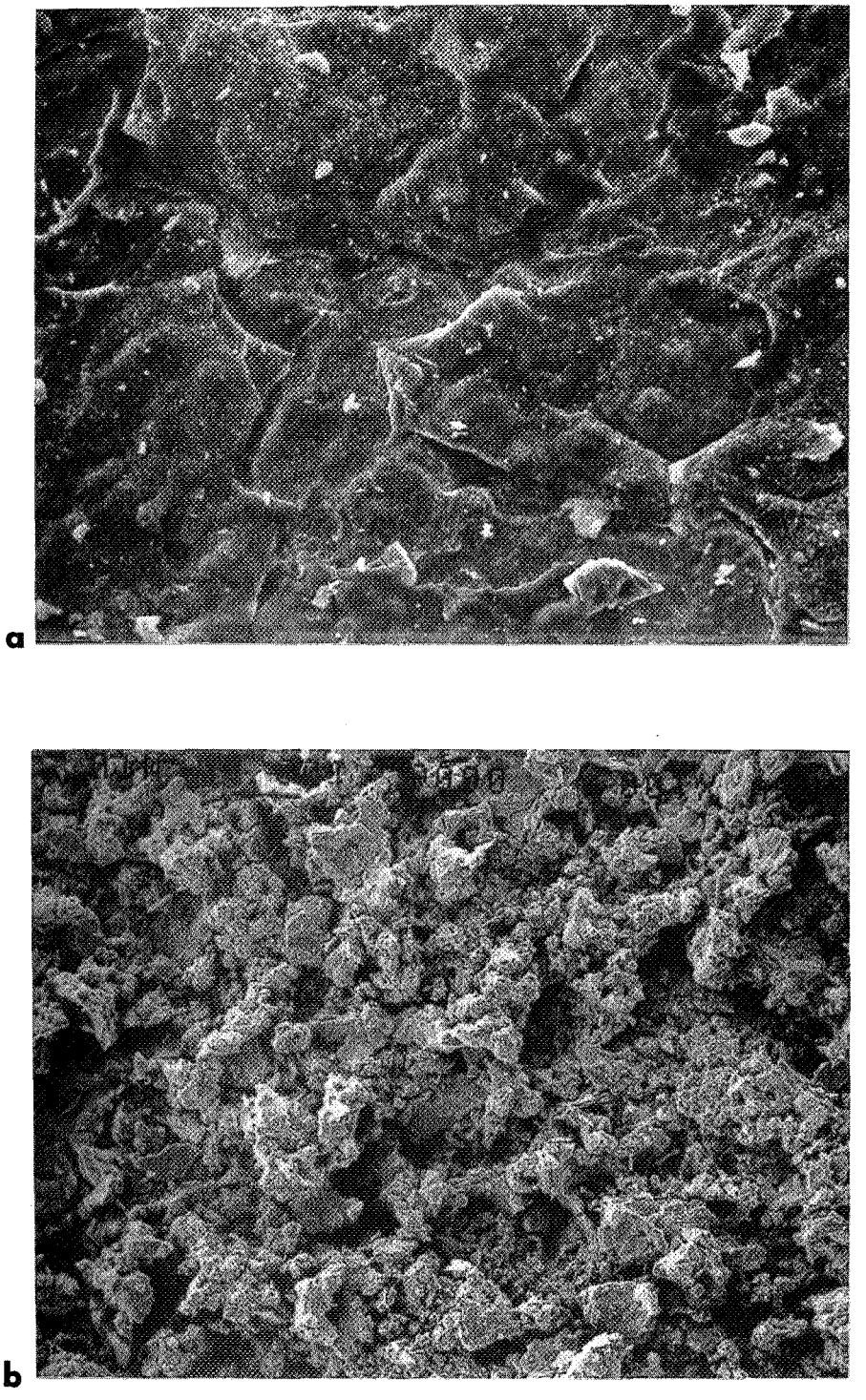

Figure 6 Surface oxide morphologies after cyclic oxidation a. Ni-13Cr-25Al-0.05Zr alloy after 800 oxidation cycles (500x) b. Ni-14Cr-25Al-0.12Y alloy after 1000 oxidation cycles (100x).

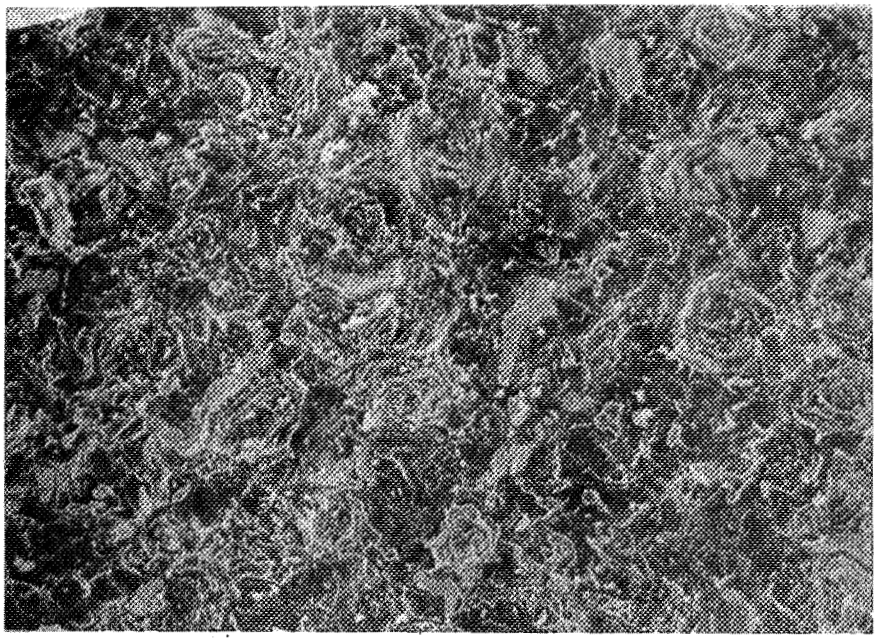

c

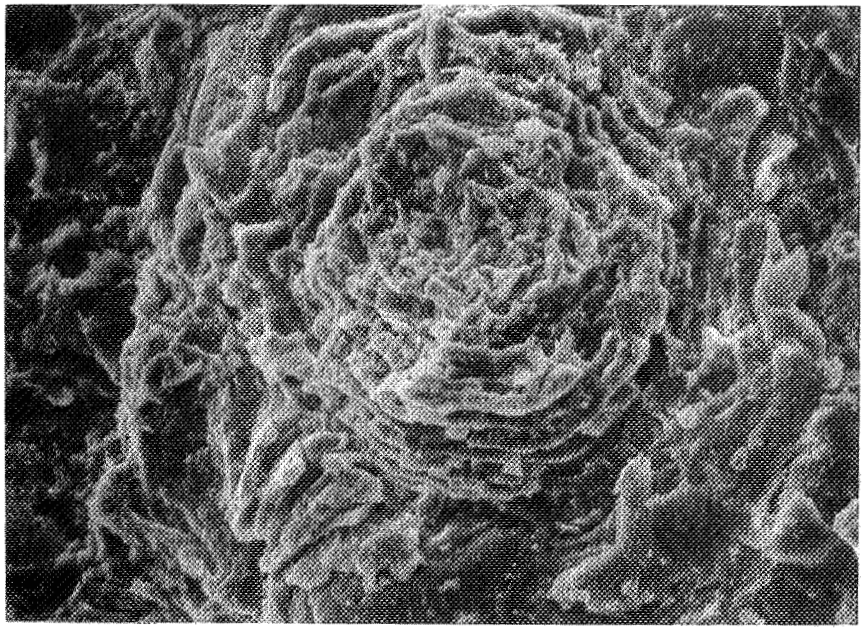

d

Figure 6 cont. c. Ni-14Cr-24Al-0.07Zr alloy after 800 oxidation cycles (100x) d. same as c. (500x)

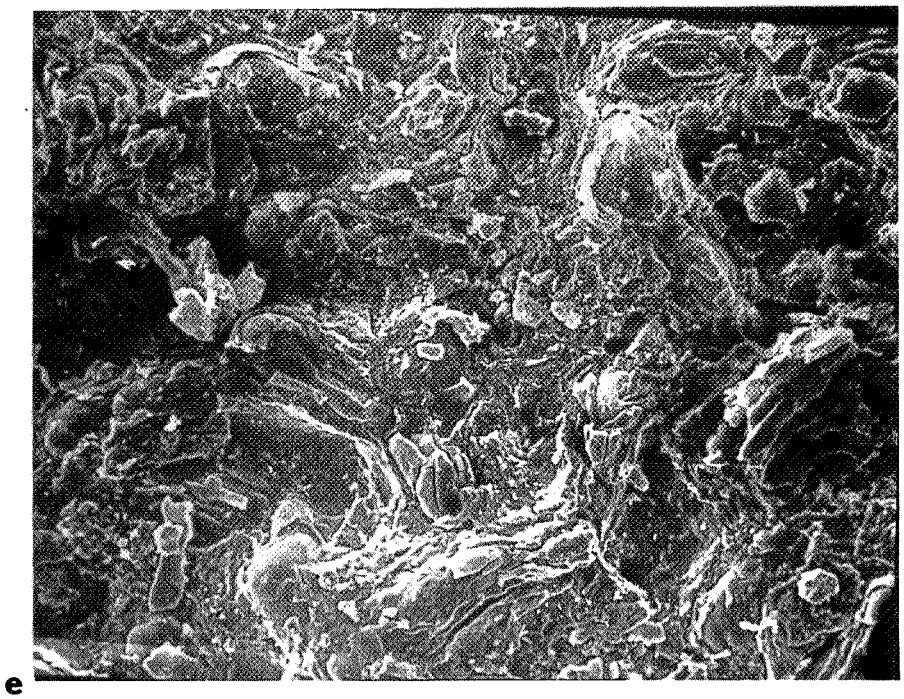

e

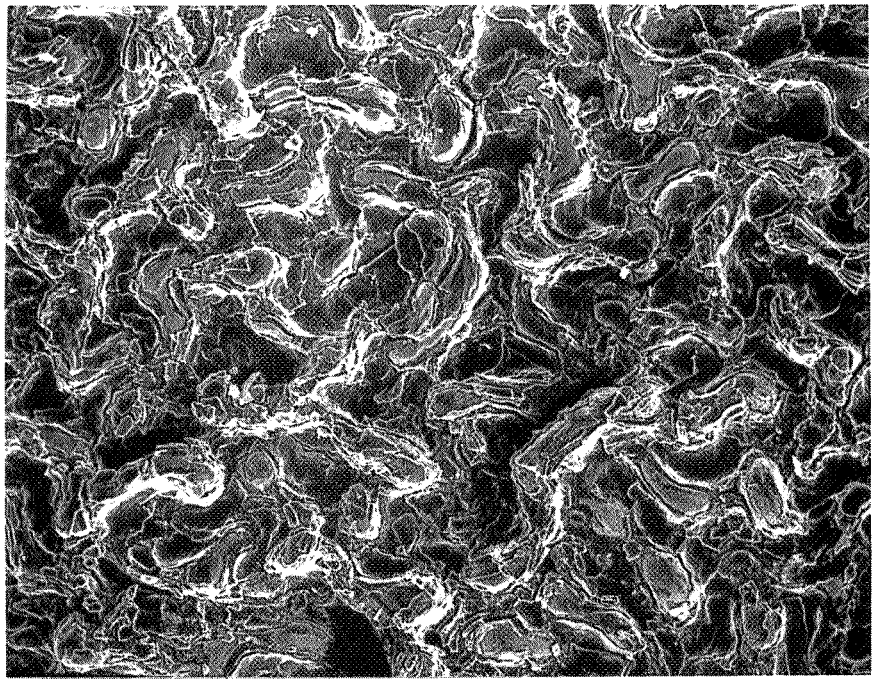

f

Figure 6 cont. e. Ni-19Cr-24Al-0.04Zr alloy after 800 oxidation cycles (200x) f. same as e. after 1200 oxidation cycles (100x).

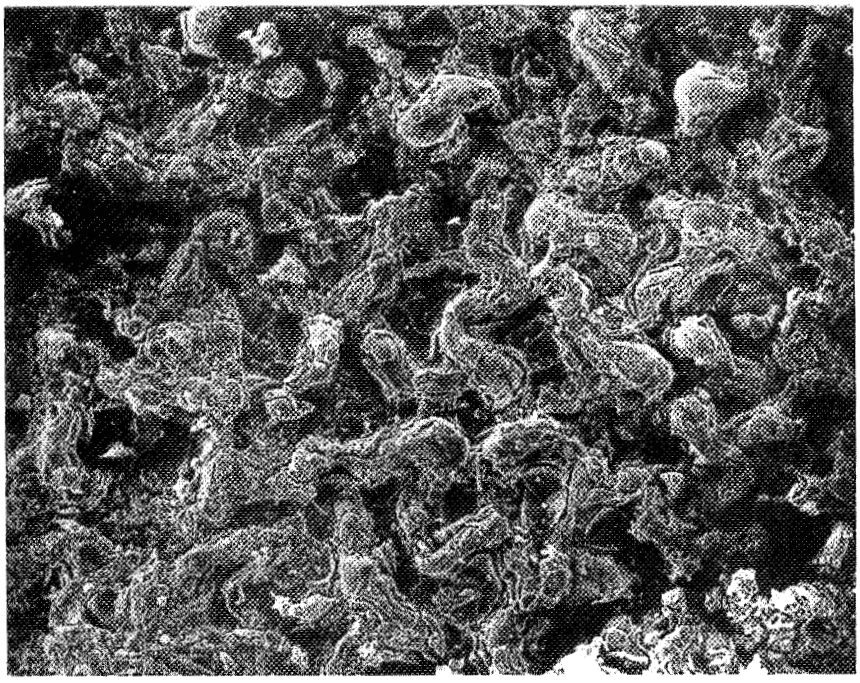

g

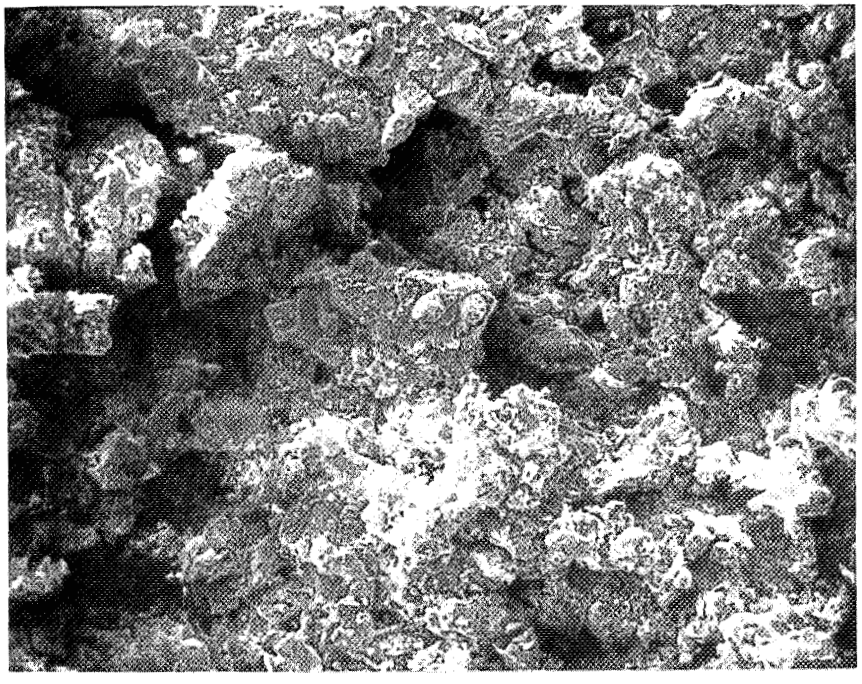

h

Figure 6 cont. g. Ni-19Cr-24Al-0.04 Zr alloy after 1600 oxidation cycles (100x) h. Ni-17Cr-28Al-0.18Zr alloy after 800 oxidation cycles (100x).

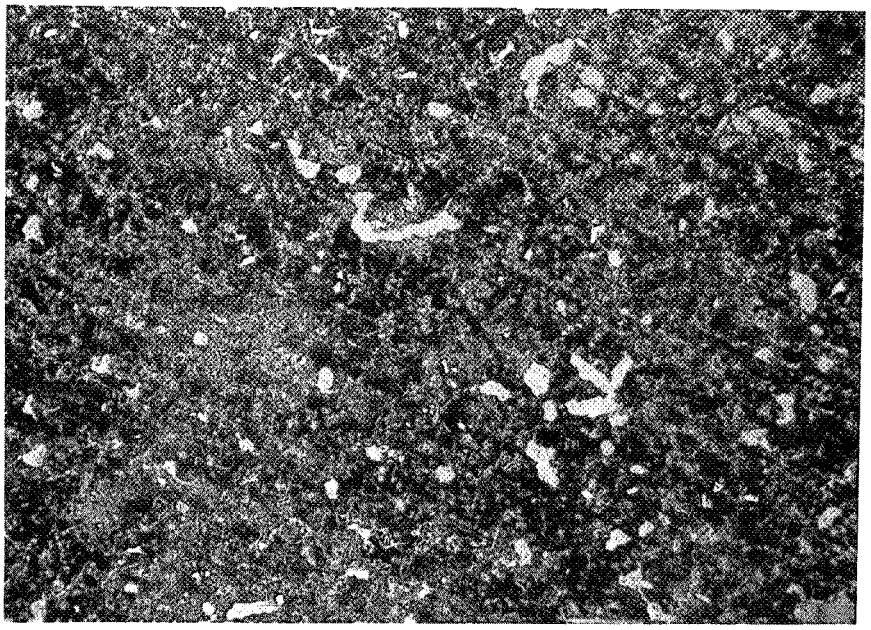

a

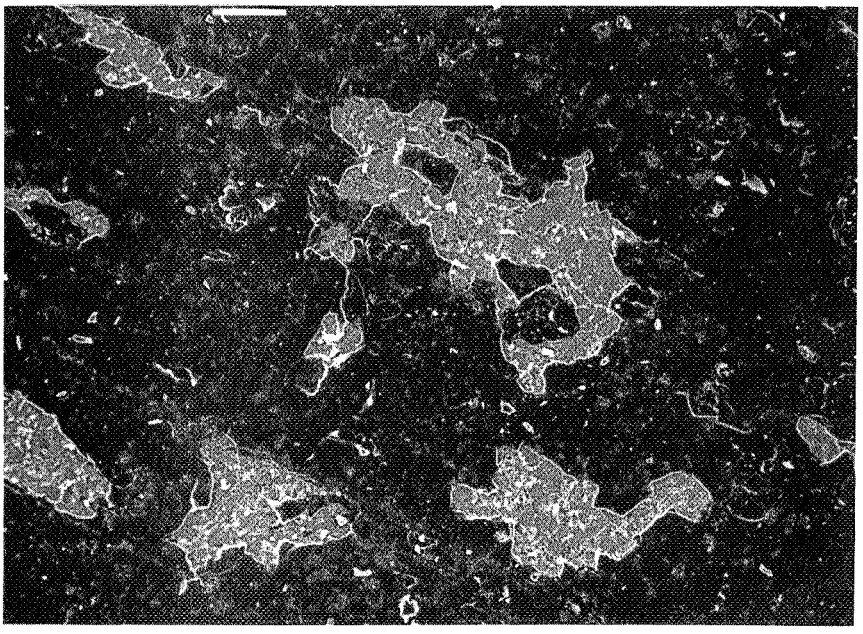

b

Figure 7 Surface oxide morphologies on the Ni-14Cr-25Al-0.12Y alloy after various cyclic oxidation exposures (100x). a. 1 oxidation cycle b. 15 oxidation cycles

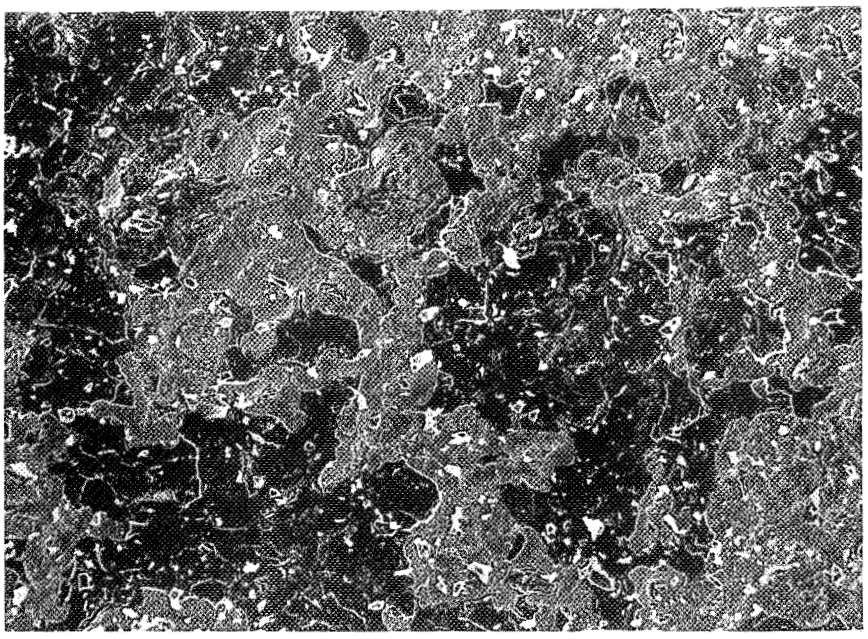

c

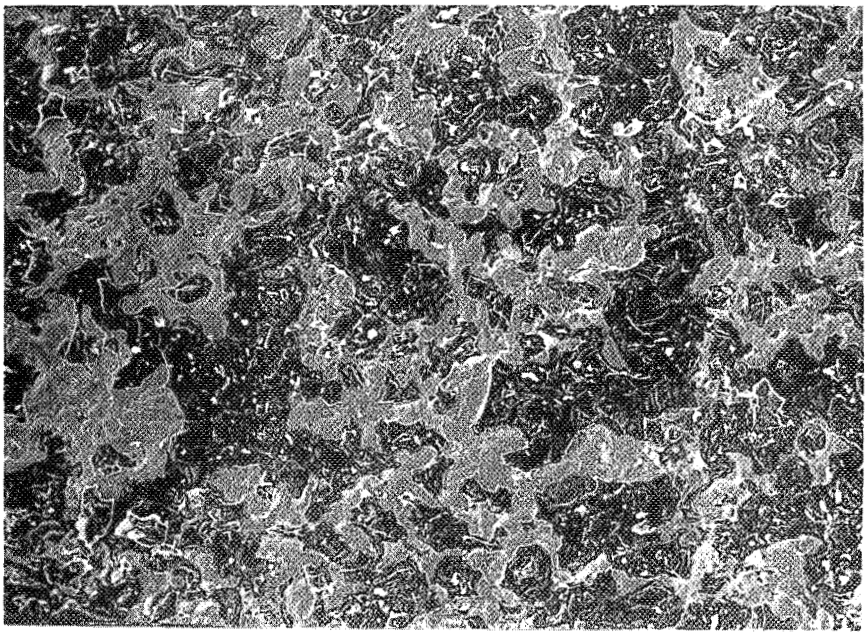

d

Figure 7 cont. c. 100 oxidation cycles d. 200 oxidation cycles.

the micrographs are the locations where the oxide layer has spalled. After 200 cycles, the oxide had spalled from over half the sample surface. No correlation was found between the pattern of oxide spallation and the initial $\gamma + \beta$ microstructure. After 1000 oxidation cycles (Figure 6b), the sample surface bears no resemblance to the early oxide scales.

Oxidation of $\gamma + \beta$ NiCrAl alloys results in the growth of a near-surface γ layer by dissolution of the β phase at the $\gamma/\gamma + \beta$ interface. Al is transported across the γ layer to the oxide/metal interface where it is consumed in formation of the oxide. To determine the width of the γ layer, and to prepare for quantitative electron microscopy, the orthorhombic-shaped samples were sectioned perpendicular to the main axis (z or c), thereby exposing a cross section of the alloy perpendicular to the plane of the oxide scale. The cut samples were mounted and polished by standard metallographic techniques. The near-surface γ-layer width was measured by optical microscopy using a filar eyepiece. The volume fraction of the β phase was also measured optically after various oxidation exposures. Following the optical examination, the mounted samples were carbon coated for use in the scanning electron microscope.

Four to eight Ni, Cr, and Al concentration/distance profiles were measured across the near-surface γ layer for each alloy after various cyclic oxidation exposures. The concentration/distance profiles exhibited differences when measured across the γ layer at various locations on a sample. The differences between the measured concentration/distance profiles were usually greater than the possible discrepancies introduced by the measuring technique. The differences in the concentration profiles are therefore attributed to either compositional variation within the as-cast sample, or to a varying requisite flux resulting from random oxide spallation. The concentration of the γ and β phases in the $\gamma + \beta$ region of each sample was also measured after various

oxidation exposures. Greater detail of the technique for measuring the concentrations with the scanning electron microscope is given in Appendix A. The results will be presented separately for each alloy.

Experimental Results

Ni-13Cr-25Al-0.05Zr

The near-surface γ-phase layer thickened at a rapid, non-parabolic rate. the volume fraction of the β phase decreased from 0.73 to 0.43 after 800 oxidation cycles. A third phase, γ', based on the Ni_3Al-type intermetallic phase formed at the $\gamma/\gamma+\beta$ interface between 500 and 800 oxidation cycles. In addition, the sample underwent a volume distortion after 500 oxidation cycles so that the sectioned plane (x-y plane shown in Figure 8) of the 800-hour sample had decreased in the y direction but increased in the x direction (Figure 8). Changes in the z direction could not be determined. The γ layer, always measured in the x direction on all samples, was observed to increase abnormally due to the anomalous volume distortion. Considerable Kirkendall-type porosity was evident in the near-surface γ layer (Figure 8a) but was not observed on other alloys exhibiting volume distortions (Ni-14Cr-25Al-0.12Y alloy, Figure 8b). Therefore, the porosity alone cannot be the cause of the volume distortion. The microstructures and the near-surface γ layer after various oxidation exposures of the Ni-13Cr-25Al-0.05Zr alloy are shown in Figure 9.

The rapid loss of Al results in a time-decreasing Al concentration at the oxide/metal interface. The decreasing Al concentration at this interface is attributed to an increased requisite flux encountered during cyclic oxidation accompanied by significant oxide spallation. Discontinuous loss of the oxide scale results in an average scale thickness less than that which occurs during parabolic oxidation. The thinner oxide scale results in a greater requisite

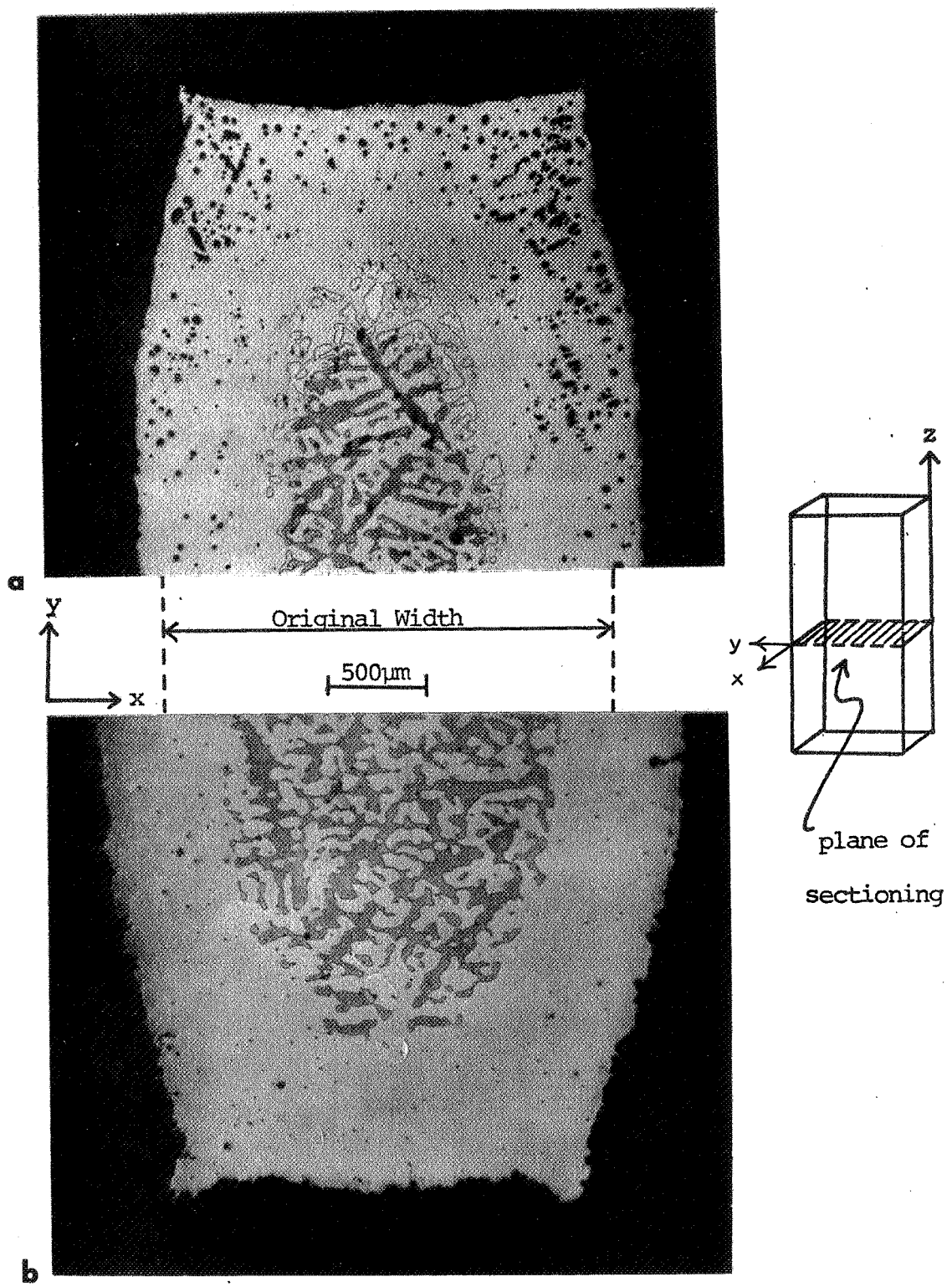

Figure 8 Volume distortion of sample coupons a. Ni-13Cr-25Al-0.05Zr alloy after cyclic oxidation for 800 hours b. Ni-14Cr-25Al-0.12Y alloy after cyclic oxidation for 1000 hours. Schematic drawing to right shows the relationship between plane of sectioning (dashed) and sample coupon.

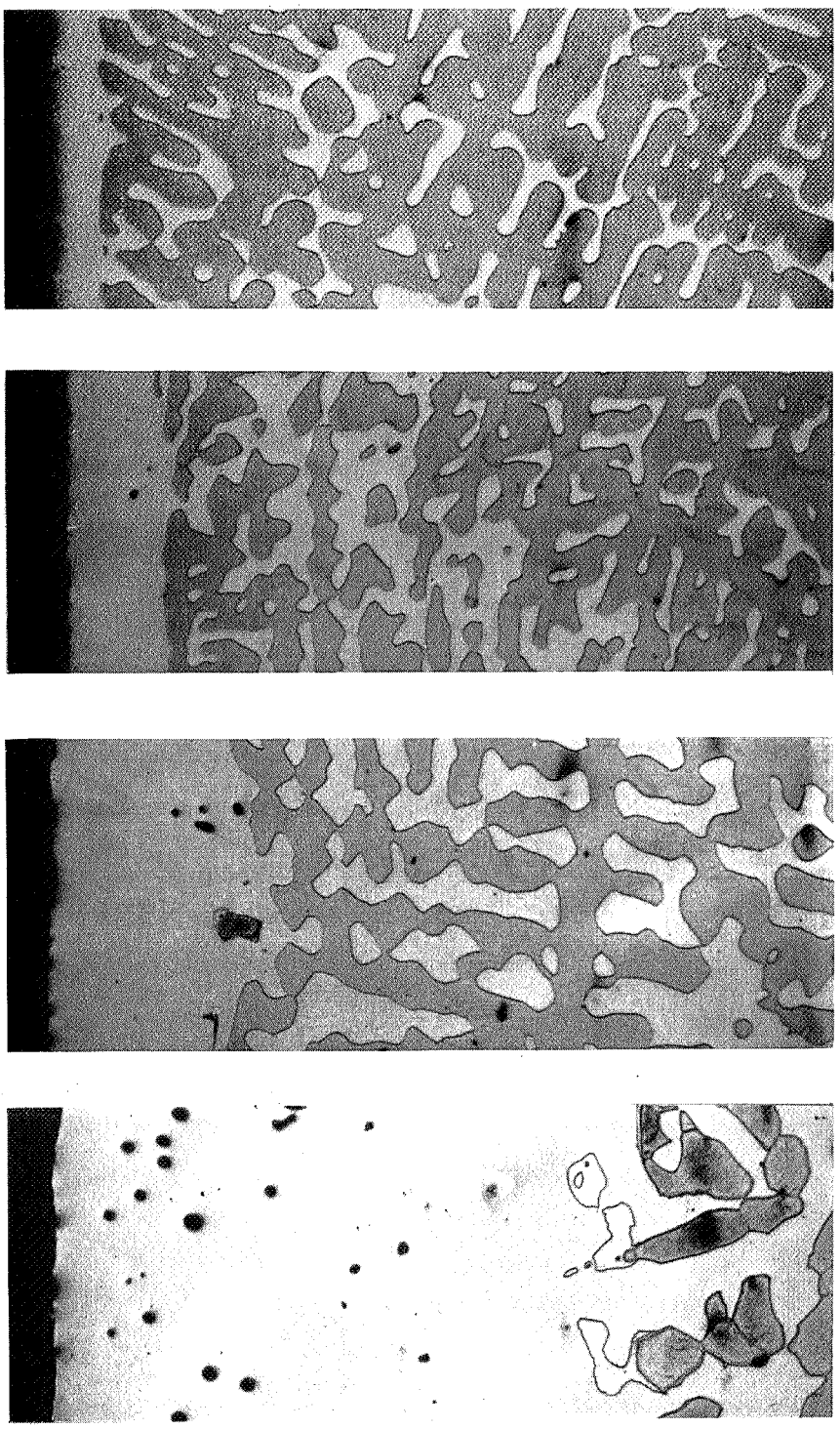

Figure 9. Micrographs of the near-surface γ layer after cyclic oxidation of the Ni-13Cr-25Al-0.05Zr alloy.

flux ($J_{req} \alpha\ 1/\Delta X_{oxide}$). The Al concentration at the oxide/metal interface decreases with time, increasing the concentration gradient, and thereby supplying the increased requisite Al flux for continued Al_2O_3 formation and growth. The decreasing Al concentration at the oxide/metal interface is shown as the left-most point of the Al concentration/distance profiles in Figure 10. The Ni and Cr concentration profiles are also shown. The right-most point of each profile indicates the position of the $\gamma/\gamma+\beta$ interface, and the Ni, Cr, and Al concentrations at that interface. The right-most point also gives the concentration of the γ phase in the $\gamma+\beta$ region of each sample. There were no measurable concentration gradients in the $\gamma+\beta$ region. The error bars on the right-most point indicate the average standard deviation on the concentrations on that particular Ni, Cr, or Al profile. Comparison of the individual profiles measured at various locations on a single sample indicated the scatter to be the result of profile-to-profile differences and not the result of the measuring technique. The differences between the concentration profiles measured at various locations along the sample are attributed to the non-uniform oxide spallation observed following cyclic oxidation of these alloys (Figure 7). The non-uniform oxide spallation results in a range in the oxide thickness on the sample surface, which further results in a range in the requisite flux along the sample surface. The differences in the measured concentration profiles reflect the varying response of the alloy in supplying Al over the range of requisite flux conditions.

The Al and Ni concentrations at the $\gamma/\gamma+\beta$ interface (right-most concentration points, Figure 10) increase with increasing oxidation time, whereas the Cr concentration at the interface decreases with increasing oxidation time. In addition, the entire Ni concentration profiles shift to greater Ni concentrations with increasing oxidation time while the Al and Cr concentration profiles

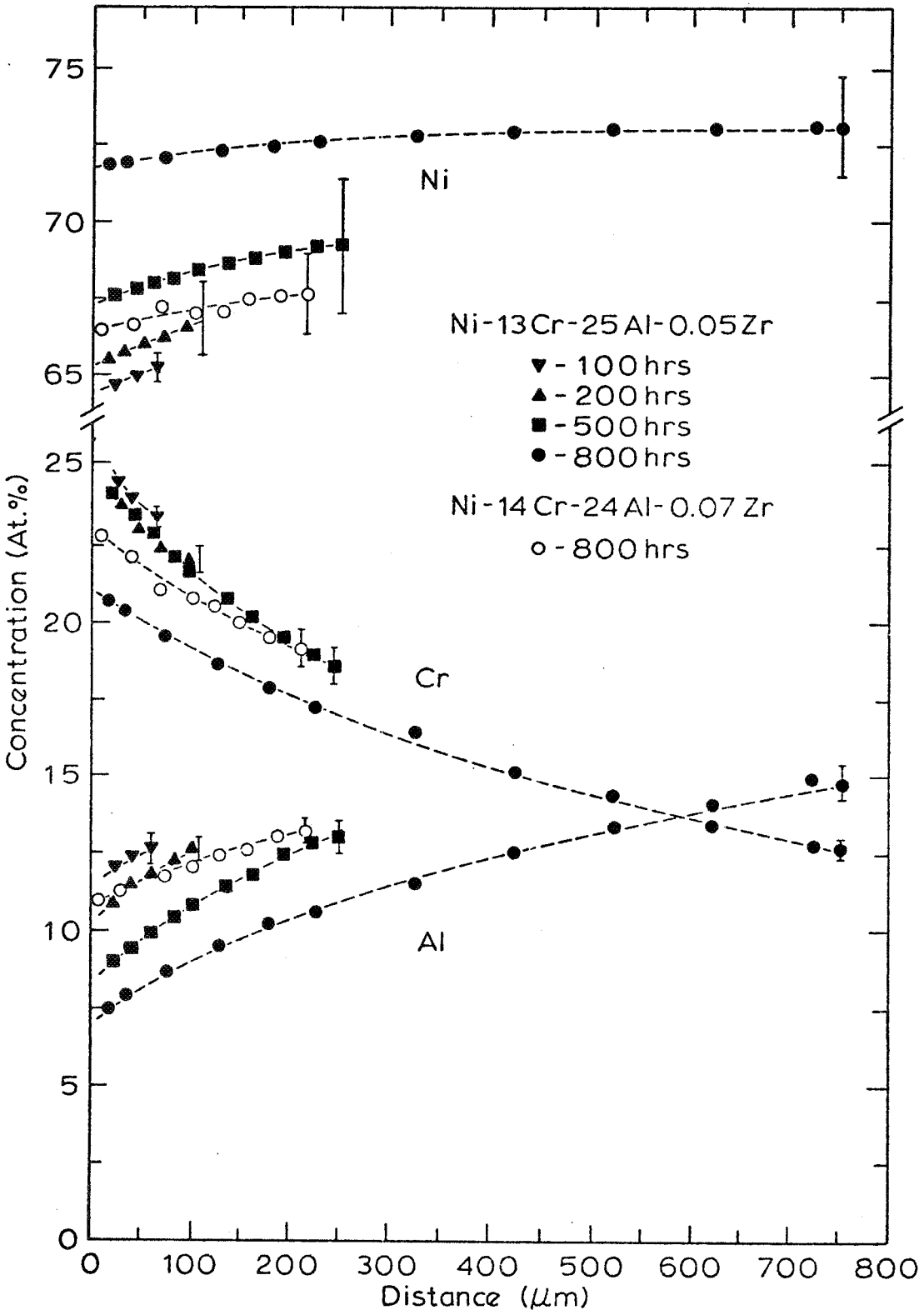

Figure 10. Ni, Cr, and Al concentration/distance profiles in the γ layer after cyclic oxidation of the Ni-13Cr-25Al-0.05Zr and the Ni-14Cr-24Al-0.07Zr alloys.

generally decrease with increasing oxidation time. The overall increase or decrease in the concentration profiles can be observed and explained by plotting the concentration profiles as diffusion paths on the NiCrAl phase diagram. The diffusion paths are observed to "translate" toward the Ni-rich corner of the phase diagram, as shown in Figure 11. The solubility limit of Al in the γ phase (the line dividing the γ and $\gamma + \beta$ fields) is the effective solubility limit at 1200°C used throughout this study, as discussed in Appendix B.

The diffusion path translation can be understood by determining the composition of the sample after oxidation. First, consider a Ni-18Cr alloy with the same Cr/Ni ratio (0.21) as the Ni-13Cr-25Al-0.05Zr alloy (point A in Figure 11). If pure Al is added to this binary alloy, the resulting composition of the NiCrAl alloy would lie on a line connecting point A to the 100 at.%Al corner, also passing through the Ni-13Cr-25Al composition (see inset, Figure 11). Similarly, if Al were removed from the Ni-13Cr-25Al alloy, the resulting composition would again fall on the dashed line in Figure 11. The composition of the Ni-13Cr-25Al-0.05Zr alloy after oxidation is the sum of the average compositions in the $\gamma + \beta$ region and the near-surface γ layer, weighted in proportion to the fractional amount of the $\gamma + \beta$ region (or γ layer) present after the oxidation exposure. The average composition of the γ layer, determined from Figure 10, and the average composition of the $\gamma + \beta$ region, determined from the concentration and volume fraction of each phase, are indicated as open squares for each diffusion profile shown in Figure 11. The composition of the sample lies on a line connecting the average compositions of the $\gamma + \beta$ region and the γ layer and is shown as open triangles in Figure 11. As shown, the composition of the sample after oxidation closely follows the dashed line of constant Cr/Ni ratio.

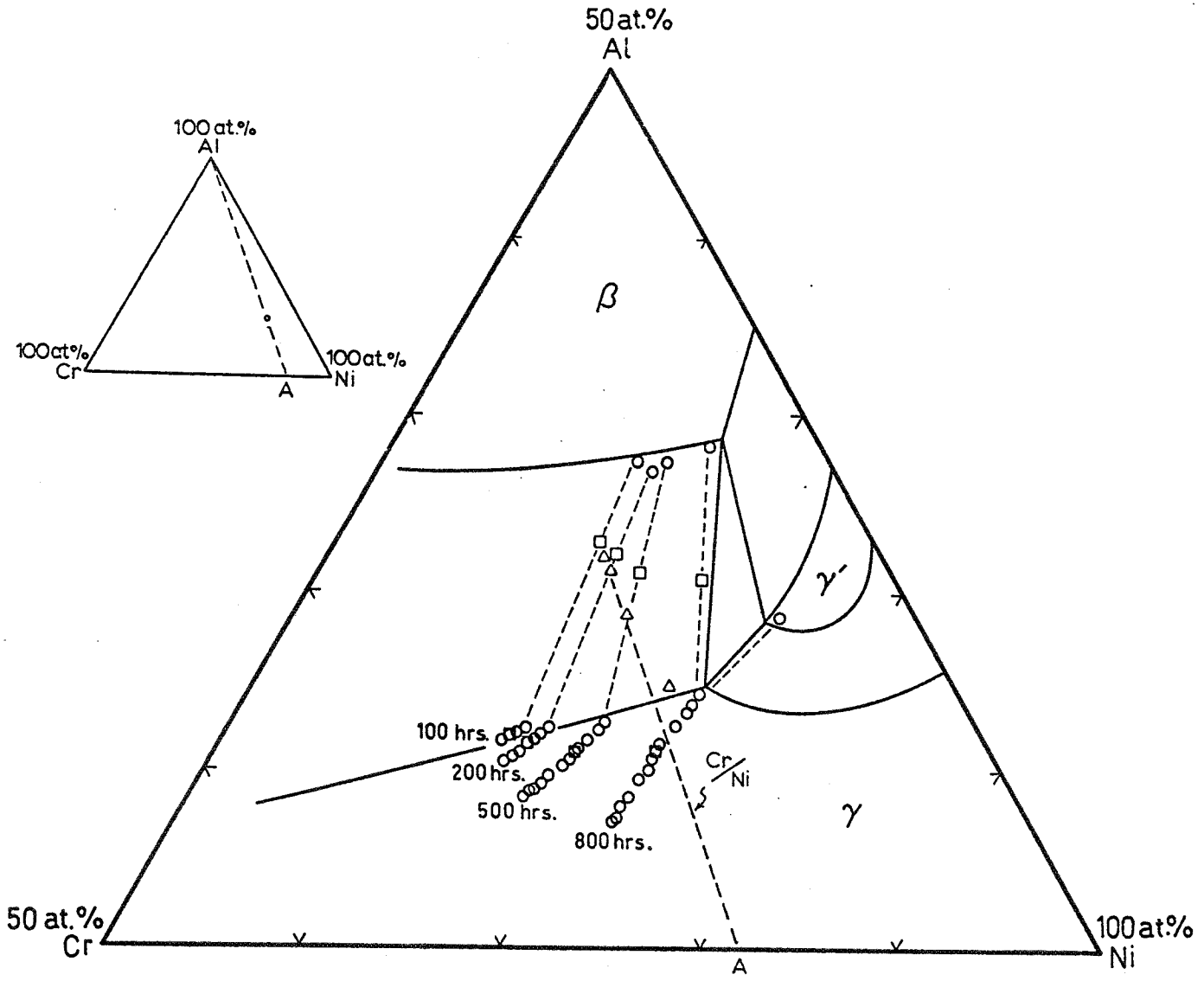

Figure 11. Diffusion path translation after cyclic oxidation of the Ni-13Cr-25Al-0.05Zr alloy.

The diffusion path translation results as a natural consequence of losing Al from the finite sample coupons during the oxidation process. Since the average composition of the γ layer resides to the left, or Cr-rich, side of the line of constant Cr/Ni ratio, the average composition of the $\gamma + \beta$ region must lie to the right, or Cr-poor, side of the line of constant Cr/Ni ratio. As the average composition of the $\gamma + \beta$ region shifts away from the Cr corner, the concentration in the γ phase at the $\gamma/\gamma + \beta$ interface also shifts in the same direction. The shifts in the concentration at the $\gamma/\gamma + \beta$ interface tend to "pull" the diffusion paths in the γ phase away from the Cr corner, resulting in the observed translation of the diffusion paths. The decrease in the volume fraction of the β phase with increasing oxidation time (Figure 9) is a result of the changing average composition in the $\gamma + \beta$ region associated with diffusion path translation.

Diffusion path translation requires diffusion to occur in the $\gamma + \beta$ region of the alloy. It is apparent that the average composition of the $\gamma + \beta$ region increases in Ni concentration (Figure 10). Therefore, Ni must diffuse into the $\gamma + \beta$ region as Al and/or Cr diffuse from the region. The fact that there were no measurable concentration gradients in the $\gamma + \beta$ region suggests that the region behaves as a thin, finite section; i.e., the average composition of the region changes uniformly with negligible concentration gradients.

The Ni atoms must diffuse up the Ni concentration gradient in the γ layer in order to enter the $\gamma + \beta$ region. A mass balance of Ni at the $\gamma/\gamma + \beta$ interface, when considering the interface motion, requires the diffusion of Ni into the $\gamma + \beta$ region. The diffusion of Ni up its own concentration gradient is permissible when the Ni flux is significantly influenced by the concentration gradients of either Cr or Al. Diffusion of Al down its own concentration gradient in the γ layer from the $\gamma + \beta$ region is supported by both the decrease

in the average Al concentration in the $\gamma + \beta$ region (Figure 10) and by mass balance considerations regarding the motion of the $\gamma/\gamma + \beta$ interface. The interface motion also requires a flux of Cr atoms toward the moving interface (Appendix C). Since the average Cr concentration in the $\gamma + \beta$ region decreases with increasing oxidation time (Figure 11), part of the Cr supply comes from transport of Cr in the $\gamma + \beta$ region to the $\gamma/\gamma + \beta$ interface. In addition, since the average Cr concentration in the γ layer also decreases with increasing oxidation time (Figure 11), Cr must also diffuse down the Cr concentration gradient in the γ layer to the $\gamma/\gamma + \beta$ interface. Therefore, changes in the average composition of both the $\gamma + \beta$ region and the γ layer, along with mass balance considerations at the $\gamma/\gamma + \beta$ moving interface, suggest that Al and Cr diffuse down their respective concentration gradients while Ni diffuses up its own concentration gradient.

Diffusion of Ni away from the oxide/γ-layer interface is not contradicted by the observation of mixed Ni oxides in the scale (Table II). Considerable oxide cracking or spalling to the metal substrate would allow a high concentration of oxygen to contact the metal. Significant amounts of NiO may initially form and rapidly grow since Ni is the most abundant species at the oxide/metal interface. As Al diffuses to the interface, the Al will react with the NiO to form the more thermodynamically stable $NiAl_2O_4$. When the NiO is completely converted, an Al_2O_3 scale will form below the $NiAl_2O_4$. Figure 12 shows a duplex scale structure for the Ni-13Cr-25Al-0.05Zr alloy after 800 hours of cyclic oxidation. The area indicated A is the metal substrate containing obvious oxide grain imprints. The rough area designated B was determined by energy-dispersive spectroscopy (EDS) to contain roughly 60% Cr, 30% Ni, and 10% Al, probably a mixture of $NiCr_2O_4$ and $NiAl_2O_4$ spinels. The area designated C shows columnar grains containing mainly Al, most

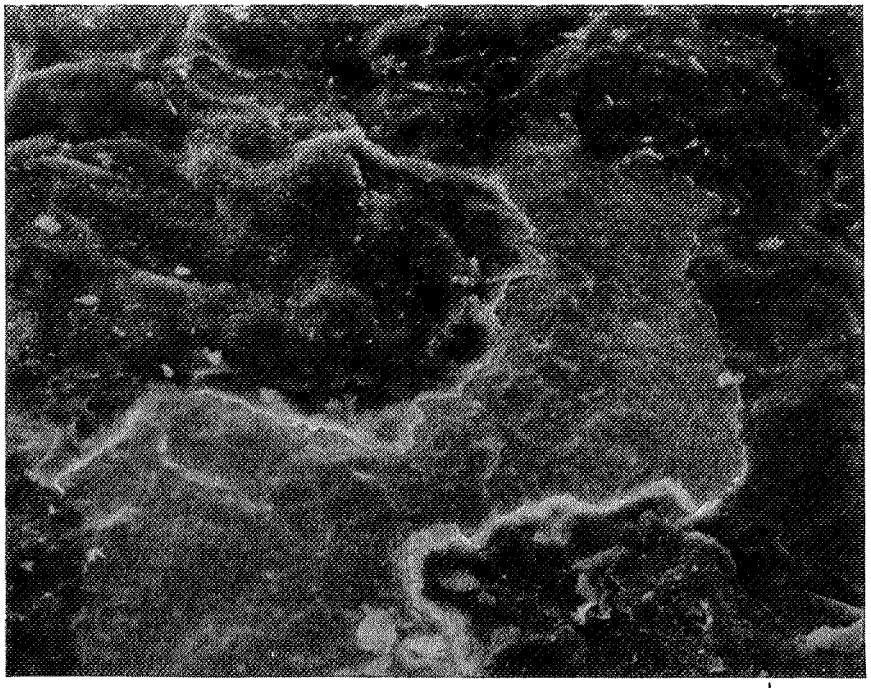

a

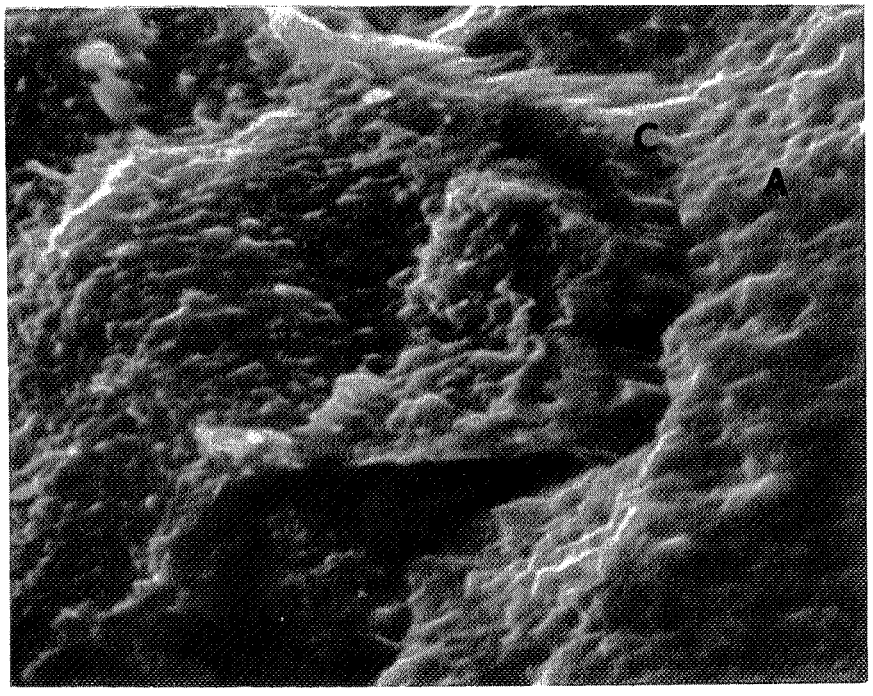

b

Figure 12. Scanning electron micrograph of the surface oxide scale on the Ni-13Cr-25Al-0.05Zr alloy after 800 oxidation cycles. a. oxide scale (dark) and metal substrate where oxide has spalled (light), (600x); b. high magnification of oxide scale edge showing duplex oxide structure; note oxide imprints in the metal substrate, A; mixed spinel oxides, B; and columnar Al_2O_3 grains, C. (2400x)

probably Al_2O_3 (oxygen could not be detected with the EDS), growing below the spinels into the metal substrate. The explanation of initial NiO formation converting to a spinel with subscale formation of Al_2O_3 is similar to models of transient oxide formation during isothermal oxidation (5,21,23).

Ni-14Cr-24Al-0.07Zr

The oxide scale provided by this alloy affords greater oxide protection during cyclic oxidation than the previously discussed Ni-13Cr-25Al-0.05Zr alloy with approximately the same composition. The present 0.07Zr alloy was alloyed with Zr by induction melting elemental Ni, Cr, and Al in zirconia crucibles, allowing the Zr to be leached from the crucible. Two points are immediately obvious in a comparison of the microstructures and concentration profiles of each alloy. First, the γ layer of the 0.07Zr alloy is much less than the previously discussed 0.05Zr alloy, both after 800 oxidation cycles (Figure 13). Secondly, the Al concentration at the oxide/metal interface after 800 oxidation cycles is considerably greater for the 0.07Zr alloy than that for the 0.05Zr alloy after 800 or even 500 oxidation cycles. The concentration/distance profiles for the 0.07Zr alloy are shown as open points in Figure 10. The concentration profiles (Figure 10), taken together with the difference in the γ-layer widths (Figure 13) and the weight change data (Figure 4), indicate that the 0.07Zr alloy possesses much better spalling characteristics than the 0.05Zr alloy. A study of the effect of the Zr concentration on the cyclic oxidation of NiCrAlZr alloys by Barrett, Kahn, and Lowell (48) indicates that the difference in the Zr content of the two alloys does not explain the variation observed in their oxidation behavior. Hence it appears that the variation in the cyclic oxidation behavior may be attributable to the method of alloying the Zr and that Zr pick-up from the zirconia crucibles during the induction melting process improves the cyclic oxidation behavior of these alloys. The

Cyclic

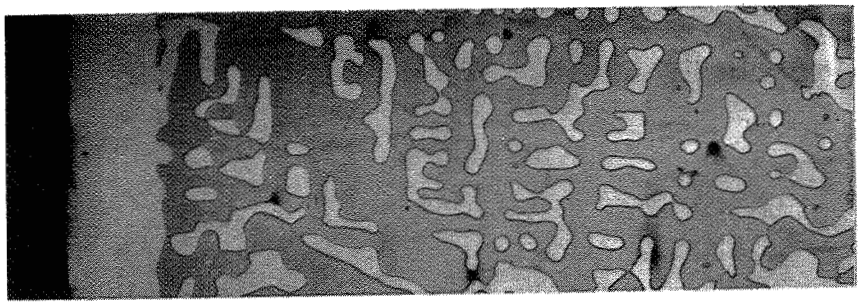

Ni-13Cr-25Al-0.05Zr 200 hrs.

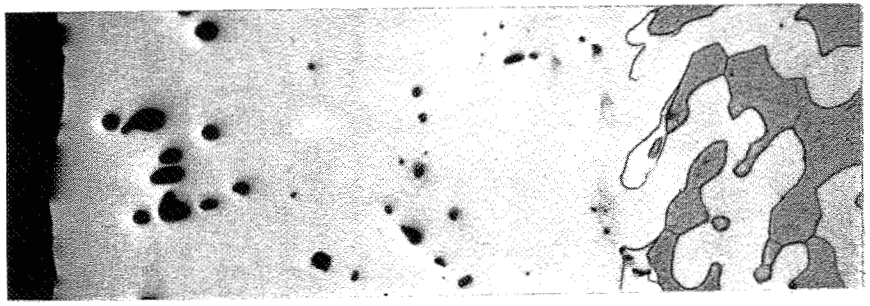

Ni-13Cr-25Al-0.05Zr 800 hrs.

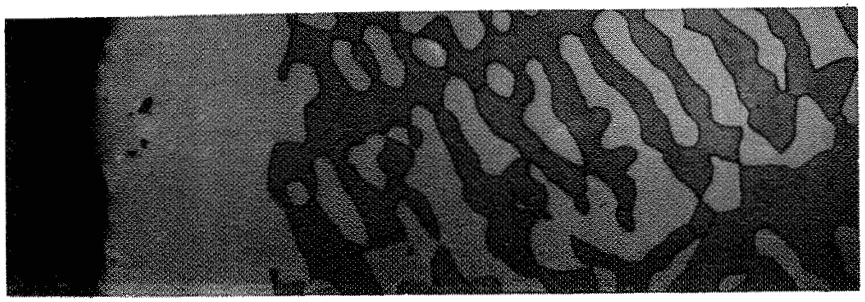

Ni-14Cr-24Al-0.07Zr 800 hrs.

Isothermal

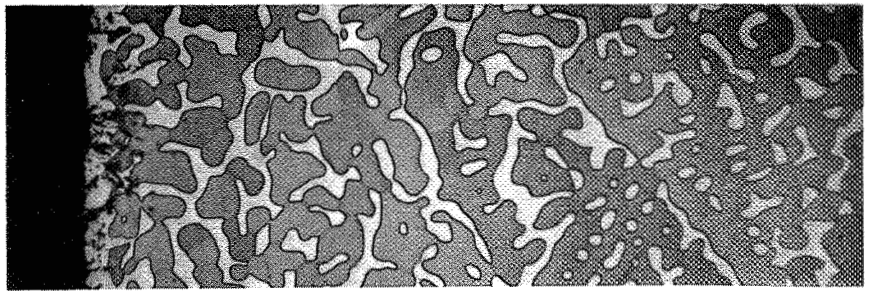

200 hrs. Ni-14Cr-24Al-0.07Zr

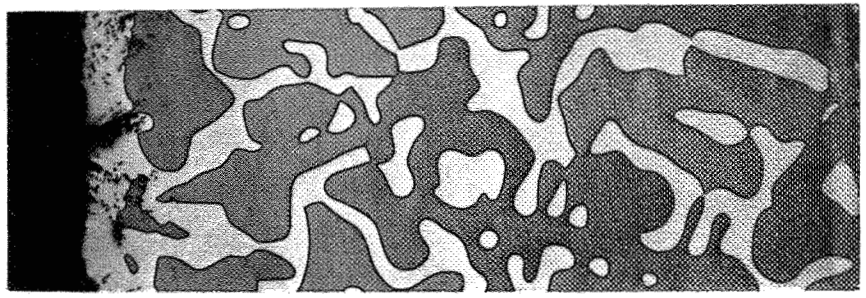

1000 hrs. Ni-14Cr-24Al-0.07Zr

Figure 13. Cyclic and Isothermal oxidation of Ni-13Cr-25Al-0.05Zr alloy and Ni-14Cr-24Al-0.07Zr alloy. All micrographs at 100x.

improved cyclic oxidation behavior resulting from Zr pick-up from the zirconia crucibles is under further investigation at the NASA-Lewis Research Center (57).

The Ni-14Cr-24Al-0.07Zr alloy was also examined after isothermal oxidation for 200 and 1000 hours at 1200°C. The γ-layer width after isothermal oxidation is very slight in comparison to the width following cyclic oxidation. The γ-layer widths and resulting microstructures after isothermal and cyclic oxidation of the 0.07Zr alloy and the cyclic oxidation of the 0.05Zr alloy are compared in Figure 13. The β phase in both alloys underwent considerable coarsening during the high-temperature exposure. The volume fraction of the β phase remained essentially constant during isothermal oxidation (0.64 - 0.68), whereas the volume fraction of the β phase significantly decreased during cyclic oxidation. The difference in the volume fractions of the β phase is directly attributable to the lack of any significant diffusion path translation in the isothermally oxidized alloy. The relatively large loss of Al during cyclic oxidation results in significant diffusion path translation, changes in the average composition of the γ + β region, and consequently, a change in the volume fraction of the β phase.

Limited concentration measurements in the γ layer after isothermal oxidation up to 1000 hours indicate a very low Al concentration gradient. A low Al concentration gradient is consistent with the expectation of a low requisite flux during parabolic oxidation. The near-surface γ layer was measured to thicken parabolically with time. The thin black oxide stringers growing in from the oxide scale are common in Zr-containing alloys (27,48). The growth of the oxide stringers into the substrate appears irrespective of the presence of either the γ or β phase (Figure 14). EDS analysis of the stringers indicates a high Al content (presumably Al_2O_3) with a very slight trace of Zr.

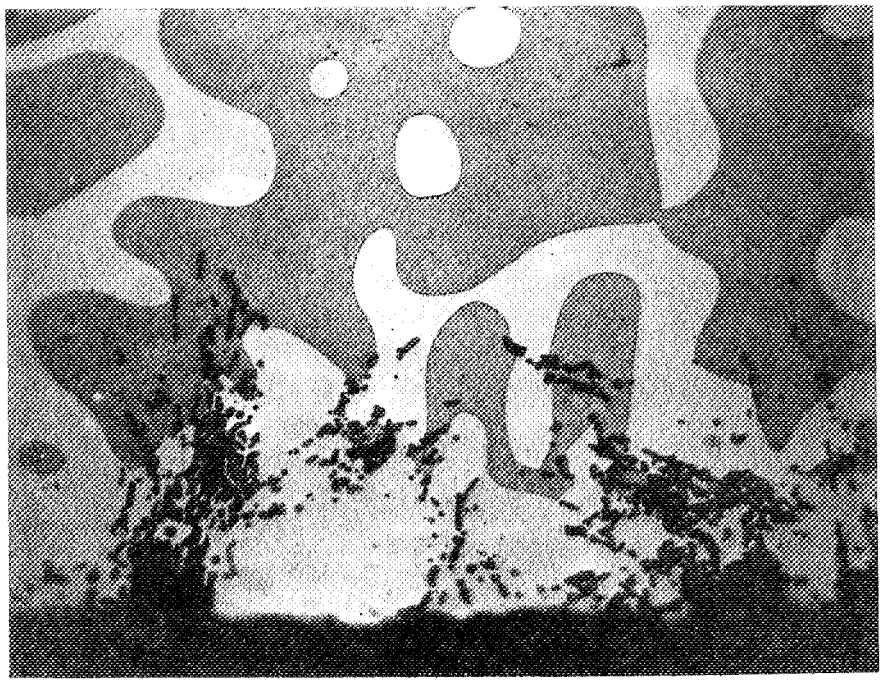

Figure 14. Growth of the Al_2O_3 stringers into the substrate of the Ni-14Cr-24Al-0.07Zr alloy after 1000 hours of isothermal oxidation. (300x)

Ni-19Cr-24Al-0.04Zr

This alloy exhibited the best cyclic oxidation resistance of the four alloys studied. Strong Al_2O_3 formation (Table II) resulted in a low loss of scale during cyclic oxidation, as indicated by the weight change data in Figure 4. The near-surface γ layer increased at a much lower rate than the other cyclically oxidized alloys. Figure 15 shows the alloy microstructures after cyclic oxidation to 1600 hours. The volume fraction of the β phase decreased only slightly from approximately 0.62 to 0.53 after 1600 oxidation cycles.

The good cyclic oxidation behavior of this alloy is reflected in the low Al concentration gradients in the γ layer. A low requisite Al flux associated with good oxide scale adherence results in a very small decrease in the Al concentration at the oxide/metal interface. The concentration/distance profiles are shown in Figure 16. The 800-hour Al concentration profile appears abnormally high, most probably the result of an increased Al content produced at the casting stage. The relatively low loss of Al from this alloy results in a small amount of diffusion path translation, shown in Figure 17. The difference in the concentration profiles resulting from a low, and high, requisite flux condition can be seen by comparing the concentration profiles of the Ni-13Cr-25Al-0.05Zr alloy and the Ni-19Cr-24Al-0.04Zr alloy, shown in Figures 10 and 16, respectively. The obvious difference between the concentration profiles is the Al concentration at the oxide/metal interface. The interfacial Al concentration of the Ni-19Cr-24Al-0.04Zr alloy remains relatively high (> 8 at.% after 1600 hours), whereas the interfacial concentration of the Ni-13Cr-25Al-0.04Zr alloy is considerably lower (< 7.5 at.% after only 800 hours.

The good oxide adherence of Ni-19Cr-24Al-0.04Zr alloy may be due to accommodation of the thermally induced strains by the increasingly convoluted

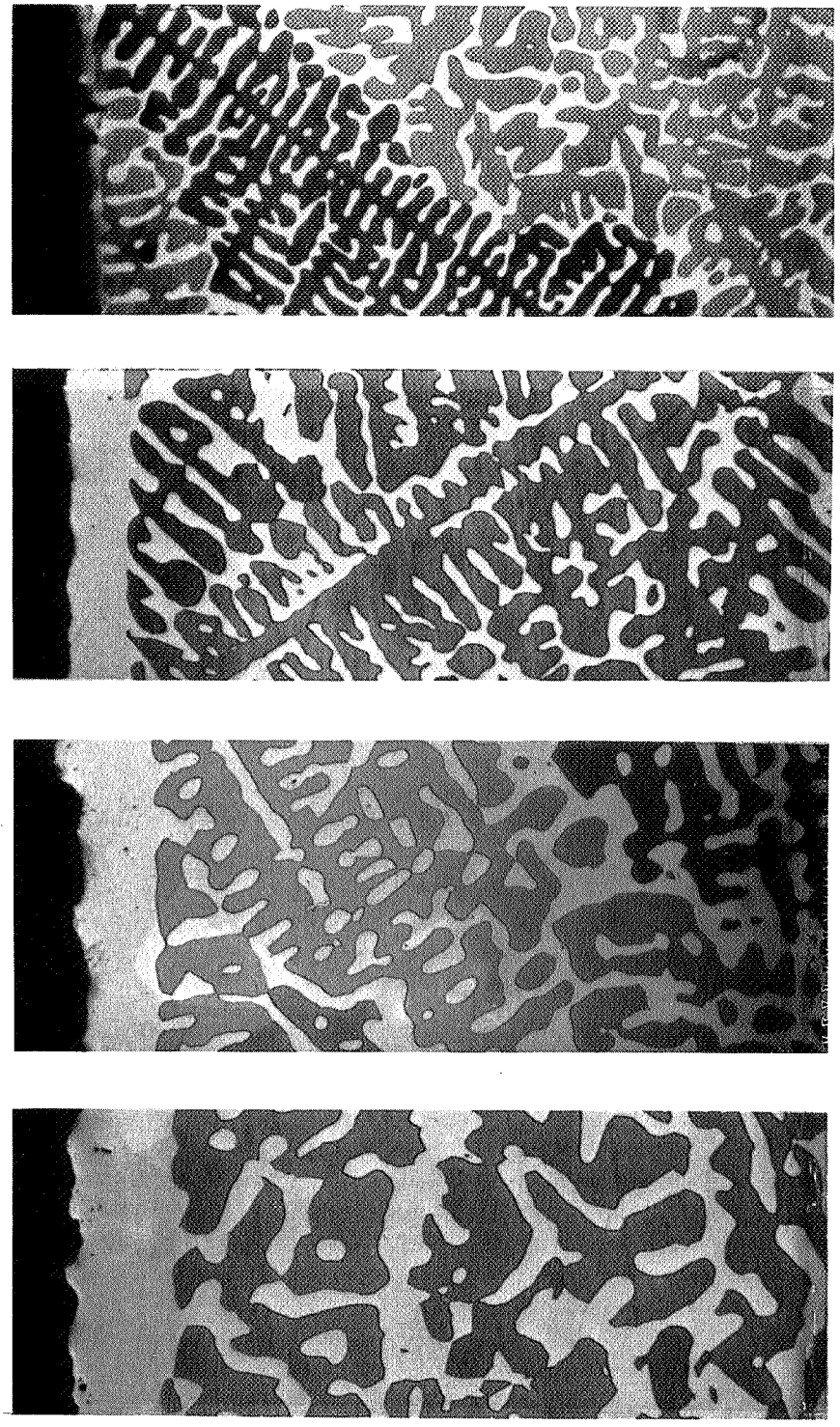

Figure 15. Micrographs of the near-surface γ layer after cyclic oxidation of the Ni-19Cr-24Al-0.04Zr alloy.

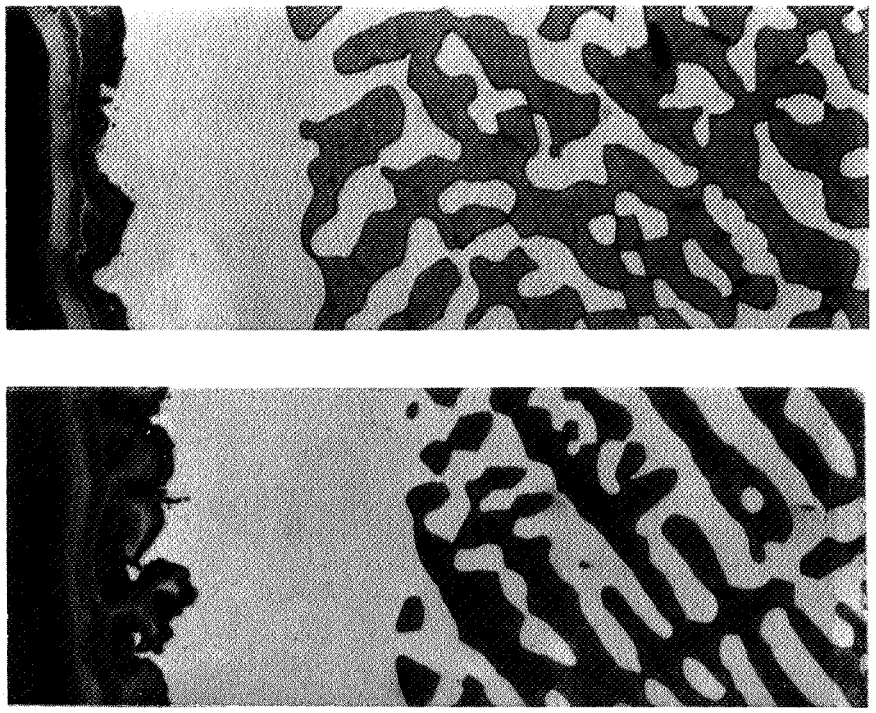

1200 hrs.

1600 hrs.

Figure 15. cont. Ni-19Cr-24Al-0.04Zr alloy.

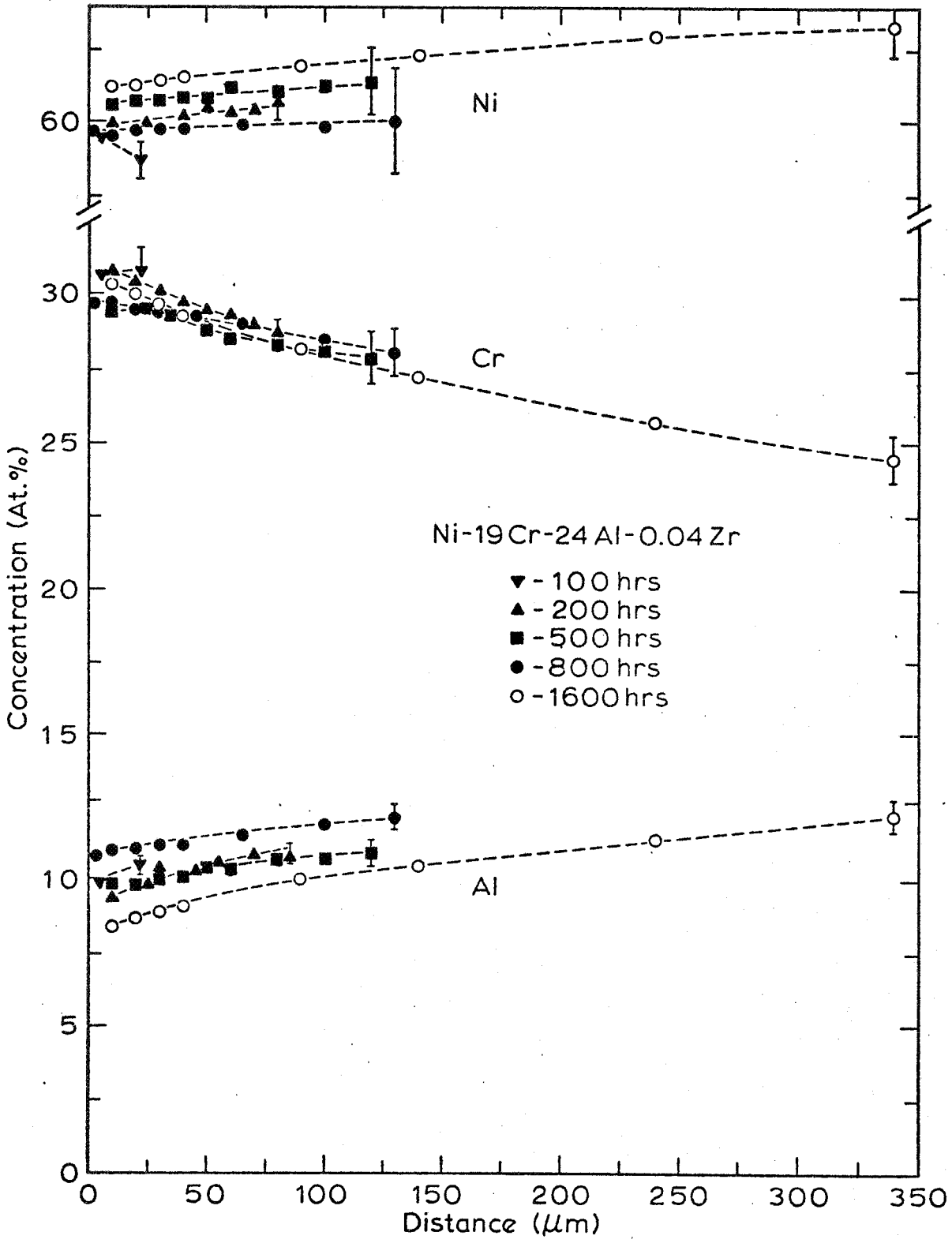

Figure 16. Ni, Cr, and Al concentration/distance profiles in the γ layer after cyclic oxidation of the Ni-19Cr-24Al-0.04Zr alloy.

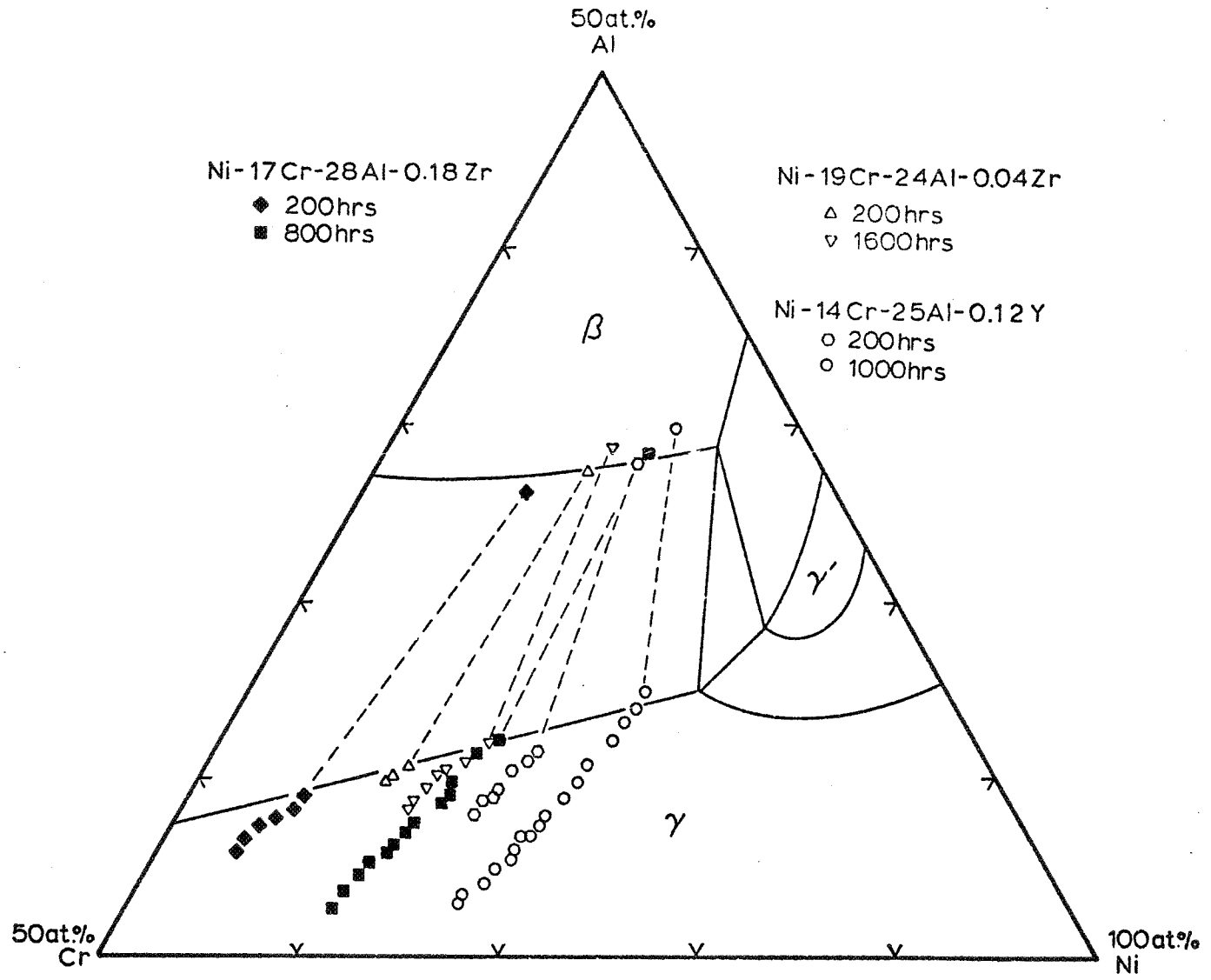

Figure 17. Diffusion path translation after cyclic oxidation of the Ni-19Cr-24Al-0.04Zr, the Ni-14Cr-25Al-0.12Y, and the Ni-17Cr-28Al-0.18Zr alloys.

oxide/metal interface. Oxide ridges are apparent in Figures 6c - 6g. The convoluted oxide/metal interface is also apparent in the micrographs of Figure 15 (800 - 1600 hour exposures). The source containing References 13 and 15 discusses the theoretical and experimental aspects of stress effects and oxide morphologies during oxidation.

Ni-14Cr-25Al-0.12Y

The Y content of this alloy effects cyclic oxidation behavior very similar to that of the Ni-13Cr-25Al-0.05Zr alloy. The near-surface γ layer increases at approximately the same rate for both alloys through 500 hours. The difference at longer times is probably due to different volume distortions which occur in both alloys at the longest oxidation time (Figure 8b). The similarity in the γ-layer width between the two alloys can be observed by comparing the micrographs of the Y-containing alloy (Figure 18) with those of the Zr-containing alloy (Figure 9).

The concentration/distance profiles also exhibit characteristics similar to the Zr-containing alloy. The Al concentration at the oxide/metal interface significantly decreases with increasing oxidation time, while the Al concentration at the $\gamma/\gamma+\beta$ interface similarly increases as a result of diffusion path translation. The concentration/distance profiles are shown in Figure 19. Two Al concentration profiles are shown for the 1000-hour sample near the oxide/metal interface. The lower Al concentration profile resulted from measuring the concentrations in the metallic sections which extended past the average oxide/metal interface position. The diffusion path translation is shown in Figure 17.

Two important points are worth noting in a comparison of the Y- and Zr-containing alloys. First, the Al concentration at the $\gamma/\gamma+\beta$ interface is approximately the same for both alloys at each oxidation time. This similarity

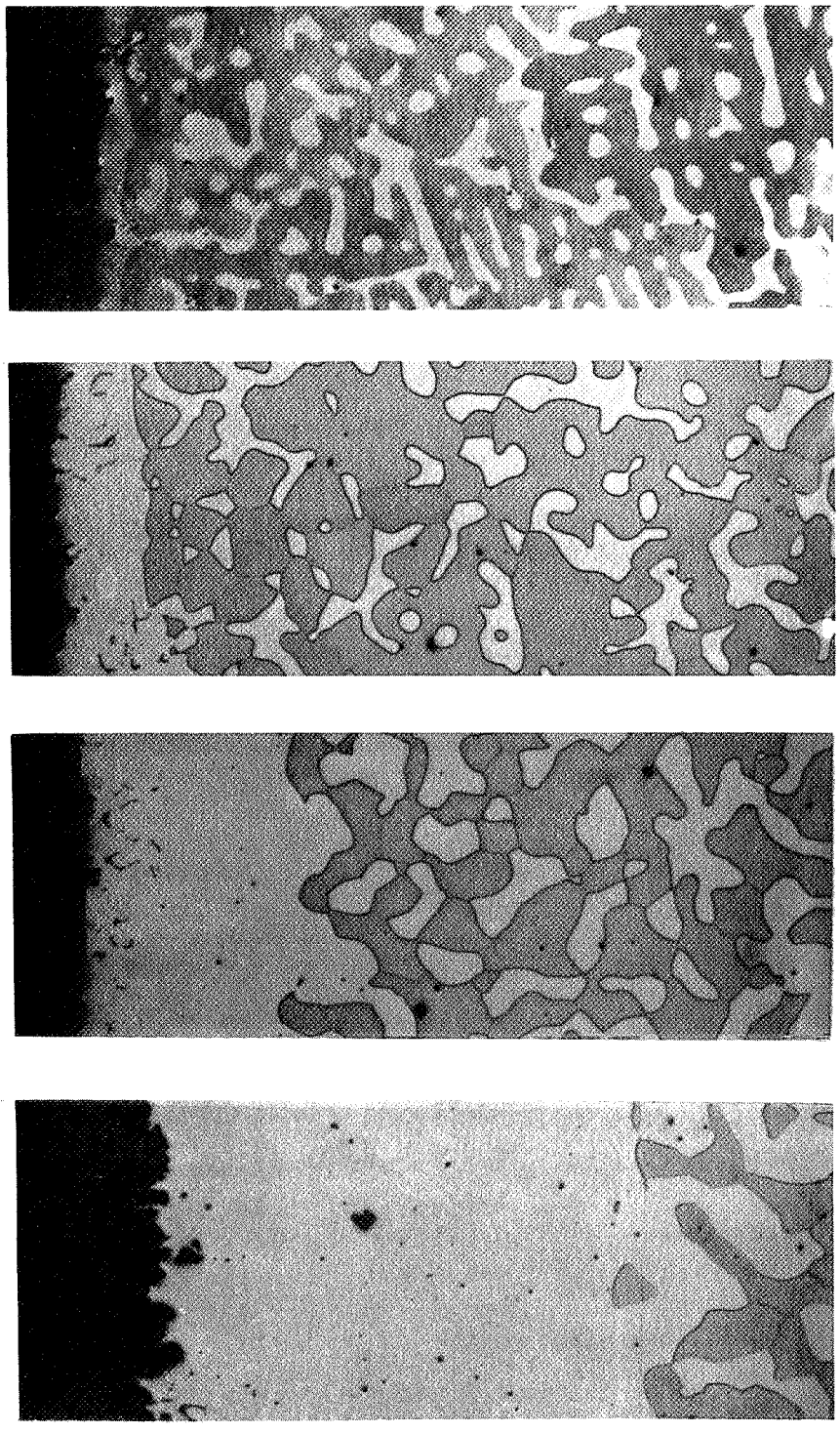

Figure 18. Micrographs of the near-surface γ layer after cyclic oxidation of the Ni-14Cr-25Al-0.12Y alloy.

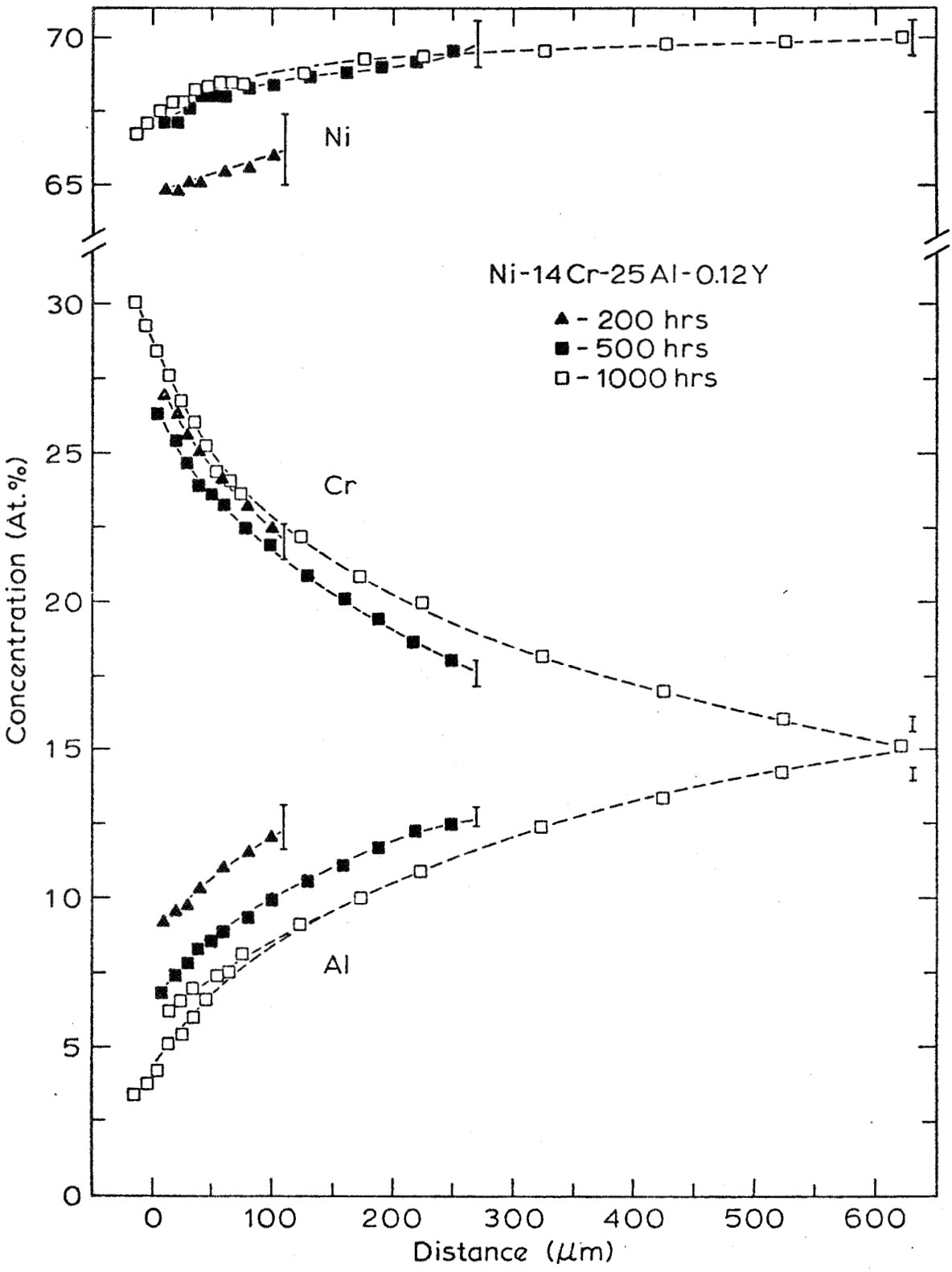

Figure 19. Ni, Cr, and Al concentration/distance profiles in the γ layer after cyclic oxidation for the Ni-14Cr-28Al-0.12Y alloy.

implies that Y does not significantly affect the maximum solubility of Al in the γ phase. It is also shown in Appendix B that Zr does not appear to significantly affect this solubility. Second, although both alloys have approximately the same γ-layer width after equivalent oxidation times, the Al concentration gradient in the Y-containing alloy is greater than that in the Zr-containing alloy. The similar γ-layer widths imply that both alloys have lost Al at approximately the same rate, further implying that both alloys have approximately the same requisite flux. The difference in the concentration gradients, but the same requisite flux, suggests that Y adversely affects the supply of Al to the oxide/metal interface. Since Appendix C suggests that the Al flux in the γ layer is mainly dependent on the Al concentration gradient, it may be inferred that Y decreases the Al diffusivity below that in the Zr-containing alloy. A greater concentration gradient is therefore required in the γ layer to supply the same requisite flux as the Zr-containing alloy.

The oxide stringers observed after oxidation of Y-containing alloys are generally attributed to the selective oxidation of grain-boundary yttrides. Figure 20 shows the selective oxidation of a grain boundary yttride after 100 hours of cyclic oxidation of the Ni-14Cr-25Al-0.12Y alloy. EDS analysis of the unoxidized portion of the yttride indicated a composition of mainly Ni with lesser amounts of Y and trace amounts of Al and Cr.

Ni-17Cr-28Al-0.18Zr

The high Zr content of this alloy effects poor oxide spalling characteristics similar to the Ni-13Cr-25Al-0.05Zr and Ni-14Cr-25Al-0.12Y alloys. The Al content, being the highest in this alloy, results in a lower growth rate of the near-surface γ layer while still supplying Al to the oxide scale at approximately the same rate as the Ni-13Cr-25Al-0.05Zr and the Ni-14Cr-25Al-0.12Y alloys. The width of the γ layer in the Ni-17Cr-28Al-0.18Zr alloy is shown in

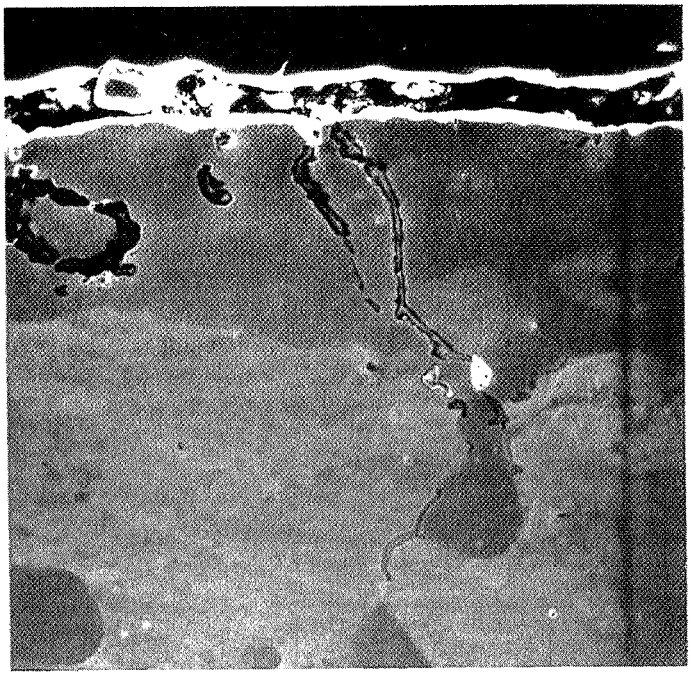

Figure 20. Selective oxidation of grain boundary yttrides on the Ni-14Cr-25Al-0.12Y alloy after cyclic oxidation for 100 hours. (500x)

Figure 21. The high Zr content also results in an increased occurrence of Al_2O_3 stringers in the γ layer, apparent in Figure 21. The increased number of oxide stringers accounts for the abnormally large, positive weight change during cyclic oxidation (Figure 4).

More interesting in the Ni-17Cr-28Al-0.18Zr alloy is the occurrence of localized breakaway oxidation after 500 and 800 oxidation cycles. Internal oxidation of Al, signaling external formation of less protective oxides of Ni and Cr, is shown in Figure 22. An increased slope in the weight change data after approximately 500 oxidation cycles (Figure 4), indicating rapid spallation of poorly adherent scales, further attests to the onset of breakaway oxidation. Breakaway oxidation occurs in localized regions because of the non-uniform nature of oxide spallation from the sample surface. The x-ray maps of Figure 23 show Cr-rich oxides (probably Cr_2O_3) forming in an internally oxidized subscale region indicating significant oxygen influx into the alloy. Figure 22 also shows a partial link-up of Al_2O_3 precipitates at the boundary between the γ layer and the internally oxidized zone.

Breakaway oxidation results from a failure of the alloy to supply the requisite Al flux for sole formation and growth of an Al_2O_3 oxide scale. As was evident from the previously discussed alloys, the Al concentration at the oxide/metal interface decreased with time, increasing the Al concentration gradient in the γ layer, and allowing the alloy to supply the requisite flux to the oxide scale. Decrease of the interfacial Al concentration to zero prevents further supply of the requisite flux, and less-protective oxides will eventually form. Formation of less-protective oxides permit a high influx of oxygen into the alloy substrate internally oxidizing the Al. Further oxidation results in either total internal oxidation of the Al in the sample, with rapid spalling of Ni and Cr oxides, or internal oxide link-up resulting in a

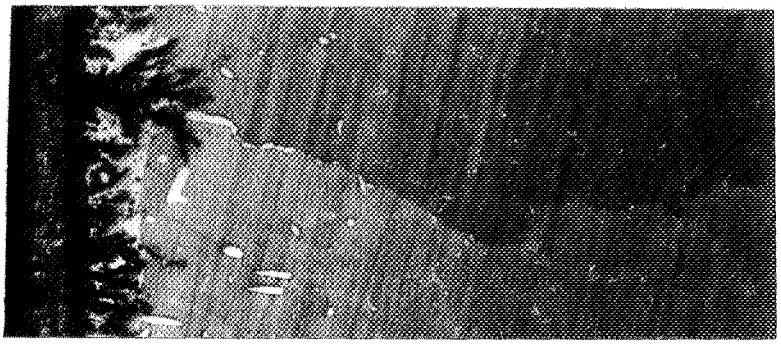

100 hrs.

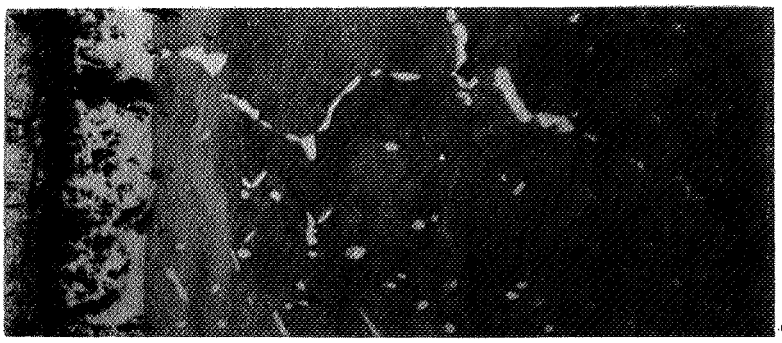

200 hrs.

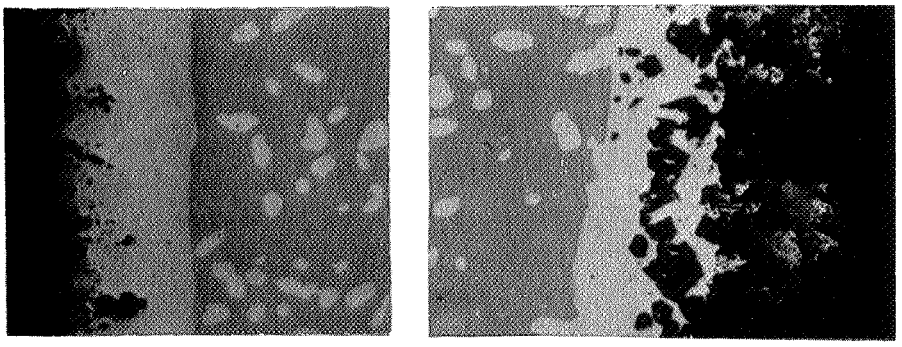

500 hrs.

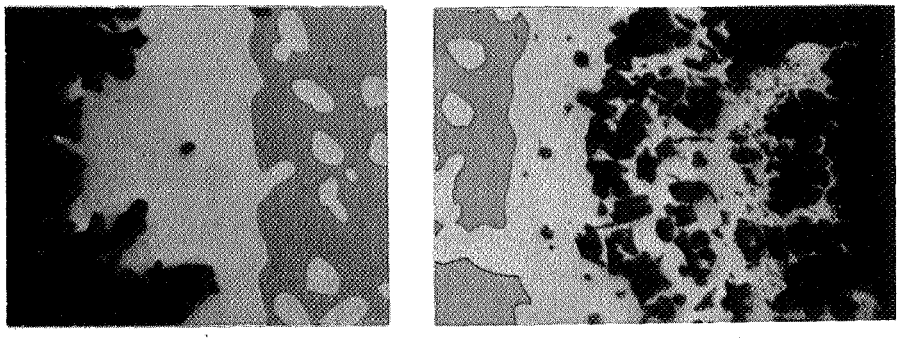

800 hrs.

Figure 21. Micrographs of the near-surface γ layer after cyclic oxidation of the Ni-17Cr-28Al-0.18Zr alloy.

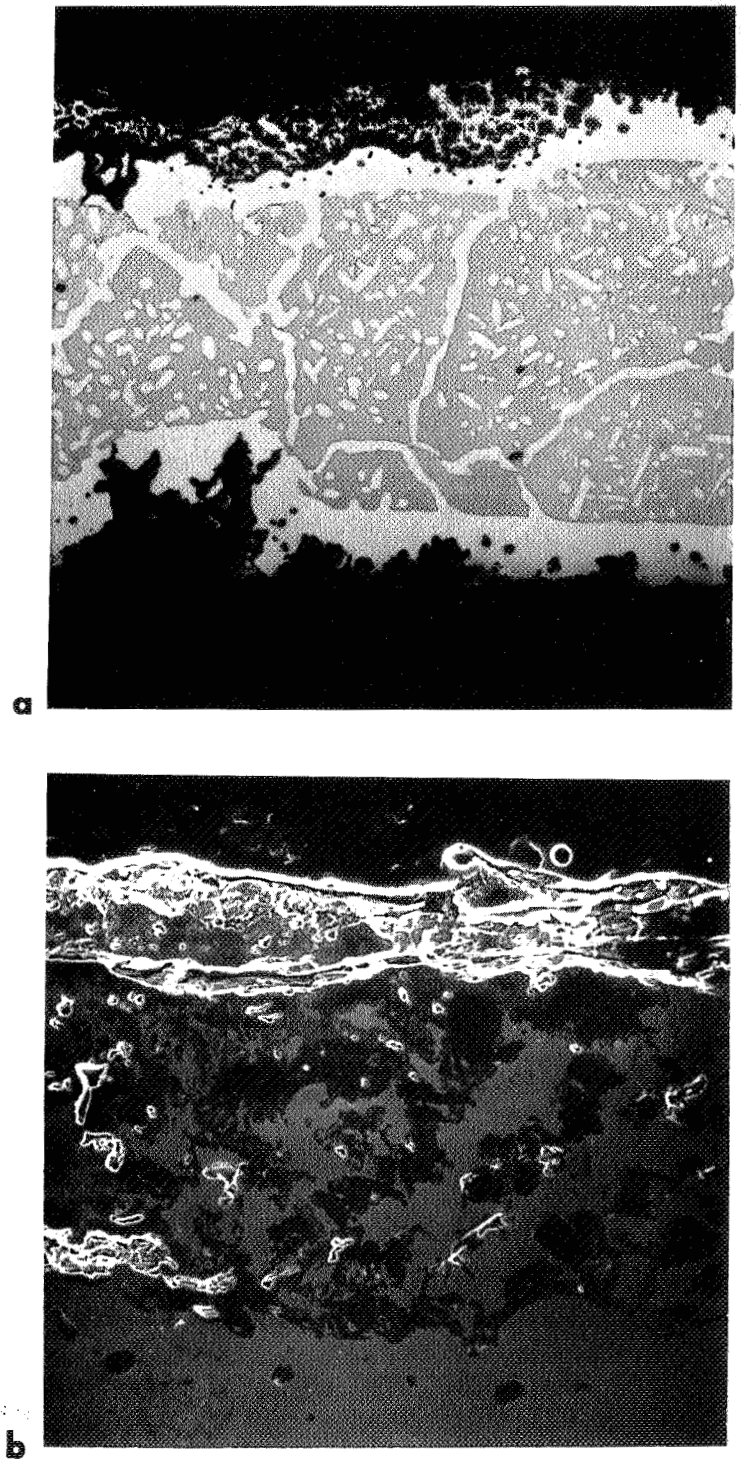

Figure 22. Localized breakaway oxidation of the Ni-17Cr-28Al-0.18Zr alloy after 800 oxidation cycles a. (30x) b. Internal oxidation of Al and some Cr. (180x)

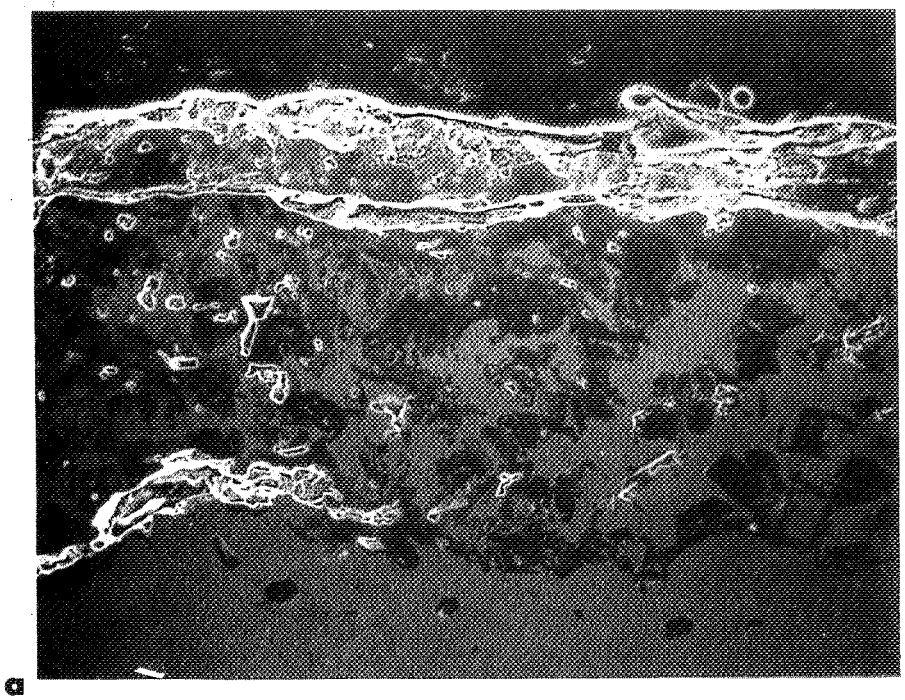

a

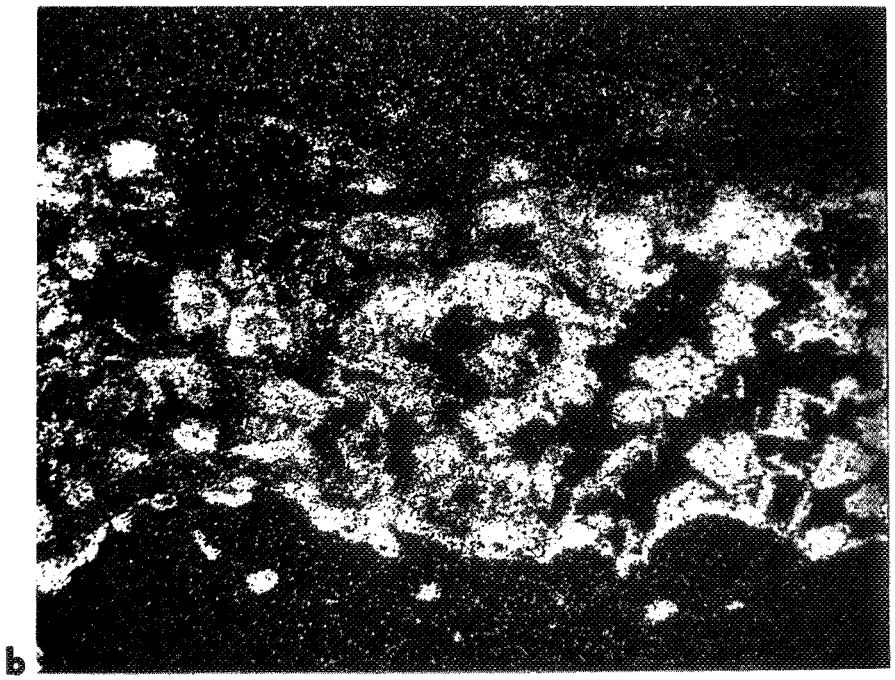

b

Figure 23. X-ray maps of internal oxidation substrate shown in Figure 22. a. Internally oxidized subscale (180x) b. Al x-ray map.

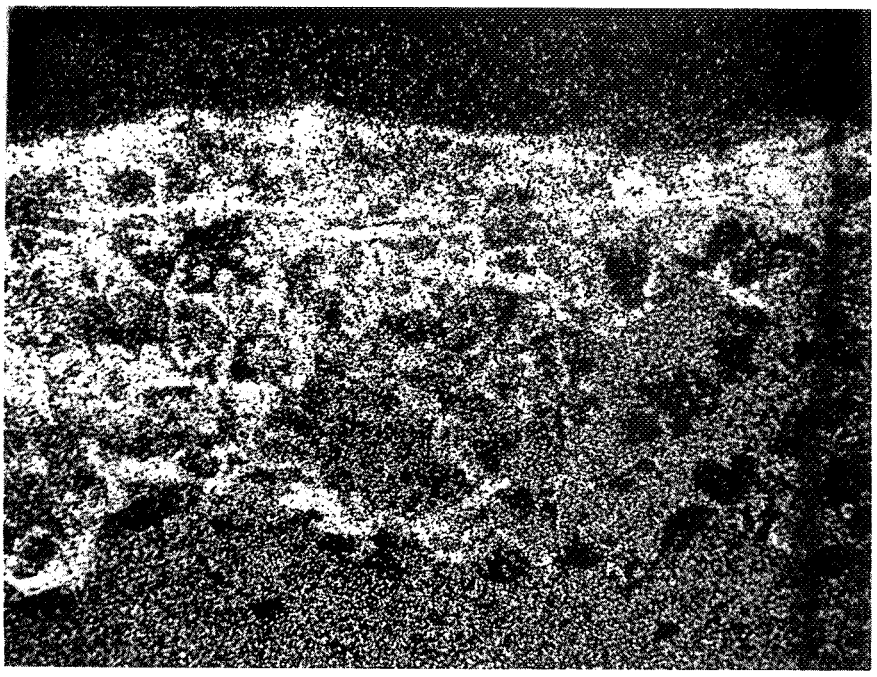

c

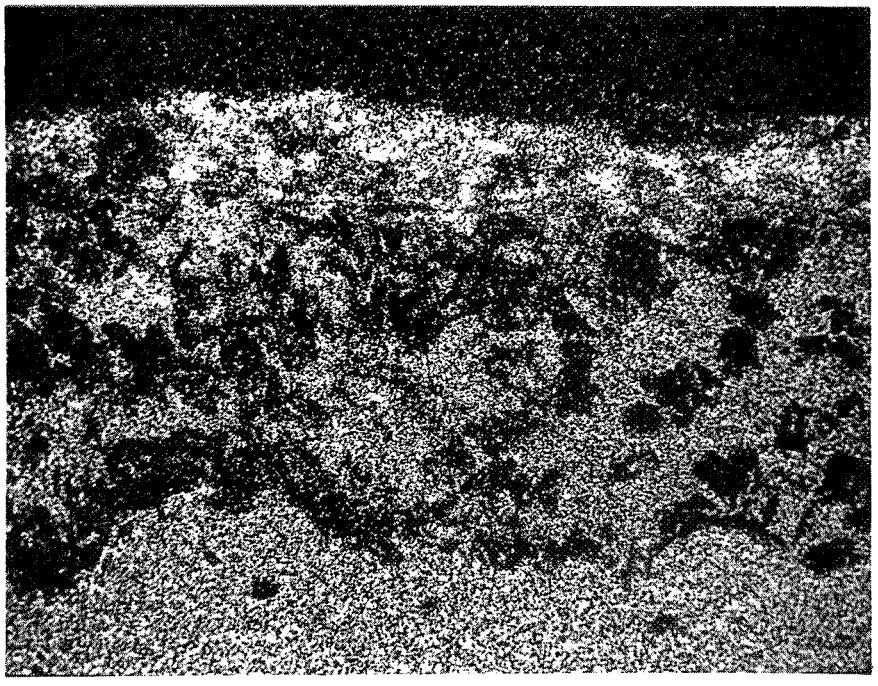

d

Figure 23. cont. c. Cr x-ray map d. Ni x-ray map.

new Al_2O_3 protective barrier. The greater the volume fraction of internally-oxidized precipitates deposited, the more tortuous the path the incoming oxygen must travel and the greater the chance of precipitate link-up establishing a continuous, protective oxide scale. Rapp (58) has reviewed the theoretical and experimental work regarding the solute concentration and diffusivity necessary for the transition from internal oxidation to the formation of an external, continuous oxide scale. It is apparent from Figure 23 that the supply of Al to the internal oxidation/γ-layer interface is sufficient to reestablish a continuous Al_2O_3 barrier by link-up of the Al_2O_3 precipitates.

The Al concentration at the oxide/metal interface for the Ni-17Cr-28Al-0.18Zr alloy decreases to nearly zero after 800 oxidation cycles. The Al concentration profiles showed a significant difference in concentrations between the five to eight profiles measured at various locations along the sample surface. The profiles are shown in Figure 24. The two error bars below the Al concentration profiles are indicative of the differences between various concentration profiles measured on the same sample. The concentrations at the $\gamma/\gamma+\beta$ interface change in accordance with the diffusion path translation shown in Figure 17.

The occurrence of breakaway oxidation on the 500 and 800 hour samples results from a failure of the alloy to supply the requisite flux when the Al concentration at the oxide/metal interface decreased to nearly zero. It is interesting to note that this alloy with the highest Al content (28 at.%) undergoes breakaway oxidation before the alloys with less Al, even though the requisite Al flux and the weight of Al consumed in this alloy will be shown to be similar to that in the Ni-13Cr-25Al-0.05Zr and Ni-14Cr-25Al-0.12Y alloys. This point will be discussed further in the next section.

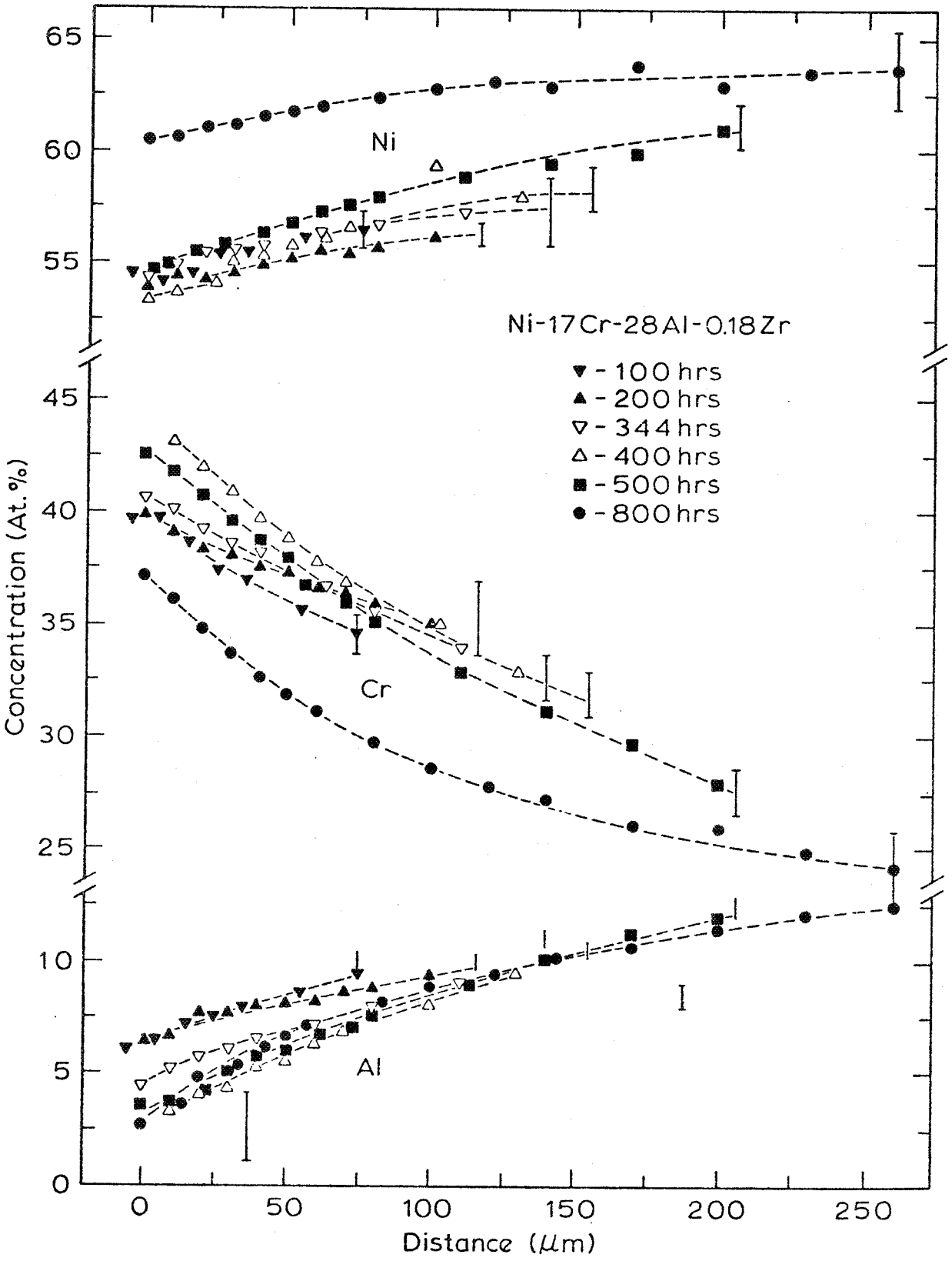

Figure 24. Ni, Cr, and Al concentration/distance profiles in the γ layer after cyclic oxidation for the Ni-17Cr-28Al-0.18Zr alloy.

Summary

The observations concerning the Al transport during the cyclic oxidation of NiCrAlZr(Y) alloys will be briefly reviewed. The differences between isothermal and cyclic oxidation will also be noted. The observations from the experimental analysis are:

1. Oxide spallation during thermal cycling results in a more rapid loss of Al over that which occurs during isothermal oxidation. The accelerated loss of Al is due to the higher requisite flux associated with cyclic oxidation.
2. Repeated oxide spallation results in a decreasing Al concentration at the oxide/γ-layer interface. The interfacial Al concentration decreases, increasing the concentration gradient, in order to supply the higher requisite flux. No measurable decrease in the interfacial Al concentration was observed during isothermal oxidation.
3. The rate of Al decrease at the oxide/γ-layer interface was in proportion to the severity of the oxide spallation. The Ni-13Cr-25Al-0.05Zr, the Ni-14Cr-25Al-0.12Y, and the Ni-17Cr-28Al-0.18Zr alloys, all with poor spalling characteristics, exhibited large decreases in the interfacial Al concentration after 800 - 1000 hours. In comparison, the Ni-19Cr-24Al-0.04Zr alloy, with good spalling characteristics, exhibited a small decrease in the interfacial concentration after 1600 hours.
4. Breakaway oxidation was observed when the Al concentration at the oxide/γ-layer interface decreased to approximately zero in the Ni-17Cr-28Al-0.18Zr alloy. Breakaway oxidation resulted from a failure of the alloy to continue to supply the requisite flux.
5. The γ-layer width following cyclic oxidation was considerably greater

than that observed after isothermal oxidation. The growth rate of the γ layer in the cyclically oxidized alloys reflects the influence of the increased requisite flux associated with oxide spallation.

6. The loss of Al from finite samples led to diffusion path translation, changes in the composition of both phases in the $\gamma + \beta$ region, and a decrease in the volume fraction of the β phase. The isothermally oxidized alloys, having lost relatively little Al, showed insignificant diffusion path translation or decrease in the volume fraction of the β phase.

NUMERICAL MODELING RESULTS AND DISCUSSION

Numerical Modeling

Numerical models may be used to simulate and predict the diffusional transport in alloys at elevated temperatures. Most numerical models are based on finite-difference techniques which permit considerable flexibility when a closed-form analytical solution is not possible. The flexibility of a numerical model allows incorporation of concentration-dependent diffusion coefficients, complex boundary conditions, non-isothermal temperature conditions, and overlapping diffusion fields. A number of binary and ternary numerical models utilizing finite-difference techniques have been developed to simulate diffusion under various conditions (59-62). Even with the increased flexibility, numerical models still require some assumptions in order to determine a solution.

Numerical modeling of atomic diffusion in systems containing moving boundaries requires solution of Fick's second law in all single-phase regions constrained by mass balances at the moving boundaries. If concentration-independent diffusion coefficients are assumed, Fick's second law for the NiCrAl system can be stated as (63):

$$\frac{dC_{Al}}{dt} = D_{AlAl}\frac{d^2C_{Al}}{dx^2} + D_{AlCr}\frac{d^2C_{Cr}}{dx^2} \qquad (1a)$$

$$\frac{dC_{Cr}}{dt} = D_{CrAl}\frac{d^2C_{Al}}{dx^2} + D_{CrCr}\frac{d^2C_{Cr}}{dx^2} \qquad (1b)$$

where C_{Al} and C_{Cr} are the Al and Cr concentrations, respectively. The parameters x and t refer to distance and time, respectively. The four diffusion coefficients—D_{AlAl}, D_{CrCr}, D_{AlCr}, and D_{CrAl}—will be defined shortly.

The mass balance at the $\gamma/\gamma+\beta$ interface has the form:

$$(C^{0}_{Al} - C^{\gamma}_{Al}) \frac{d\xi}{dt} = -J^{\gamma}_{Al,\xi} = \left| D_{AlAl} \frac{dC_{Al}}{dx} + D_{AlCr} \frac{dC_{Cr}}{dx} \right|_{\xi} \quad (2a)$$

$$(C^{0}_{Cr} - C^{\gamma}_{Cr}) \frac{d\xi}{dt} = -J^{\gamma}_{Cr,\xi} = \left| D_{CrAl} \frac{dC_{Al}}{dx} + D_{CrCr} \frac{dC_{Cr}}{dx} \right|_{\xi} \quad (2b)$$

where: $\frac{d\xi}{dt}$ = velocity of the $\gamma/\gamma+\beta$ interface,

$J^{\gamma}_{Al,\xi}$ = Al flux in the γ phase evaluated at the $\gamma/\gamma+\beta$ interface,

C^{0}_{Al} = Al concentration in $\gamma+\beta$ region,

C^{γ}_{Al} = Al concentration in the γ phase at the $\gamma/\gamma+\beta$ interface.

The Cr concentration parameters in Eq. 2b are defined similarly to those for the Al. The Al and Cr fluxes are defined by the right-most term within the brackets in Eqs. 2a and 2b. D_{AlAl} and D_{CrCr} in Eqs. 1 and 2 are the main or direct diffusion coefficients relating the Al concentration gradient to the Al flux and the Cr concentration gradient to the Cr flux (right-most terms, Eqs. 2a and 2b), respectively. D_{AlCr} and D_{CrAl} are the cross term, or indirect, diffusion coefficients relating the Cr concentration gradient to the Al flux and the Al concentration gradient to the Cr flux (right-most terms, Eqs. 2a and 2b), respectively. The terms containing D_{AlCr} and D_{CrAl} in Eqs. 1 and 2 are referred to as the cross terms which describe the effect of one component on the diffusion of other components in ternary and more complex systems (63).

Loss of a component from the metal substrate at a free surface results in recession of the metal substrate. The appropriate equation describing the metal recession due to loss of Al from the γ phase in NiCrAl alloys is:

$$\frac{(1-\overline{V}_{Al})}{\overline{V}_{Al}} C^{s}_{Al} \frac{d\xi_2}{dt} = -J^{\gamma}_{Al} \Big|_{\xi_2} \quad (3a)$$

where: $\frac{d\xi}{dt}$ = velocity of the metal substrate recession,

$\overline{V}_{Al}$ = partial molar volume of Al in the γ phase,

C^{s}_{Al} = Al concentration in the γ phase at the oxide/γ-layer interface,

J^{γ}_{Al} = Al flux in the γ phase evaluated at the oxide/γ-layer interface (defined similarly to the right-bracketed term in Eq. 2a).

The greater the partial molar volume of Al, the greater the surface recession caused by loss of Al from the metal substrate.

The second goal of this research consisted in developing a model to simulate the Al diffusion in $\gamma + \beta$ NiCrAl alloys during cyclic oxidation. As previously shown, the diffusion of Al to form an Al_2O_3 oxide scale results in the growth of a near-surface γ layer. The loss of Al from the metal substrate resulted in the recession of the Al_2O_3/γ-layer interface. Hence, it was necessary to determine the Al diffusion in the near-surface γ layer constrained by the $\gamma/\gamma + \beta$ and Al_2O_3/γ-layer moving boundaries. The cross term effect of the Cr concentration gradient was neglected on the basis that D_{AlAl} was much greater than D_{AlCr}, as suggested by the diffusion couple work in Appendix C. Therefore, the Al transport was modeled on the assumption that the Al concentration gradient was the dominant driving force for Al diffusion.

A numerical model was developed capable of predicting Al concentration/distance profiles, the $\gamma/\gamma + \beta$ interface motion, the oxide/γ-layer surface recession, and the weight of Al consumed. In addition, the model could predict the time to breakaway oxidation by predicting the time the Al concentration at the oxide/γ-layer interface approached zero. Seven assumptions were made in the development of the numerical model. They were:

1. The diffusion coefficients were independent of concentration.
2. The $\gamma/\gamma + \beta$ interface was planar.
3. The oxide/γ-layer interface was planar.

4. The partial molar volume of Al was independent of concentration and phase.
5. Sample heat-up and cool-down times were rapid; i.e., diffusion only occurred at 1200°C.
6. Only Al_2O_3 was formed.
7. The driving force for Al was solely the result of the Al concentration gradient.

The finite-difference forms of Fick's second law and the mass balances at each interface were utilized to describe the Al diffusion. The resulting diffusion equations to be solved were:

$$\frac{dC}{dt} = D \frac{d^2C}{dx^2} \tag{4a}$$

in the γ layer;

$$(C^{\gamma} - C^{0}) \frac{d\xi_1}{dt} = J_1^{\gamma}\Big|_{\xi_1} = -D \frac{dC}{dx}\Big|_{\xi_1} \tag{4b}$$

at the $\gamma/\gamma + \beta$ interface; and

$$- \frac{(1 - \bar{V}_{Al})}{\bar{V}_{Al}} C^{s} \frac{d\xi_2}{dt} = J_2^{\gamma}\Big|_{\xi_2} = -D \frac{dC}{dx}\Big|_{\xi_2} \tag{4c}$$

at the oxide/γ-layer interface, where the concentration and flux parameters refer only to Al, and D refers to the diffusion coefficient approximating D_{AlAl} as discussed in Appendix C. All other parameters are described previously for Eqs. 1, 2, and 3.

The boundary condition at the oxide/γ-layer interface may be stated as either a time-dependent flux (J_2^{γ}) or as a time-dependent interface concentration (C^{s}). If the flux (J_2^{γ}) or the specific rate of Al consumption (i.e., the requisite flux) is known, the interfacial Al concentration can be determined from the right-most term in Eq. 4c and Fick's second law in the γ layer (Eq. 4a).

Similarly, if the Al concentration at the interface (C^S) is known, Eqs. 4a and 4c alloy the flux (J_2^γ) to be determined. The interfacial Al concentration (C^S), estimated from the concentration/distance profiles measured on the cyclically oxidized alloys, was input to the model. The range of concentration gradients measured on the cyclically oxidized alloys did not facilitate easy estimation of the flux (J_2^γ).

The time dependence of the Al concentration at the $\gamma/\gamma+\beta$ interface was also input to the model. The Al concentration at this interface increased with time as the diffusion paths translated toward the Ni-rich portion of the phase diagram. The time dependence of the Al concentration at the $\gamma/\gamma+\beta$ interface and at the oxide/γ-layer interface is shown in Figure 25. The finite-difference form of the diffusion equations and the basic operations of the numerical model are described in greater detail in Appendix D. The determination of the diffusion coefficients for each alloy is shown and discussed in Appendix C.

Results and Discussion

Al Concentration Profiles and γ-Layer Widths

The numerical model is able to predict accurately the Al concentration profiles and γ-layer widths through 500 hours for the Ni-13Cr-25Al-0.05Zr alloy. The anomalous volume expansion of this alloy results in the underestimation of the γ-layer width for the 800-hour prediction. The predicted and measured Al concentration/distance profiles are shown in Figure 26.

Similarly, the concentration/distance profiles and γ-layer widths are accurately predicted for the Ni-14Cr-25Al-0.12Y alloy through 500 hours. Again the anomalous volume expansion results in the underestimation of the γ-layer width at 1000 hours. The concentration/distance profiles are shown in Figure 27. The curvature in the 500-hour and 1000-hour Al concentration profiles is greater than the curvature in the predicted profiles. The additional curvature

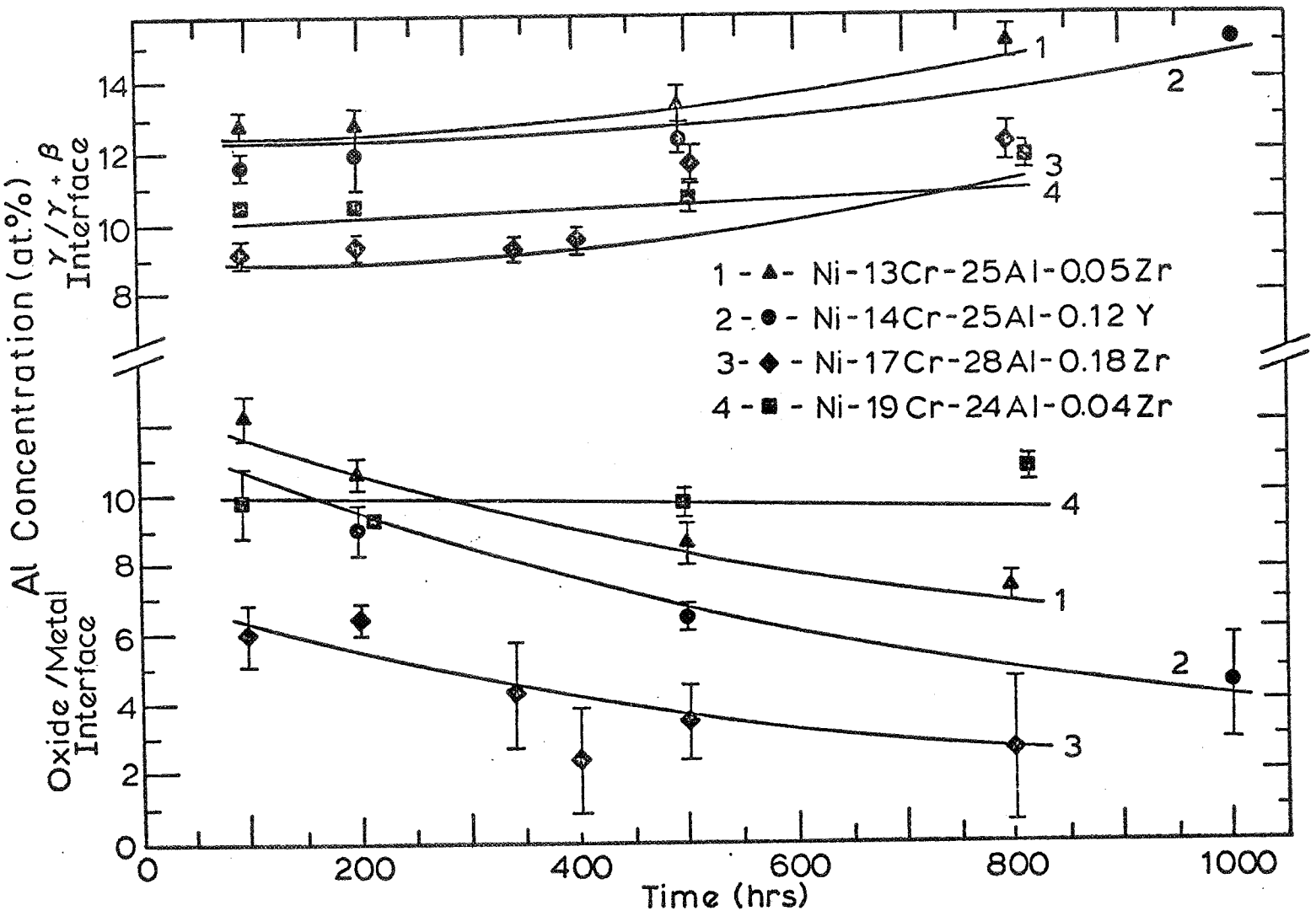

Figure 25. The time dependence of the Al concentration at the γ/γ+β interface and at the oxide/γ-layer interface.

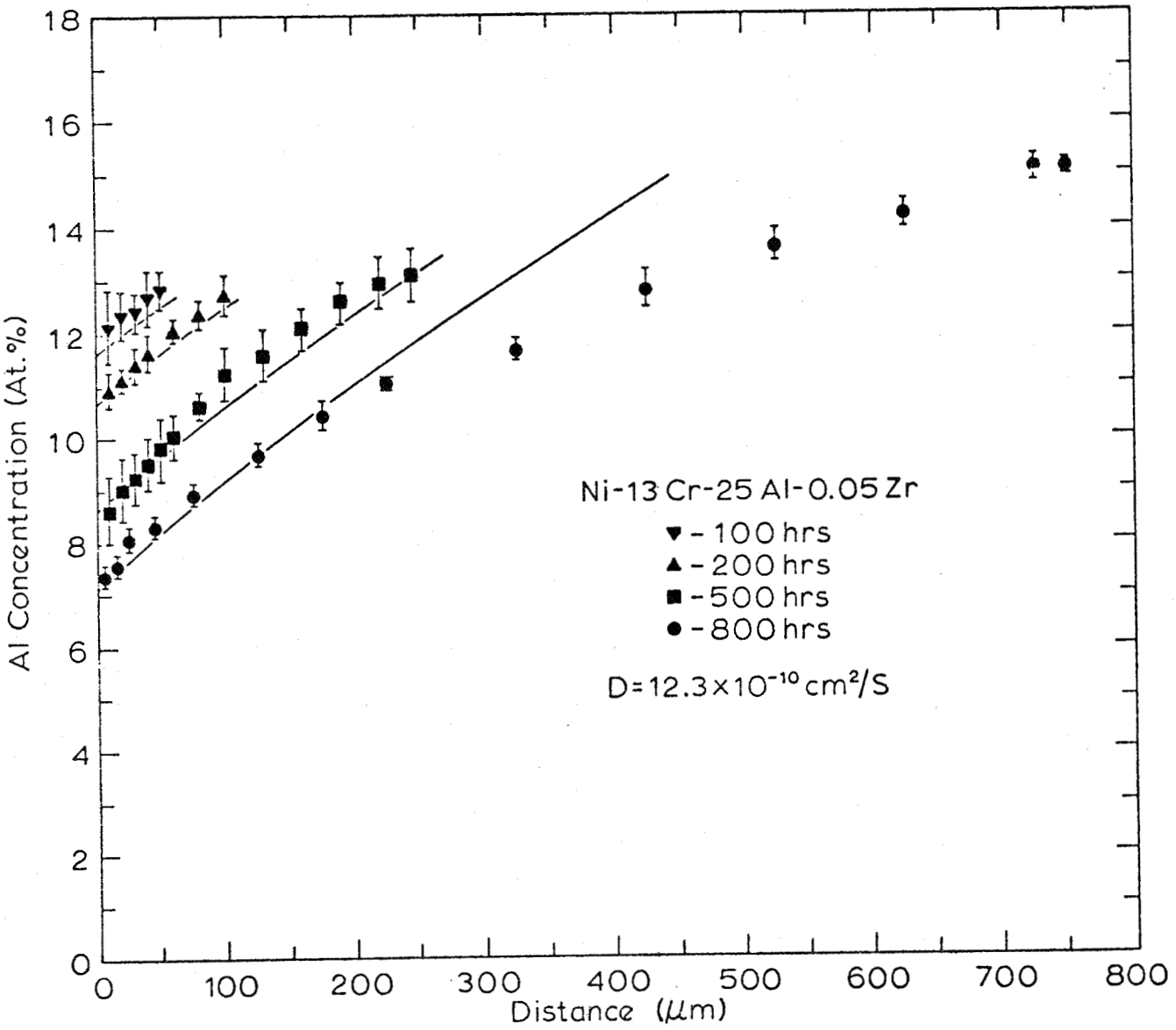

Figure 26. Predicted and measured Al concentration/distance profiles for the Ni-13Cr-25Al-0.05Zr alloy.

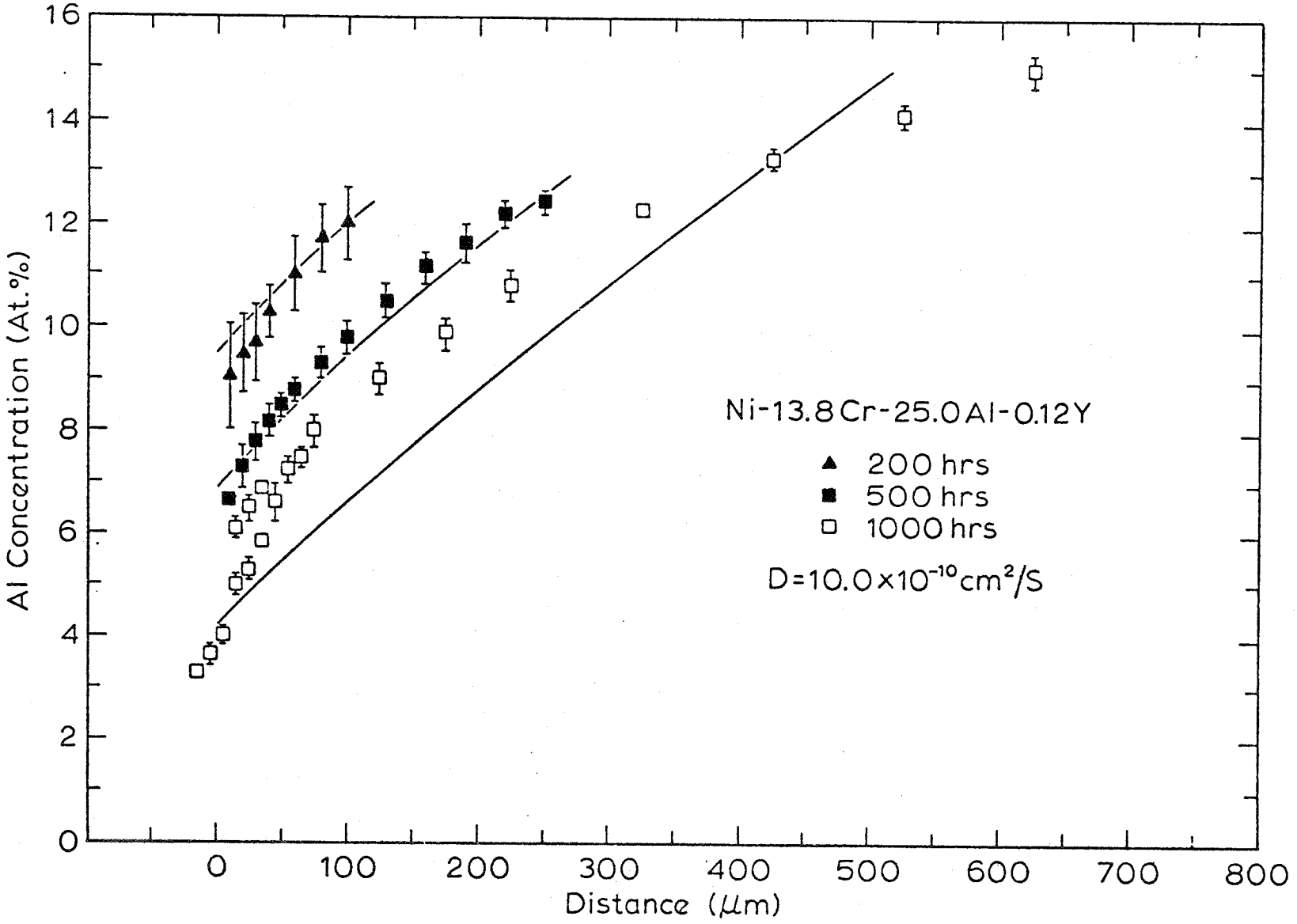

Figure 27. Predicted and measured Al concentration/distance profiles for the Ni-14Cr-25Al-0.12Y alloy.

may be the result of either a concentration dependence of the diffusion coefficient, the diffusion coefficient decreasing as the Al concentration decreases, or the effect of the Cr concentration profile on the Al diffusion.

The concentration/distance profiles and γ-layer widths were predicted with moderate success for the Ni-19Cr-24Al-0.04Zr alloy. This alloy exhibited the best oxide spalling characteristics of the four alloys studied and, consequently, has lost the least Al to the formation of Al_2O_3. Since the requisite flux for this alloy was relatively low, the concentration gradients measured and predicted were also low in comparison with the other alloys. The measured and predicted concentration/distance profiles for this alloy are shown in Figure 28. Small changes in the time dependence of the Al concentration at the oxide/metal interface, or at the $\gamma/\gamma+\beta$ interface, resulted in large changes in the γ-layer width. In addition, small differences in the initial alloy composition could also result in large differences between the predicted and observed behavior. An example of this is the high Al concentration measured in the γ layer of the 800-hour sample. The predicted concentration profile is much lower than that measured resulting in an overestimation of the γ-layer width.

The concentration/distance profiles and γ-layer width for the Ni-17Cr-28Al-0.18Zr alloy were also predicted with moderate success. The width of the γ layer was predicted fairly well through 500 hours but overestimated at 800 hours. The 500-hour and 800-hour samples were both from a different melt than the shorter-time samples and appear to have a slightly higher Al concentration at the $\gamma/\gamma+\beta$ interface than what would be expected based on the shorter-time concentration profiles. The measured and predicted concentration/distance profiles are shown in Figure 29.

The longer-time concentration profiles exhibit more curvature than the

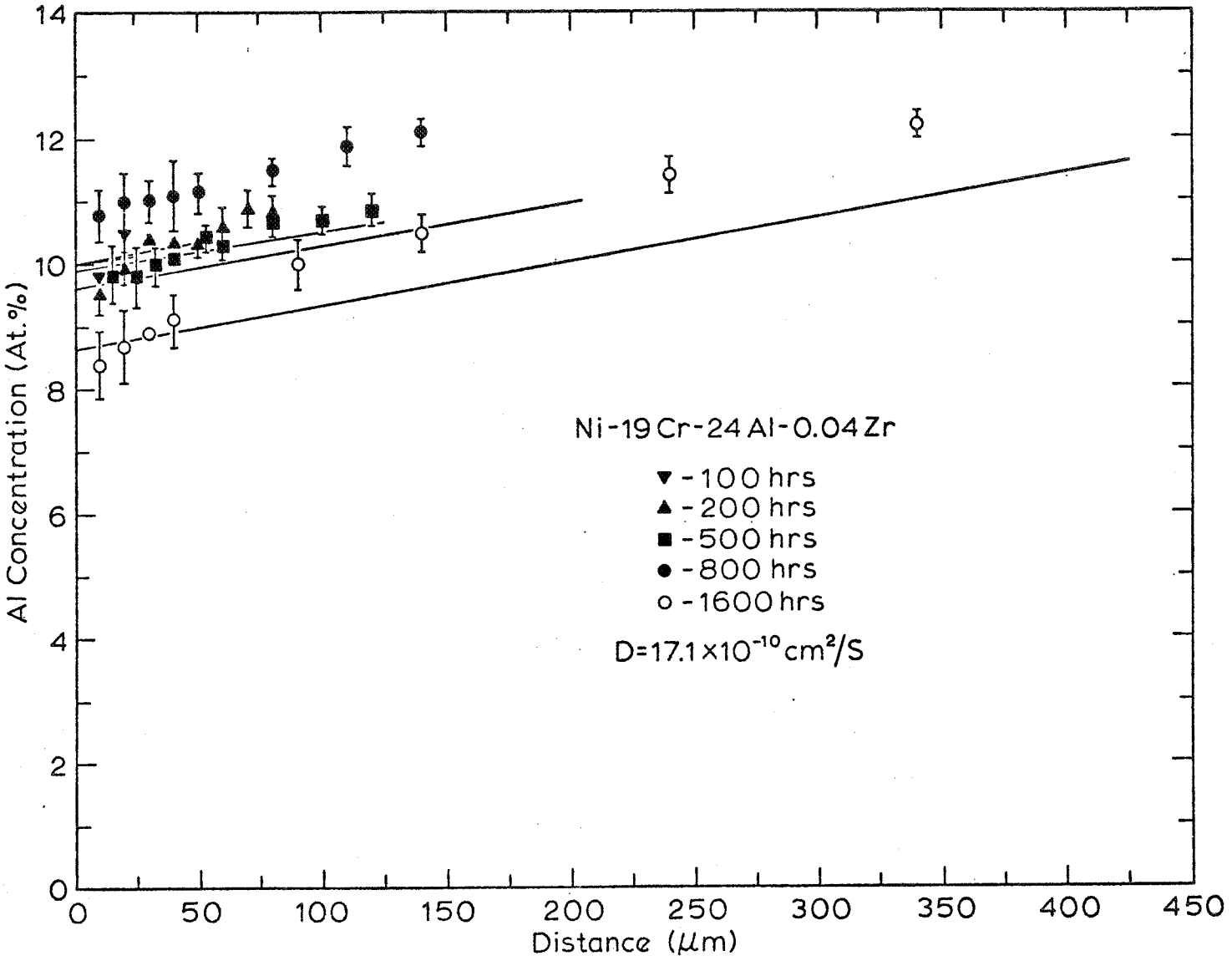

Figure 28. Predicted and measured Al concentration/distance profiles for the Ni-19Cr-24Al-0.04Zr alloy.

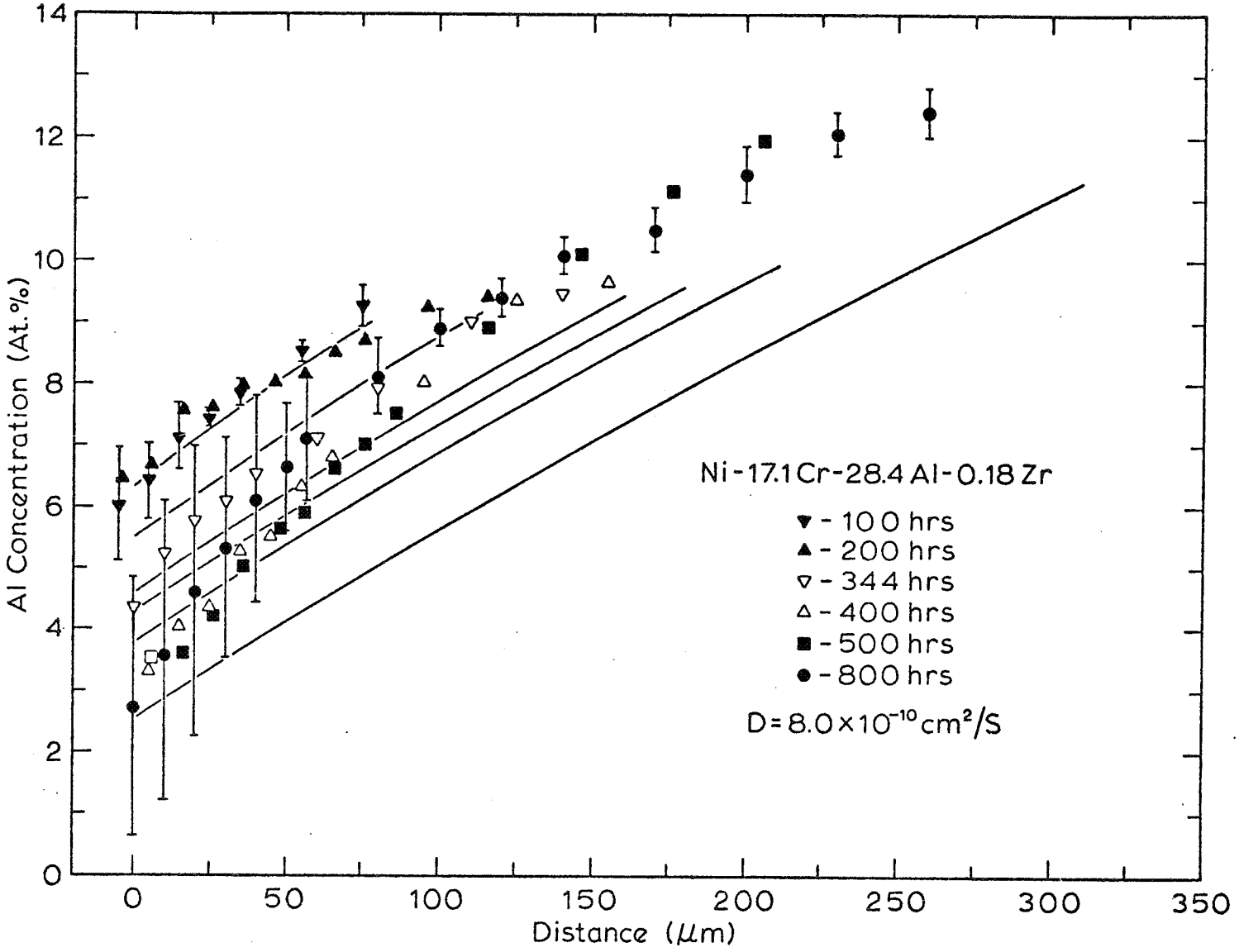

Figure 29. Predicted and measured Al concentration/distance profiles for the Ni-17Cr-28Al-0.18Zr alloy.

predicted concentration profiles. The additional curvature could be due to either concentration-dependent diffusion coefficients or the cross-term effect of the Cr concentration profiles. The curvature in the concentration gradients near the oxide/metal interface may also be due to the very irregular shape of this interface caused by the protrusion of the Al_2O_3 stringers into the γ layer. The Al diffusion in this region may not be in the single direction towards the oxide/metal interface but in three directions as Al also diffuses to the oxide stringers in a direction parallel to the sample surface. The increased sinks for the Al diffusion could effect lower Al concentrations and steeper Al gradients in the regions containing the oxide stringers.

The ability of the model to predict the width of the γ layer for each of the four cyclically oxidized alloys is shown in Figure 30. The Ni-14Cr-24Al-0.07Zr alloy after isothermal oxidation is shown also. Good agreement is evident for each of the alloys excluding the 800-hour Ni-13Cr-25Al-0.05Zr sample and the 1000-hour Ni-14Cr-25Al-0.12Y sample, both of which exhibited anomalous volume expansions.

The agreement between the predicted and experimentally determined weight of Al consumed is shown in Figure 31. The experimental values were determined graphically by the use of Figures 26 - 29. The anomalous volume expansions and the inability to determine accurately the oxide/metal surface recession at longer times prohibited the experimental determination of the weight of Al consumed beyond 500 hours. Because of the scatter in the concentration values in Figures 26 - 29, the accuracy of the experimental values is estimated to be $\pm$ 15%. Figure 31 shows that the Ni-19Cr-24Al-0.04Zr alloy exhibits the lowest loss of Al, consistent with the observation of good spalling characteristics attributed to an adherent Al_2O_3 oxide scale. The alloys Ni-13Cr-25Al-0.05Zr, Ni-14Cr-25Al-0.12Y, and Ni-17Cr-28Al-0.18Zr exhibit a high loss of Al indicating

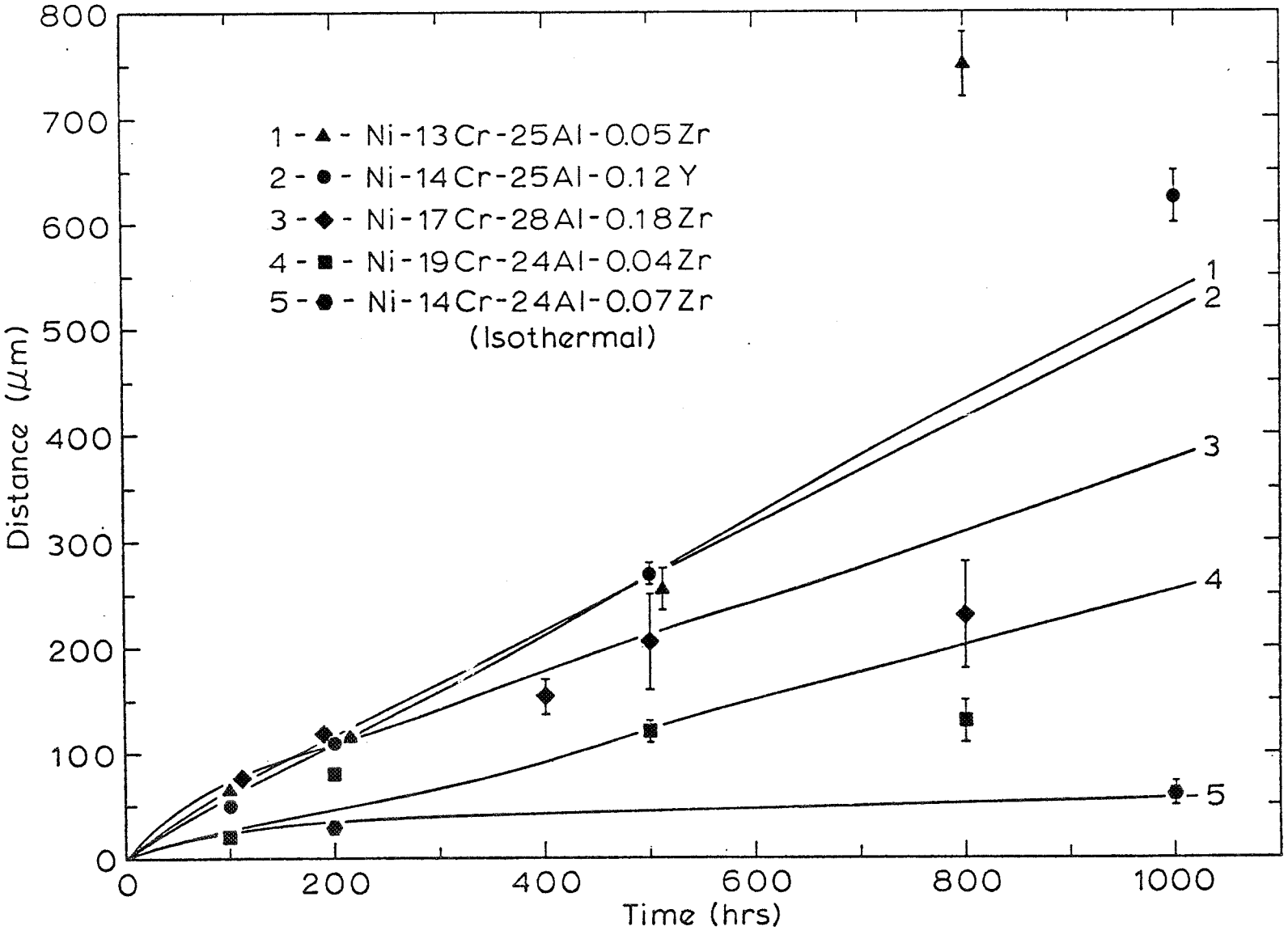

Figure 30. Predicted and measured width of the near-surface γ layer.

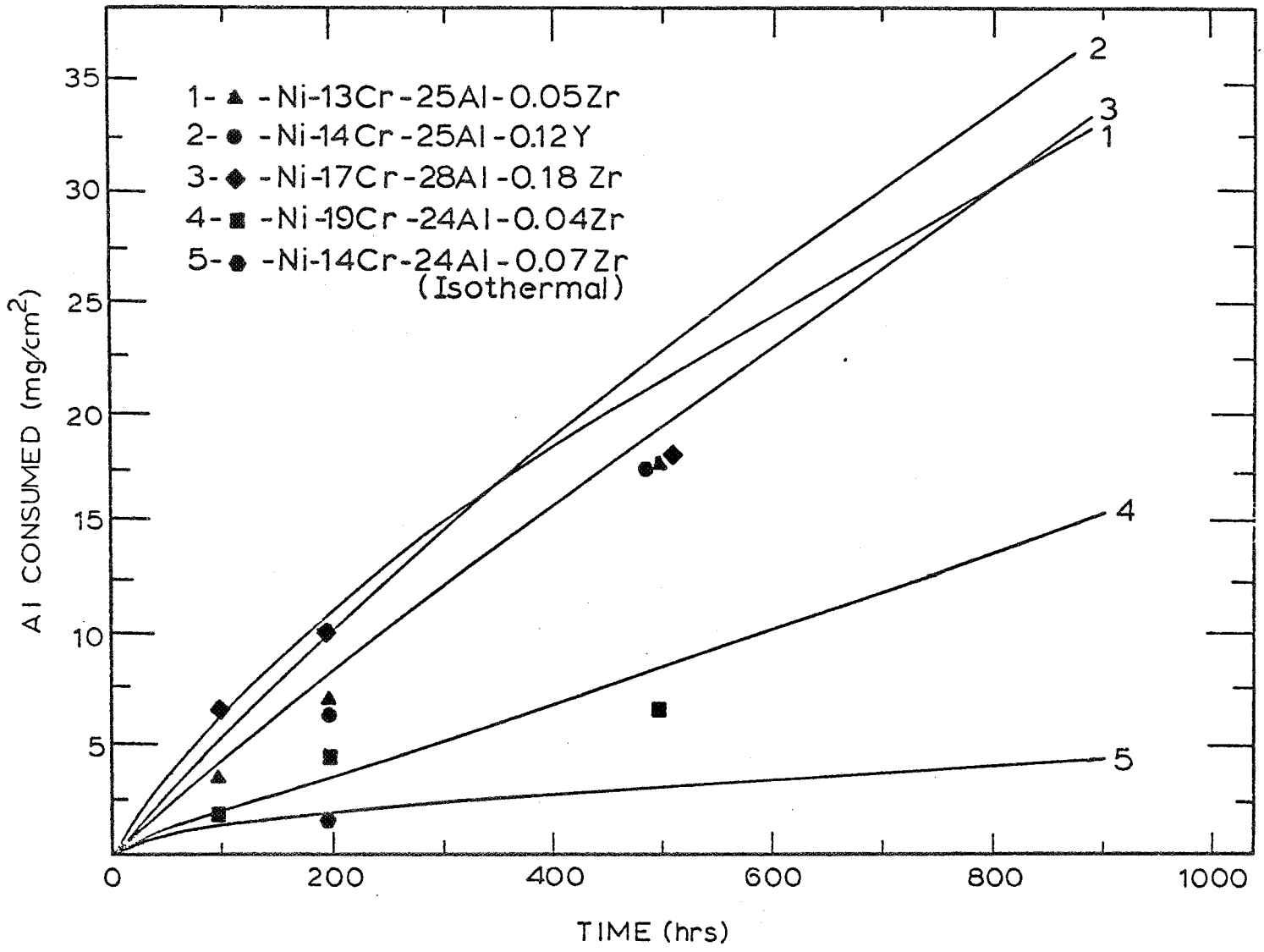

Figure 31. Predicted and measured weight of Al consumed.

poor scale adherence during cyclic oxidation. It is interesting to note that the alloy with the best scale adherence contained the lowest Zr content which was obtained by leaching Zr from a zirconia crucible during the melting process.

Breakaway Oxidation

Predicting the time to breakaway oxidation can be illustrated for the Ni-13Cr-25Al-0.05Zr alloy and the Ni-17Cr-28Al-0.18Zr alloy. Figure 31 indicates that both alloys have lost approximately the same amount of Al after 800 hours of cyclic oxidation. Hence, the requisite fluxes for both alloys were approximately equal. After several hundred oxidation cycles, the requisite flux approaches a constant value as the average oxide scale tends toward a constant thickness. The constant oxide-scale thickness is a consequence of scale growth being equal to scale spallation during each cycle. This behavior results in the linear portion of the paralinear weight change curves shown in Figure 4.

An approximately equal time-independent flux (J_2^{γ}) was input to the numerical model as a boundary condition at the oxide/γ-layer interface for the Ni-13Cr-25Al-0.05Zr and Ni-17Cr-24Al-0.18Zr alloys. The Al concentration at the oxide/γ-layer interface of the higher-Al-containing alloy was predicted to approach zero at a much shorter time. The input flux and the predicted interfacial Al concentration is shown in Figure 32. A parabolically decreasing flux and the resulting time-independent interfacial Al concentration for the isothermal oxidation of the Ni-14Cr-24Al-0.07Zr alloy is also shown. The experimental scatter in the Al concentration near the oxide/γ-layer interface in the Ni-17Cr-28Al-0.18Zr alloy suggests that breakaway oxidation over much of the sample surface could occur before 1000 oxidation cycles. The observation of limited breakaway oxidation after 500 hours, and the occurrence of greater areas undergoing breakaway oxidation after 800 hours (Figure 22), confirm the

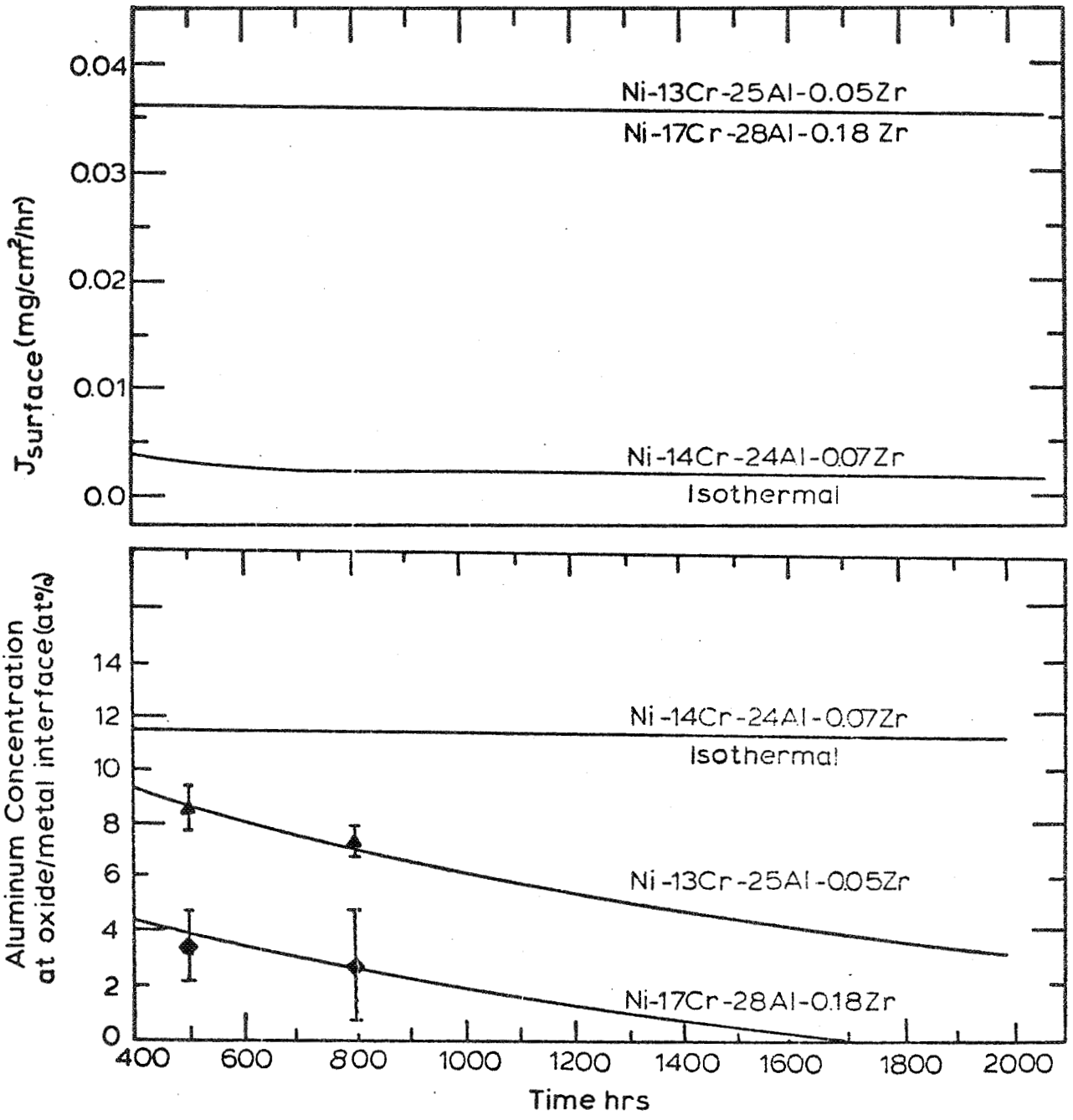

Figure 32. Input flux ($J_{surface}$) and the resulting Al concentration at the oxide/metal interface. The flux and interfacial Al concentration for isothermal oxidation is also shown.

model's prediction of the early failure of the high-Al alloy even though both alloys have lost approximately equal amounts of Al.

The time to breakaway oxidation is dependent on the alloy composition and the Al diffusivity. The Al content, as just shown, is not a sufficient parameter for ranking alloys according to their ability to resist breakaway oxidation. The alloy composition, specifically with regard to its position in the $\gamma + \beta$ region of the phase diagram, and the diffusion coefficient, relating the Al flux to the concentration gradient, must also be considered when predicting breakaway oxidation. The importance of the diffusivity and alloy position in the phase diagram can be seen in a comparison of the two alloys previously discussed, viz., the Ni-13Cr-25Al-0.05Zr and the Ni-17Cr-28Al-0.18Zr alloys. The diffusivity of the low-Al Ni-13Cr-25Al-0.05Zr alloy was measured as twice that of the high-Al Ni-17Cr-28Al-0.18Zr alloy. Therefore, the low-Al alloy could supply the same Al flux to the oxide/metal interface as the high-Al alloy but with only half the Al concentration gradient. The difference in the concentration gradients near the oxide/metal interface is obvious from a comparison of the predicted Al concentration profiles for each alloy at 800 hours, shown in Figure 33, where both alloys are supplying the same requisite flux (Figure 32).

Two important points regarding the bulk alloy composition and position in the phase diagram can be noted in Figure 33. First, the high-Al alloy has a large concentration drop at the $\gamma/\gamma + \beta$ interface, from the bulk concentration (C_o) to the maximum solubility of Al in the γ phase ($C_{\gamma\beta}$). The large concentration difference at the $\gamma/\gamma + \beta$ interface allows the high-Al (28 at.%Al) alloy to supply the same amount of Al to the oxide after 800 hours with less than three-fourths the depletion width of the low-Al (25 at.%Al) alloy (see Figures 1b and 1c). The second point to note is that the position of the high-Al alloy

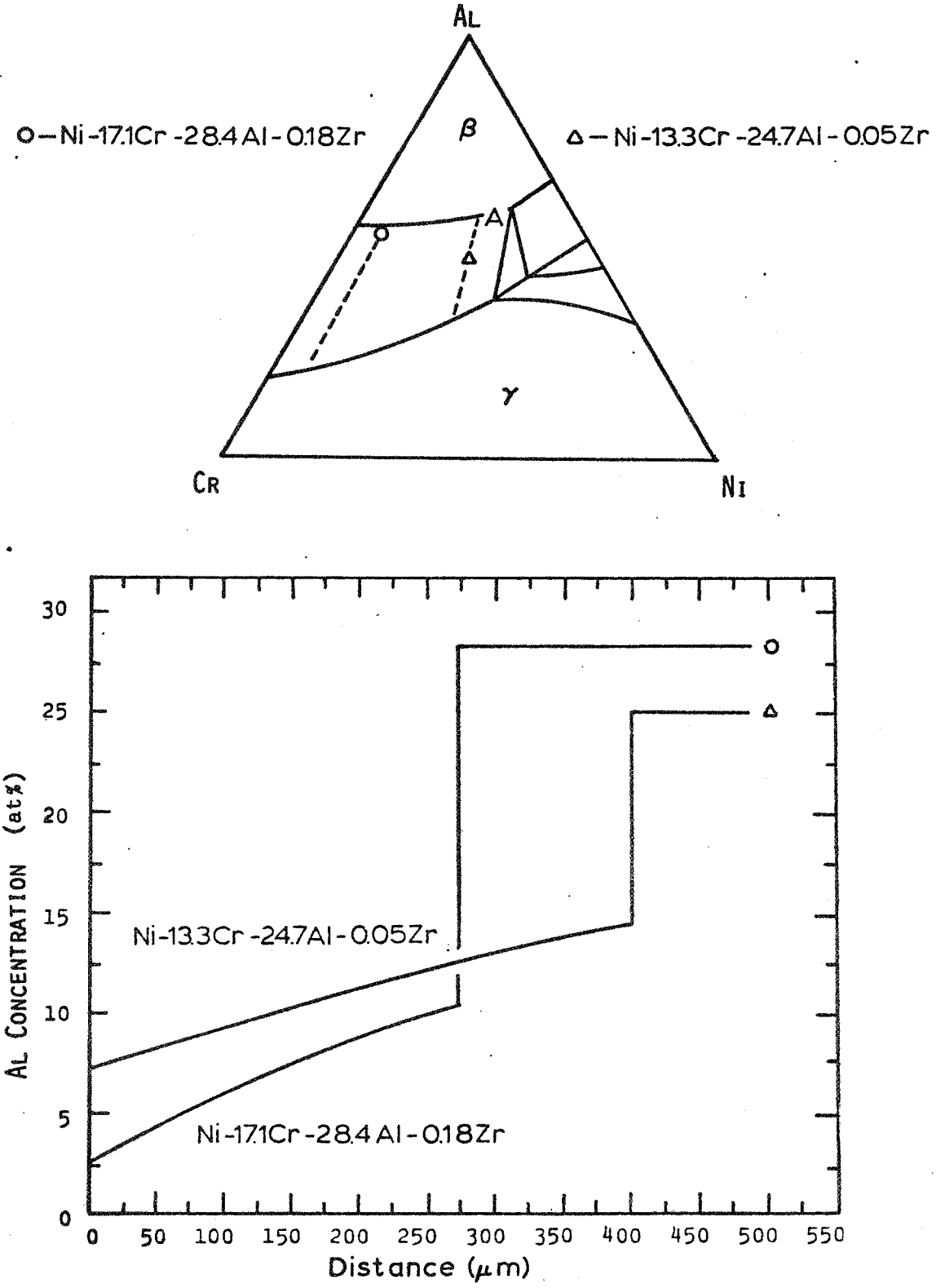

Figure 33. Predicted Al concentration profiles for 800 oxidation cycles of the Ni-17Cr-28Al-0.18Zr and the Ni-13Cr-25Al-0.05Zr alloys.

in the $\gamma + \beta$ field results in a low value of the maximum solubility of Al in the γ phase ($C_{\gamma\beta}$). Consequently, the Al concentration at the oxide/γ-layer interface is lower than that in the low-Al alloy. The same statement would be true even if the diffusivities, and therefore the concentration gradients, of both alloys were equal (see Figures 1b and 1d). An optimum $\gamma + \beta$ alloy composition may be selected to maximize the time before breakaway oxidation. The alloy would be chosen with the highest possible Al solubility in the γ phase ($C_{\gamma\beta}$) and the maximum Al content (C_0) effecting a low γ-layer growth rate. An alloy fitting this description is indicated as point A on the ternary phase diagram in Figure 33.

The assumptions made in the development of the numerical model can be examined to identify some of the possible sources of inaccuracy introduced to the model. The assumption of a planar interface at the $\gamma/\gamma + \beta$ boundary appears justified by the observation that the boundary remains planar on a macroscopic scale (Figures 9, 13, 15, 18, and 21) and by the fact that no concentration gradients were observed in the $\gamma + \beta$ region of any sample. The assumption of a constant molar volume seems reasonable based on the observation that considerable variation in the partial molar volume results in relatively small changes in the overall diffusion behavior (Appendix D). The assumption of exclusive formation of Al_2O_3 was accepted even though some oxides containing Ni and Cr were observed. Formation of Ni or Cr oxides would accelerate the motion of the oxide/metal interface but would be expected to have no greater effect on the overall diffusion behavior than the partial molar volume. The assumption that negligible diffusion occurs during heating and cooling of the sample appears justified considering the exponential relationship of the diffusion coefficient with temperature. The assumption of a planar interface at the oxide/γ-layer interface was only an approximation to the actual case, especially for the alloy

containing the highest Zr concentration (Ni-17Cr-28Al-0.18Zr). This assumption may have accounted for some of the inacuracy in the predicted concentration profiles especially near the oxide/γ-layer interface. The assumption of negligible cross-term effects (i.e., $D_{AlAl} >> D_{AlCr}$) has been adequately discussed in Appendix C. No conclusive justification for the concentration independence of the diffusion coefficients can be given. Any concentration dependence of the diffusion coefficient could easily account for most of the discrepancy between the predicted and measured concentration profiles. Based on the diffusion data for the similar CoCrAl systems (64), D_{AlAl} could easily vary with composition by an order of magnitude. A further assumption, not explicitly stated, was that the initial composition of each sample, oxidized at different times, was the same. Possible exceptions to this assumption were noted for alloys Ni-19Cr-24Al-0.04Zr and Ni-17Cr-28Al-0.18Zr.

Summary

The results of numerically modeling the Al transport during the cyclic oxidation of $\gamma + \beta$ NiCrAl alloys will be briefly reviewed. The results were:

1. The Al concentration/distance profiles resulting from cyclic oxidation of the $\gamma + \beta$ alloys were predicted fairly accurately through 500 hours. The anomalous volume distortions in two of the alloys, and differences in the 800-hour alloy compositions in two of the alloys, did not facilitate accurate predictions beyond 500 hours.
2. The γ-layer widths and the weight of Al consumed were likewise predicted with good accuracy through 500 hours but with less accuracy beyond 500 hours.
3. The experimental Al concentration/distance profiles showed more curvature than those predicted for several of the alloys. The increased curvature could be the result of cross-term effects or,

more likely, a concentration dependence of the Al diffusivity.

4. Breakaway oxidation was correctly predicted to occur in the alloy with the greatest Al content before an alloy with a lower Al content.

CONCLUSIONS

Several conclusions may be drawn from the present study of the Al transport during the cyclic oxidation of $\gamma + \beta$ NiCrAlZr(Y) alloys. The conclusions from the experimental results are:

1. Oxide spallation results in an accelerated loss of Al from the sample.
2. Repeated oxide spallation results in a decreasing Al concentration at the oxide/γ-layer interface.
3. The rate of Al decrease at the oxide/γ-layer interface is in proportion to the severity of the oxide spallation.
4. Breakaway oxidation occurs when the Al concentration at the oxide/γ-layer interface is approximately zero.
5. The γ-layer width thickens at an accelerated, non-parabolic rate.
6. The loss of Al from finite samples leads to diffusion path translation, changes in the composition of both phases in the $\gamma + \beta$ region, and a related decrease in the volume fraction of the β phase.

The conclusions from the numerical modeling study are:

1. The diffusional transport of Al in the γ-phase layer can be modeled with acceptable accuracy to predict the γ-layer thickness, the concentration/distance profiles, and the weight of Al consumed.
2. Breakaway oxidation can be predicted from the bulk alloy composition, approximate diffusion coefficients, and the requisite flux.

APPENDIX A

TECHNIQUE OF QUANTITATIVE ELECTRON MICROSCOPY

The Ni, Cr, and Al concentrations in each of the NiCrAlZr(Y) alloys were determined by use of a scanning electron microscope (SEM), an energy-dispersive x-ray spectrometer (EDS), and a numerical correction scheme. The SEM was a JEOL JSM 35C operated at an accelerating potential of 20 KeV and a beam current of approximately 1×10^{-9} amperes. The instrument was equipped with a beam current stabilizer. The x-ray source size, or approximate volume producing x-rays (65) was calculated to be 1.0 - 1.5 μm. The EDS system consisted of an EDAX Si(Li) counting system coupled to a 711 series multichannel analyzer. The EDS system was connected to a Texas Instrument 733 ASR high-speed data terminal interfaced to a Data General NOVA2 mini-computer. The mini-computer contained both peak stripping routines and various correctional schemes.

The correctional scheme used in this study accounts for the three main sources of interference between elements in an alloy. The three interference effects accounted for are:

1. The variation in the generation of x-rays due to changes in the matrix composition and the incident electron energy. This effect is commonly referred to as the "atomic number effect" (Z) because of its dependence on the average atomic number of the matrix.
2. The absorption (A) of the x-rays characteristic of one element by the other elements in the matrix. The degree of absorption is dependent on the depth distribution of the generated x-rays and on the absorption coefficients of each of the other elements in the matrix.
3. The secondary fluorescence (F) of x-rays generated by one element when it absorbs the primary x-rays generated by a second element.

The equations to account for the above interference effects are commonly

referred to as ZAF corrections. The correctional scheme used in this study (66) was a modified version of the original computer program, designated FRAME, incorporating the ZAF corrections. Input to the program consisted of the x-ray intensity ratios (described later) for each element in the matrix, the characteristic x-ray line being used (K_α in the present study), the operating voltage, and the angles between the incident electron beam, sample surface, and the EDS collector.

The typical sequence of steps to determine the concentration at a single point in the matrix is given below. The SEM was operated in the spot mode for a set time, usually between four and five minutes. The continuous spectrum with the characteristic peaks for Ni, Cr, and Al was collected and stored by the EDS and multichannel analyzer. The continuous spectrum from the multichannel analyzer was entered into the mini-computer, and the K_α peaks of Ni, Cr, and Al were stripped from the continuous spectrum by numerical routines stored in the mini-computer. The stripped K_α peak intensities were divided by their respective pure element (Ni, Cr, and Al) intensities, measured under the same operating conditions. The resulting quotients, commonly referred to as the intensity, or k, ratios for each element were input back into the mini-computer along with the operating voltage of the SEM, the characteristic x-ray line used to determine the intensity ratios, and the appropriate angles as previously described. The computer program applied the ZAF corrections to the intensity ratios and listed the weight fraction for each element. In almost all cases, the sum of the weight fractions of Ni, Cr, and Al was in the range 0.95 - 1.00, most often between 0.98 - 1.00.

Nine NiCrAl alloys of unknown composition were analyzed by the above procedure to determine the accuracy of the ZAF correctional routines. Seven γ-phase alloys and two β-phase alloys were fabricated and homogenized at 1200°C

for a week. The samples were sectioned and a portion of each sample was analyzed by atomic absorption at the NASA Lewis Research Center. The remaining portion of each alloy was analyzed following the procedure as described above. The compositions as determined by atomic absorption are compared with the compositions determined with the ZAF correction routines in Table A-1.† As shown, the relative errors are the greatest for the Al concentration; but the maximum relative error only amounts to less than 0.5 wt.% difference in the Al concentration. Therefore, the accuracy of the Al concentration as determined in this study, at the worst, could be set at approximately ± 10% relative, which amounts to an absolute error of less than 0.5 wt.%Al (∿ 1.0 at.%Al).

†The position of the nine standards in relation to the measured phase boundaries of the NiCrAl system at 1200°C are shown in the phase diagram of Figure B-1 in Appendix B.

TABLE A-1

COMPARISON OF THE NI, Cr, AND Al CONCENTRATIONS AS MEASURED BY ATOMIC ABSORPTION AND TECHNIQUE USED IN THIS STUDY*

Atomic Absorption			ZAF Correction Routines			% Relative Error**			ΔC		
Ni	Cr	Al	Ni	Cr	Al	Ni	Cr	Al	Ni	Cr	Al
γ phase											
62.57	34.34	3.09	64.56	34.59	3.16	3.2	0.7	2.3	1.99	0.25	0.07
66.54	29.50	3.96	67.89	29.20	4.39	2.0	1.0	10.8	1.35	0.30	0.43
70.28	24.74	4.98	70.16	24.67	4.92	0.2	0.3	1.2	0.12	0.07	0.06
76.41	17.95	5.64	75.63	17.62	5.91	1.0	1.8	4.8	0.78	0.33	0.27
73.40	24.26	2.34	76.20	24.50	2.35	3.8	1.0	0.4	2.80	0.24	0.01
79.83	17.88	2.29	80.81	17.54	2.22	1.2	1.9	3.0	0.98	0.34	0.07
90.34	7.10	2.56	89.30	6.67	2.33	1.2	6.0	9.0	1.04	0.43	0.23
β phase											
66.77	14.84	18.39	65.92	15.40	18.58	1.3	3.8	1.0	0.85	0.56	0.19
73.21	8.00	18.79	73.49	7.85	18.53	0.4	1.9	1.4	0.28	0.15	0.26

* all concentrations in wt.%

** % relative error = (At. Abs. - ZAF)/ At. Abs. * 100

APPENDIX B

EFFECTIVE NiCrAl PHASE DIAGRAM AT 1200°C

An effective phase diagram for the NiCrAl system at 1200°C was determined and utilized throughout this study. Quantitative electron microscopy (Appendix A) in the $\gamma + \beta$ region of various alloys yielded the concentration of the γ phase at the $\gamma/\gamma + \beta$ phase boundary and the concentration of the β phase at the $\gamma/\gamma + \beta$ phase boundary. The concentration of the γ phase at the $\gamma/\gamma + \beta$ phase boundary demonstrated a good fit to a single line when plotted on the NiCrAl phase diagram, whereas the concentration of the β phase at the $\beta/\gamma + \beta$ phase boundary showed more scatter about a single line. The experimentally determined data points and the effective phase boundaries, indicated as solid lines, are shown in Figure B-1. The concentrations and heat treatments are given in Table B-1.

Two points of particular interest in this study can be noted by reference to the effective $\gamma/\gamma + \beta$ phase boundary. First, the boundary shows no particular dependence on the Zr or Y content of the alloys. In addition, the Ni-13.9Cr-25.1Al alloy, containing no Zr, shows the same approximate concentration at the phase boundary as the Ni-13Cr-25Al-0.05Zr alloy. Hence, there is no significant dependence of the $\gamma/\gamma + \beta$ phase boundary on the Zr or Y content of the examined alloys. Second, the concentrations of the γ phase at the $\gamma/\gamma + \beta$ phase boundary show the same fit to a single line regardless of whether the alloy was isothermally annealed as part of a diffusion couple, isothermally oxidized, or cyclically oxidized (where diffusion path translation caused a change in the concentration of the γ and β phases with time). Therefore, it appears that the γ and β phases were at thermodynamic equilibrium during the elevated temperature period of cyclic oxidation.

The $\gamma/\gamma + \beta$ and the $\beta/\gamma + \beta$ phase boundaries determined in this study are at lower Al concentrations than the published NiCrAl phase diagram for 1150°C.

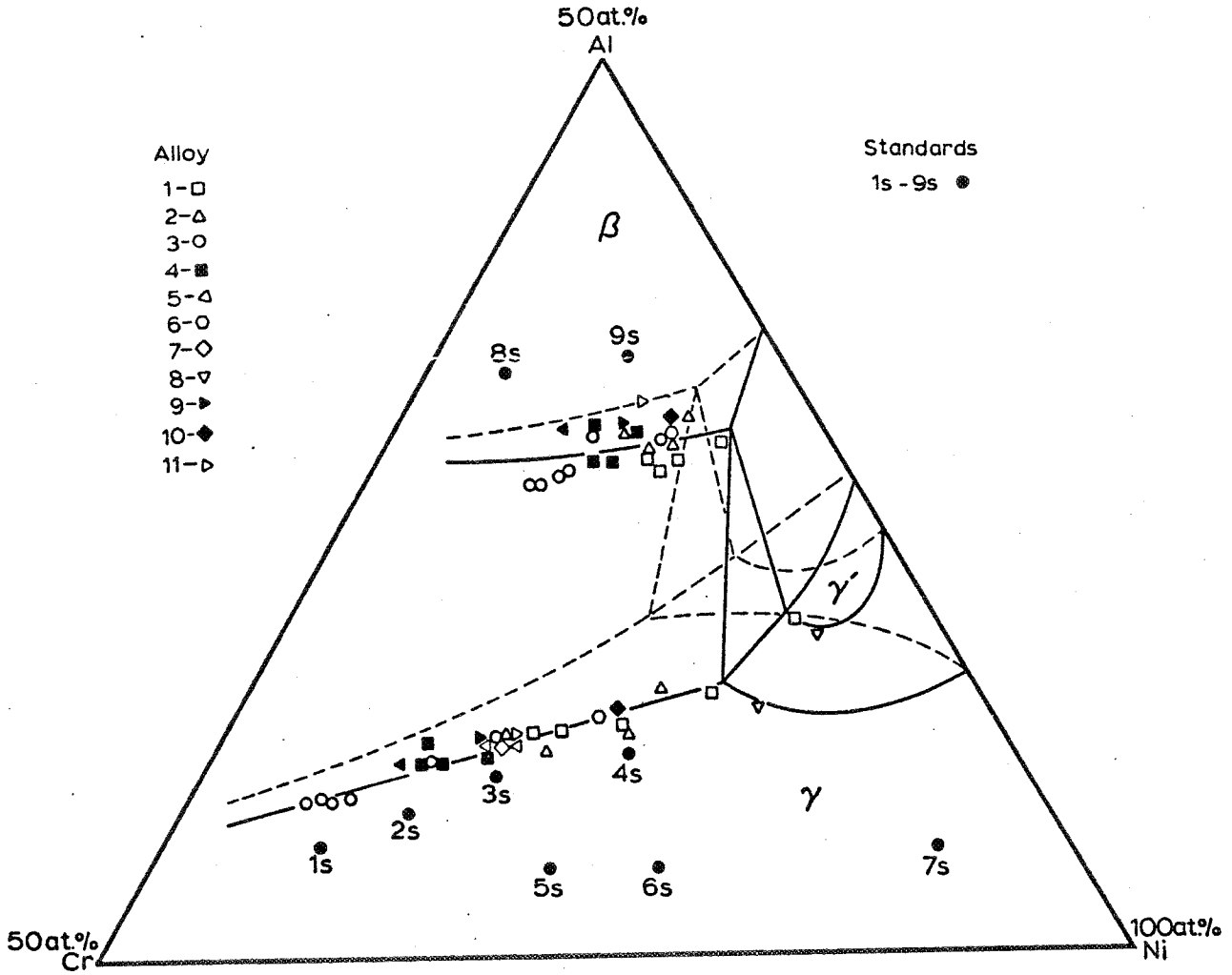

Figure B-1 Effective phase boundaries for the NiCrAl system at 1200°C determined in this study. Dashed lines indicate 1150°C phase boundaries from Reference 67.

TABLE B-1

ALLOY COMPOSITION AT THE $\gamma/\gamma+\beta$ AND $\beta/\gamma+\beta$ BOUNDARIES

Alloy #	Alloy Composition (at. %)			Treatment
	Cr	Al	Zr(Y)	
1	13.3	24.7	0.05	cyclically oxidized 100, 200 500, & 800 hours.
2	13.8	25.0	0.12Y	cyclically oxidized 100, 200, 500, 1000 hours.
3	17.1	28.4	0.18	cyclically oxidized 100, 200, 344, 400, 500, 800 hours.
4	19.0	23.6	0.04	cyclically oxidized 100, 200, 500, 800, 1600 hours.
5	14.4	23.7	0.07	isothermally oxidized 200 and 1000 hours.
6	14.4	23.7	0.07	cyclically oxidized 800 hours.
7	13.9	25.7	0.0	isothermally oxidized 200 hours.
8	9.7	17.2	0.17	cyclically oxidized 200 hours.
9	14.4	23.7	0.07	isothermal anneal in excess of 100 hours (diffusion couple).
10	16.0	17.5	0.11	isothermal anneal in excess of 100 hours (diffusion couple).
11	20.8	16.5	0.02	isothermal anneal in excess of 100 hours (diffusion couple).
Standards				isothermal anneal for 1 week
1s	35.9	6.2	—	
2s	30.7	7.9	—	
3s	25.6	9.9	—	
4s	18.6	11.3	—	
5s	25.9	4.8	—	

TABLE B-1 (cont.)

Alloy #	Alloy Composition (at. %)		
	Cr	Al	Zr(Y)
6s	19.2	4.7	—
7s	7.7	5.4	—
8s	13.6	32.4	—
9s	7.3	33.2	—

The 1150°C phase diagram reported by Taylor and Floyd (67) is shown as dashed lines in Figure B-1. The differences between the measured $\gamma/\gamma + \beta$ boundary and that reported are greater than the maximum ± 1.0 at.%Al accuracy of the concentration-measuring technique (Appendix A). Taylor and Floyd also indicated that raising the temperature results in an increase in the Al concentration of the $\gamma/\gamma + \beta$ phase boundary. Hence, the difference in the $\gamma/\gamma + \beta$ phase boundaries cannot be explained by reference to the 50°C temperature differential. A more accurate reassessment is necessary to clarify the discrepancy between the observed and reported phase boundaries.

APPENDIX C

DIFFUSION COEFFICIENTS

Introduction

Diffusion phenomena in ternary alloys may be significantly different from those observed in binary alloys. In both alloys, atoms diffuse down their own chemical potential gradients, but whereas in the binary case the chemical potential gradient of a component increases with increasing concentration of that component, no such generalization can be stated for the ternary case. As a result, "uphill" diffusion, component diffusion up its own concentration gradient, or diffusion in a two-phase region is possible in ternary alloys.

In a ternary system, four diffusion coefficients are required to describe the interdiffusion of atoms. The coefficients are of two types (64): direct diffusion coefficients which relate the flux of a component to its own concentration gradient, and cross-term diffusion coefficients which relate the flux of a component to the concentration gradients of the other components in the system. It can easily be shown that two components are sufficient to analytically describe ternary diffusion (63). The appropriate diffusion equations relating concentrations, positions, and time for non-steady-state diffusion in a single phase is Fick's second law. The appropriate ternary form is:

$$\frac{dC_1}{dt} = \frac{d}{dx}\left(D_{11}\frac{dC_1}{dx}\right) + \frac{d}{dx}\left(D_{12}\frac{dC_2}{dx}\right) \qquad \text{(C-1a)}$$

$$\frac{dC_2}{dt} = \frac{d}{dx}\left(D_{21}\frac{dC_1}{dx}\right) + \frac{d}{dx}\left(D_{22}\frac{dC_2}{dx}\right) \qquad \text{(C-2a)}$$

where: C_i = concentration of either component 1 or component 2 (i = 1,2),

t = time,

D_{11}, D_{22} = direct diffusion coefficients,

D_{12}, D_{21} = indirect diffusion coefficients,

x = distance parameter.

The terms containing D_{12} and D_{21} are commonly referred to as the cross terms. Fick's first law relates the flux of either component to the concentration gradients of both components. The appropriate form for Fick's first law is:

$$J_1 = -D_{11} \frac{dC_1}{dx} - D_{12} \frac{dC_2}{dx} \qquad \text{(C-2a)}$$

$$J_2 = -D_{21} \frac{dC_1}{dx} - D_{22} \frac{dC_2}{dx} \qquad \text{(C-2b)}$$

where J_1 and J_2 are the fluxes of component 1 and component 2, respectively. The other symbols are as described previously. For the case of a moving boundary between a single-phase (γ) and a two-phase ($\gamma + \beta$) region, the appropriate mass balance at the interface is:

$$(C_1^0 - C_1^\gamma) \frac{d\xi}{dt} = -J_{1,\xi}^\gamma \quad \text{for component 1} \qquad \text{(C-3a)}$$

$$(C_2^0 - C_2^\gamma) \frac{d\xi}{dt} = -J_{2,\xi}^\gamma \quad \text{for component 2} \qquad \text{(C-3b)}$$

where: $\frac{d\xi}{dt}$ = velocity of the $\gamma/\gamma + \beta$ interface,

$J_{i,\xi}^\gamma$ = flux of component i evaluated at the interface as approached from the γ phase (i = 1,2),

C_i^0 = concentration of component i in the $\gamma + \beta$ region (i = 1,2),

C_i^γ = concentration of component i at the interface as approached from the γ phase (i = 1,2).

A schematic of the concentration/distance profiles for the case where a $\gamma + \beta$

NiCrAl alloy is diffusion bonded to a γ-phase NiCr alloy is shown in Figure C1.

The effect of the cross terms on the diffusion behavior of NiCrAl alloys can be estimated by a judicious selection of $\gamma/\gamma+\beta$ diffusion couples. It was the intent of this particular investigation to estimate the effect of the cross terms on the diffusion of Al and to investigate the possibility of using a single diffusion coefficient to describe the Al transport. Towards this purpose extensive use was made of diffusion couple measurements on similar $\gamma+\beta$ NiCrAl alloys by S. R. Levine of the Lewis Research Center (9).

Experimental Procedure

Various $\gamma/\gamma+\beta$ diffusion couples were utilized to investigate the diffusion behavior of three $\gamma+\beta$ NiCrAl alloys. The composition of the three $\gamma+\beta$ alloys corresponded to the basic alloy compositions (minus Zr and Y) studied in the cyclic oxidation portion of this investigation. The $\gamma+\beta$ alloys were cut, polished to 600 grit with SiC paper, and placed adjacent to various NiCr γ-phase alloys in a molybdenum (Mo) canister (Figure C2). The canister and contents were annealed at 1200°C in an inert atmosphere for various times. The lower thermal expansion of the Mo canister caused a compressive stress to be placed on the couples resulting in diffusion bonding at the elevated temperature. The composition of the $\gamma+\beta$ NiCrAl alloys and the γ-phase NiCr alloys are listed in Table C1.†

Diffusion of Al from the Al-rich $\gamma+\beta$ alloy into the NiCr alloy resulted in β dissolution and the consequent growth of a γ-phase layer into the original

†The various $\gamma/\gamma+\beta$ couples will hereafter be referred to by the short designation given in Table C1. In this designation of i/j, i will refer to the $\gamma+\beta$ alloy or "source" (high Al), and j will refer to the γ-phase alloy or "sink" (low Al).

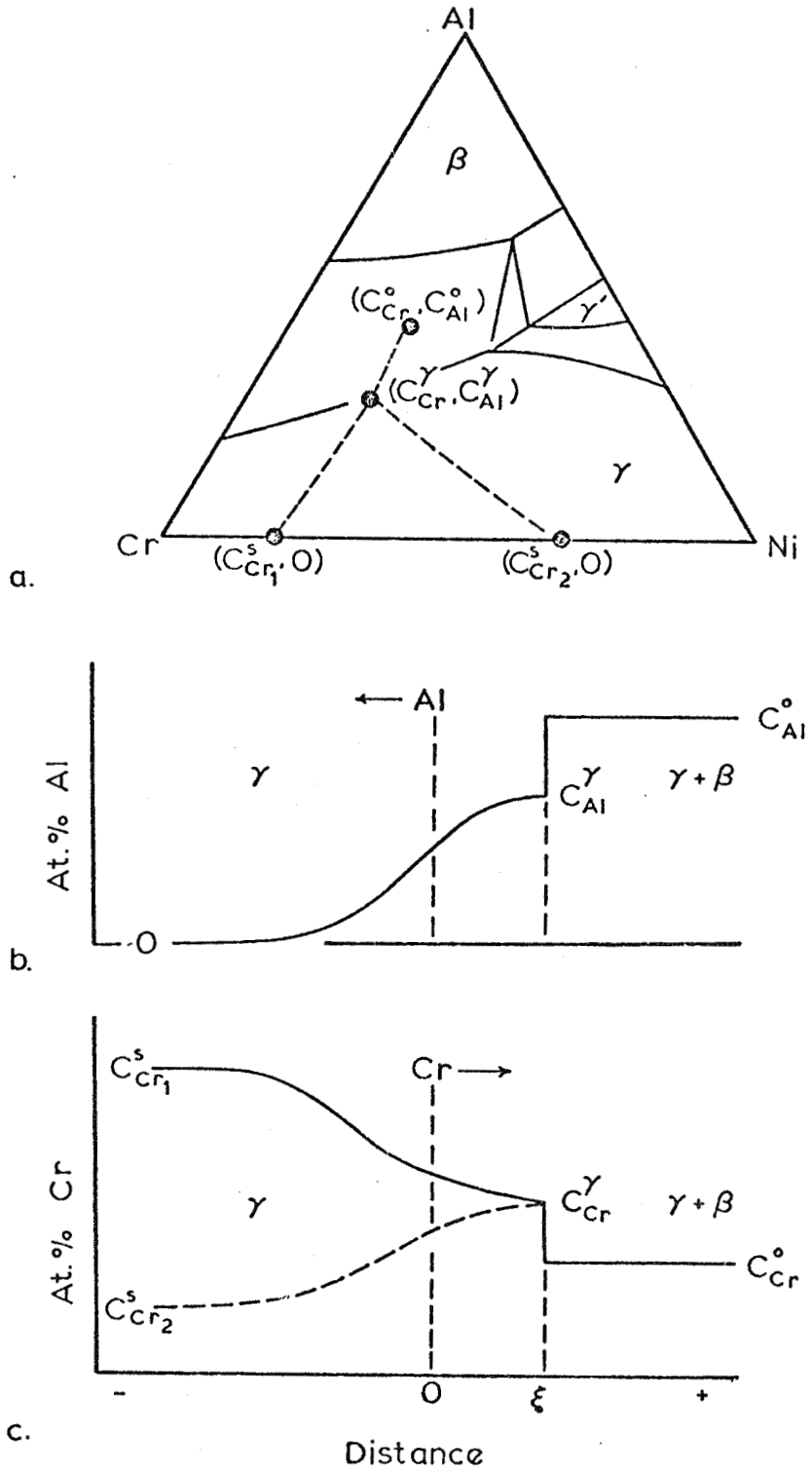

Figure C-1 γ/γ+β Diffusion Couples
a. NiCrAl source alloy and two possible NiCr sink compositions, b. schematic Al concentration profile and, c. Cr concentration profile after annealing the diffusion couple.

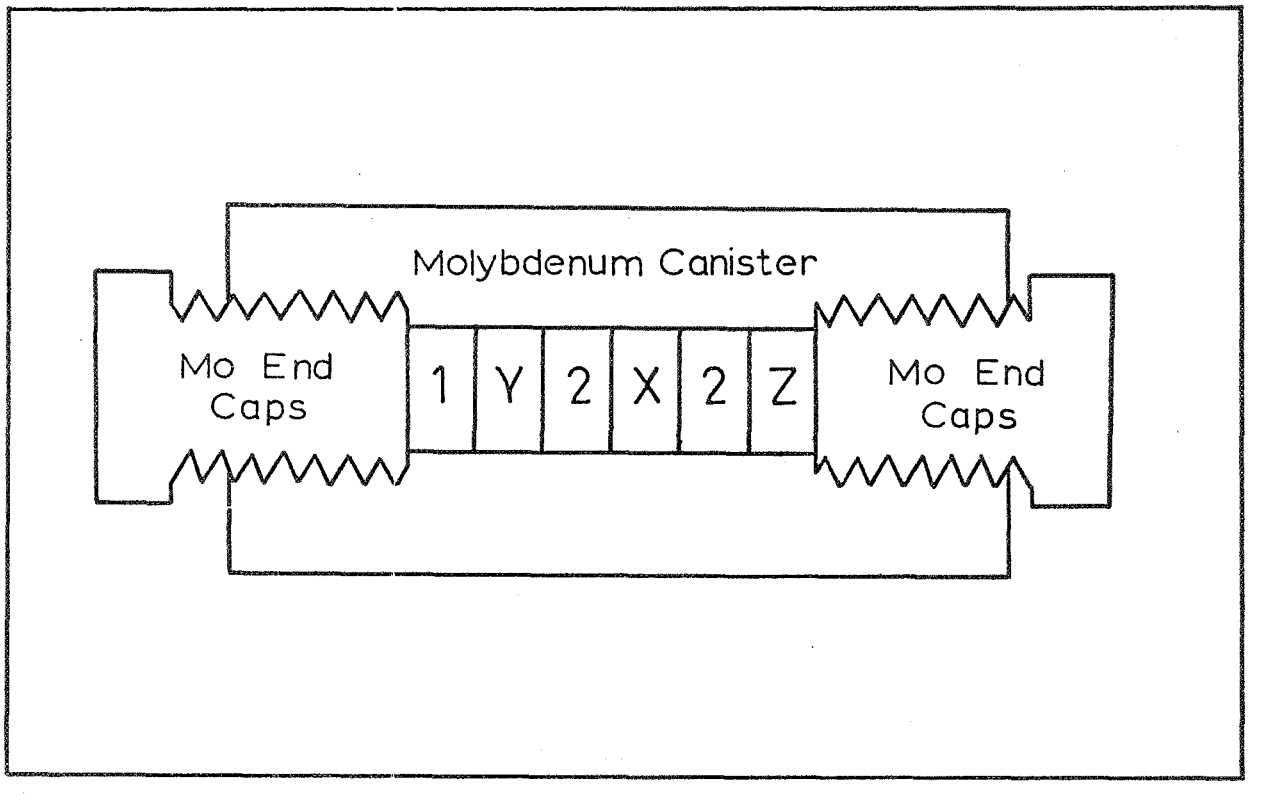

Figure C-2 Cross sectional diagram of Mo canister and diffusion couples used in determining the approximate diffusion coefficients.

TABLE C-1

ALLOY COMPOSITIONS USED IN $\gamma/\gamma+\beta$ DIFFUSION COUPLES

Alloy Designation	Ni	Cr	Al	Zr
Source				
1	61.9	14.4	23.7	—
2	57.9	19.0	23.6	—
3	54.6	17.1	28.2	—
4*	63.3	12.7	24.0	—
4-Zr*	63.1	12.7	24.0	0.16
Sink				
W	89.0	11.0	—	—
X	80.0	20.0	—	—
Y	70.0	30.0	—	—
Z	60.0	40.0	—	—

* Reference 69.

two-phase alloy. A typical microstructure after a diffusion anneal is shown in Figure C-3. The diffusion couples were sectioned perpendicular to the original $\gamma/\gamma+\beta$ interface so that the γ-layer width could be measured. The couples were polished, etched, and the γ-layer width was measured by optical microscopy. The width was observed to increase at a parabolic rate in agreement with the previous study (9). The time dependence of the γ-layer width for both studies is shown in Figure C-4. The Al and Cr concentrations were measured in the γ phase at the $\gamma/\gamma+\beta$ interface (C^{γ}_{Al}, C^{γ}_{Cr} in Figure C-1) for the 1/Y and 2/Y couples by the technique described in Appendix A. The limited data indicate that the measured concentrations (C^{γ}_{Cr}, C^{γ}_{Al}) are the concentrations at the end of tie lines passing through the $\gamma+\beta$ alloy compositions (see dotted line in Figure C-1a). This behavior will be referred to as tie-line diffusion. Some Al_2O_3 precipitates appeared at the $\gamma/\gamma+\beta$ interface, probably as a result of oxygen remaining in the sealed Mo canister. The appearance of the precipitate seemed to have little effect on the diffusion kinetics.

Experimental Results and Discussion

The approximately equal growth rates of the γ-phase layer in couples 2/W, 2/X, 2/Y, and 2/Z (2/_ couples) indicate the Cr concentration gradient had little effect on the Al diffusion; i.e., D_{AlCr} is much less than D_{AlAl}. This can be understood by reference to Eqs. C-2a and C-3a where component 1 represents Al and component 2 represents Cr. In Eq. C-3a, the $\gamma/\gamma+\beta$ interface velocity ($\frac{d\xi}{dt}$) is approximately the same for the 2/_ couples. C^{0}_{Al} and C^{γ}_{Al} can be assumed constant for the same source alloy (Figure C-1a). Therefore, from Eq. C-3a, the Al flux $J^{\gamma}_{Al,\xi}$ must be approximately equal for each of the 2/_ couples. The Al concentration gradient (dC_{Al}/dx) can also be assumed to be essentially constant since the Al concentration at the $\gamma/\gamma+\beta$ interface

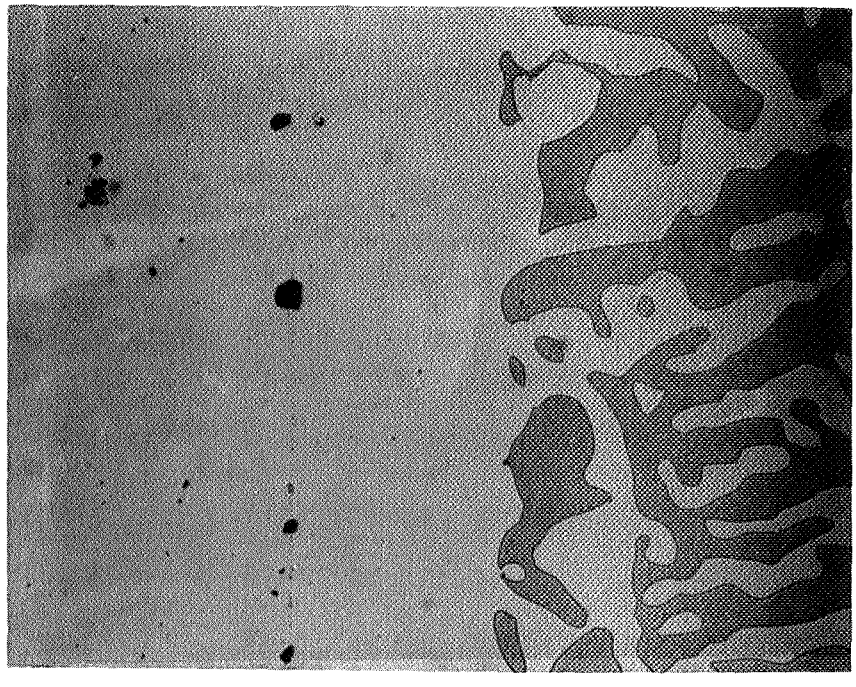

Figure C-3 Diffusion couple 2/X after 132 hour anneal at 1200°C. The original $\gamma/\gamma+\beta$ interface position runs through the dark, colinear oxide precipitates. (150x)

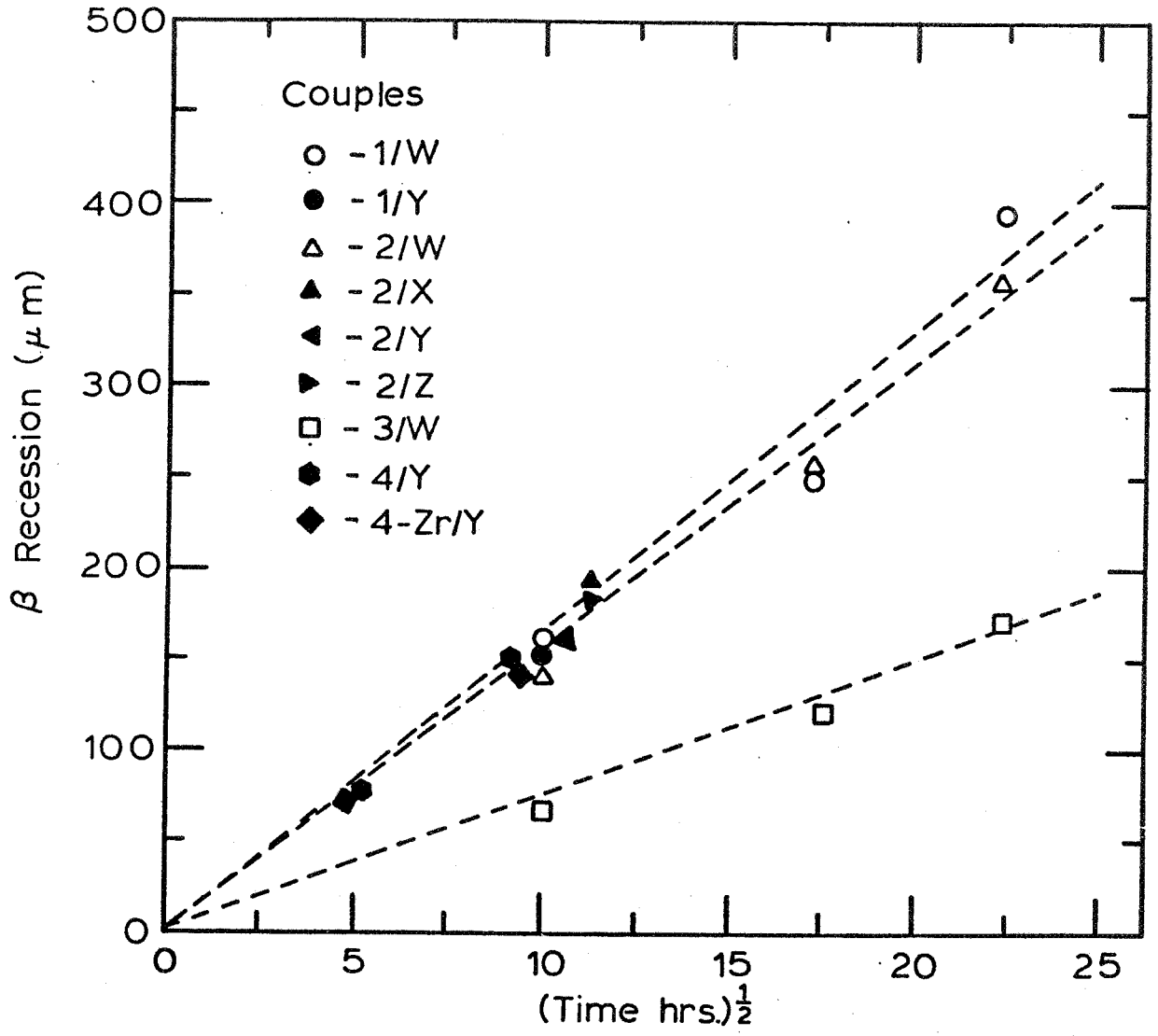

Figure C-4 β recession for the γ+β source alloys with various γ sink alloys. Dashed lines indicate k values reported for couples 1/W, 2/W, and 3/W in Reference 9 . Open symbols taken from Reference 9 .

"Page missing from available version"

"Page missing from available version"

Consideration of couples 2/X and 2/Z by similar reasoning implies the cross terms to be either dominant or significant with respect to the diffusive flux of Cr. The data in Table C-2 show that at a low Al concentration, D_{CrAl} and D_{CrCr} are similar in magnitude.

Small additions of Zr have only a slight effect on the growth rate of the γ layer (69). Figure C-4 illustrates the slightly larger γ-layer growth rate of couple 4/Y over the couple 4-Zr/Y (where the source alloy contains approximately 0.16 at.%Zr). Both couples have approximately the same γ-layer growth rates as the couples with similar source alloys 1/Y, 1/W, and the 2/_ couples. Significant in the 4/_ couples is the Kirkendall-type porosity in the γ layer. Two points can be noted in regard to the porosity. First, there is roughly twice the amount of porosity in the γ layer in the 4/Y couple where no Zr is present. Second, the location of the porosity is always on the $\gamma + \beta$ side of the original $\gamma/\gamma + \beta$ interface. Micrographs illustrating these two points are shown in Figure C-5.

It may be inferred that the intrinsic diffusivity of Al is greater than the intrinsic diffusivities of Ni or Cr in $\gamma + \beta$ NiCrAl alloys. Interdiffusion of Ni, Cr, and Al occurs by the vacancy mechanism. In the four $\gamma + \beta$ alloys studied, Al diffuses from the high-Al $\gamma + \beta$ source alloy into the NiCr sink alloys while the Ni and Cr diffusion is in the opposite direction (Figures C-1b and C-1c). The appearance of the porosity in the $\gamma + \beta$ side of the diffusion couple indicates a very rapid diffusion of Al to the NiCr alloy resulting in a non-equilibrium concentration of vacancies on the $\gamma + \beta$ side. It is possible that the porosity is a result of vacancy coalescence into larger pores. This suggestion is supported by the fact that the intrinsic diffusivity of Al is greater than the intrinsic diffusivity of Ni in Ni solid solution binary alloys (70,71).

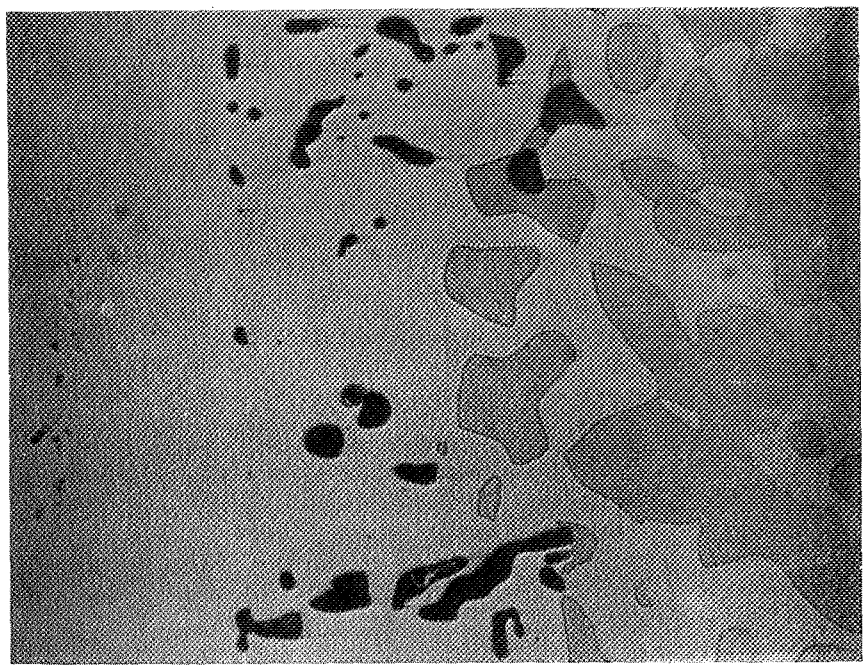

a

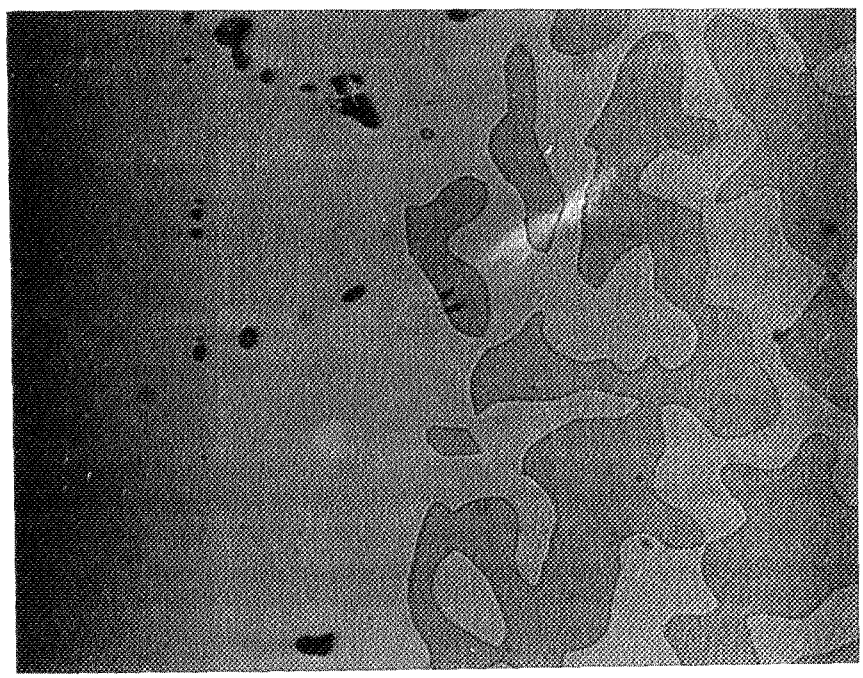

b

Figure C-5 Diffusion couples 4/Y (a.) and 4-Zr/Y (b.) after a 96 hour anneal at 1200 °C. Couple 4/Y contains approximately twice the porosity of couple 4-Zr/Y. The original $\gamma/\gamma+\beta$ interface is faintly observable in the left half of each micrograph. (200x)

The lower fraction of porosity in the Zr-containing alloy can also be explained by reference to a non-equilibrium concentration of vacancies in the $\gamma + \beta$ side of the diffusion couple. Zr atoms are relatively large and would introduce compressive stresses about the Zr atoms in the Ni solid solution matrix. Formation of Zr-vacancy complexes could reduce the stress about each Zr atom. Hence, the formation of Zr-vacancy complexes would reduce the over-abundance of free vacancies, thus reducing the porosity in the Zr-containing couple.

Discussion of Analysis

It was decided to employ a binary analysis to determine a single diffusion coefficient approximating D_{AlAl}. This decision was based on the previous observation that the Al diffusion was most strongly influenced by the Al concentration gradient. An analytical solution was derived to describe the diffusion of Al and the resulting parabolic growth of the γ layer in $\gamma/\gamma + \beta$ diffusion couples. Five assumptions were necessary for this analysis:

1. The diffusion coefficients were concentration independent.
2. The $\gamma/\gamma + \beta$ interface was planar.
3. No diffusion occurred in the $\gamma + \beta$ region.
4. The partial molar volume of Al was independent of concentration and phase.
5. The driving force for diffusion of Al was solely due to the Al concentration gradient; i.e., cross-term effects were considered negligible.

The analytical solution (72) consists of an equation describing the Al concentration in the γ layer and original NiCr alloy as:

$$C_{Al}(x) = C_{Al}^{\gamma} \frac{[1 + \mathrm{erf}(\frac{x}{\sqrt{4Dt}})]}{[1 + \mathrm{erf}(\eta)]} \qquad (C\text{-}4)$$

where: $C_{Al}(x)$ = Al concentration measured from the original $\gamma/\gamma+\beta$ interface,

η = parameter specific to each $\gamma+\beta$ alloy defined below,

D = diffusion coefficient which approximates D_{AlAl}.

The γ-phase layer width is described by

$$\xi = 2\eta\sqrt{Dt} \tag{C-5}$$

where ξ is the γ-phase layer width. The η parameter is determined from a mass balance equation at the $\gamma/\gamma+\beta$ interface:

$$\frac{\eta\sqrt{\pi}\,(C^{0}_{Al} - C^{\gamma}_{Al})}{C^{\gamma}_{Al}} = \frac{\exp(-\eta^2)}{[1 + \mathrm{erf}(\eta)]} \tag{C-6}$$

where all symbols are as previously defined. Eq. C-6 can be numerically solved for the η parameter for each of the $\gamma+\beta$ alloys. From Eq. C-5 and the data in Figure C-4, the diffusion coefficient D may be determined. The parameter and diffusion coefficients are listed in Table C-3.

The assumptions made to facilitate a binary analysis were considered acceptable for approximating the diffusion coefficient. The $\gamma/\gamma+\beta$ interface was observed to thicken macroscopically as a planar interface, even though it was obviously not planar on the microscopic scale of the individual β-phase particles. No concentration gradients were measurable in the $\gamma+\beta$ region nor was there a detectable decrease in the volume fraction of the β phase near the $\gamma/\gamma+\beta$ interface, both observations indicating insignificant diffusion in the $\gamma+\beta$ region. The effect of a variable partial molar volume of Al on the diffusion coefficient should be small and within the accuracy of the other measurements. The validity of ignoring the cross-term effects on the Al diffusion has previously been discussed. No general statement can be made concerning the concentration dependence of the diffusion coefficient. It can be observed that for the three different alloys examined, the measured diffusion

TABLE C-3

INTERFACE COMPOSITIONS AND DIFFUSION COEFFICIENTS MEASURED ON THE $\gamma/\gamma+\beta$ DIFFUSION COUPLES

Couples	C^{γ}_{Cr} (at. %)	C^{γ}_{Al} (at. %)	η	ξ^2/t (10^{-10} cm^2/s)	D (10^{-10} cm^2/s)
1/W		12.2-12.7[1]	0.38-0.39	7.6	12.5-13.2
1/Y	24.7	12.2-12.7	0.38-0.39	7.2	11.8-12.5
2/W		11.0-11.2[2]	0.32	7.0	17.1
2/X		11.0-11.2[2]	0.32	7.6	18.6
2/Y	29.6	11.0-11.2	0.32	7.1	17.3
2/Z		11.0-11.2[2]	0.32	7.6	18.6
3/W	35.0	8.9-9.4[3]	^0.2-0.22	1.5	7.7-9.4

[1] Assumed equal to 1/Y couple

[2] Assumed equal to 2/Y couple

[3] Estimated from Ni-17Cr-28Al-0.18Zr alloy examined in the oxidation section of this thesis

coefficients vary by less than a factor of three, not a very large difference with regard to diffusion coefficients, suggesting little concentration dependence over the range of concentrations examined.

It is somewhat informative to compare the measured diffusion coefficients with the interdiffusion coefficients, $\tilde{D}$, in the Ni solid solution regions of the Ni-Al and Ni-Cr binary systems. The measured diffusion coefficients were in the range of $\tilde{D}_{Ni-Al}$ in the Ni-Al system shown in Table C-4. This observation implies (64) that the chemical potential of Al in NiCrAl alloys is principally a function of Al concentration and virtually independent of Cr concentration. This suggestion is consistent with the previous observation that D_{AlCr} is significantly less than D_{AlAl}. Further support of the weak Cr-concentration influence is that the phase boundary between the γ and the $\gamma + \beta$ regions on the NiCrAl phase diagram lies almost parallel to the NiCr side, indicating a weak dependence of the chemical potential of Al on the Cr concentration (64).

The exact diffusion coefficient used in the computer model developed and used in this report is shown in Table C-5. The diffusion coefficients used for the Ni-17Cr-28Al-0.18Zr and the Ni-14Cr-25Al-0.12Y alloys were slightly less than the diffusion coefficients measured on the equivalent alloy not containing Zr or Y. Justification for this slight decrease was suggested previously in the section discussing the effect of Zr on the diffusion of Al.

TABLE C-4

COMPARISON OF Ni-Al AND Ni-Cr INTERDIFFUSION COEFFICIENTS AT 1200°C

$\tilde{D}_{Ni-Al}$ (10^{-10} cm^2/s)	Reference
7.0 - 23.7	71
7.6	68
14 - 24	70
$\tilde{D}_{Ni-Cr}$	
3.3 - 4.5	37
1.8 - 3.9	73
D	
7.7 - 18.6	This Study

TABLE C-5

DIFFUSION COEFFICIENTS USED IN THE NUMERICAL MODEL

Alloy	D (10^{-10} cm^2/s)
Ni-13Cr-25Al-0.05Zr	12.3
Ni-14Cr-25Al-0.12Y	10.0
Ni-17Cr-24Al-0.04Zr	17.1
Ni-17Cr-28Al-0.18Zr	6.2

APPENDIX D

THE NUMERICAL MODEL

A numerical model utilizing finite-difference techniques was developed to simulate the Al diffusion during the cyclic oxidation of $\gamma + \beta$ NiCrAl alloys. Finite-difference techniques have been well established as an effective tool in modeling complex diffusion behavior in both binary and ternary alloys. The numerical model developed in this study incorporates the complex boundary conditions at both the oxide/metal interface and the $\gamma/\gamma + \beta$ interface observed to occur during the cyclic oxidation of $\gamma + \beta$ NiCrAl alloys.

Seven assumptions were made in the development of the numerical model. They were:

1. The diffusion coefficients were concentration independent.
2. The $\gamma/\gamma + \beta$ interface was planar.
3. The oxide/γ-layer interface was planar.
4. The partial molar volume of Al was independent of concentration and phase.
5. The sample heat-up and cool-down times for each cycle were rapid; i.e., diffusion only occurred at 1200°C.
6. Only Al_2O_3 was formed.
7. The driving force for diffusion of Al was solely due to the Al concentration gradient.

The validity of each assumption is discussed in the numerical modeling section of this report.

The selective oxidation of Al in $\gamma + \beta$ NiCrAl alloys results in the growth of a γ layer in the near-surface region. A solution of Fick's second law yields the Al concentration/distance profiles in this layer. A unique solution

to Fick's second law requires knowledge of the boundary conditions at the oxide/γ-layer interface and at the $\gamma/\gamma+\beta$ interface. A mass balance at each interface yields their position and velocity. The finite-difference equivalent of Fick's second law, the mass balance at the oxide/γ-layer interface, and the mass balance at the $\gamma/\gamma+\beta$ interface are shown in Table D-1.

The finite-difference technique requires definition of a grid of points across the γ layer. The grid points are equally spaced across the layer, each point being associated with a specific Al concentration. Six to eight grid points were used in the present study. A linear concentration profile across a γ layer of 0.1 - 1.0 μm width was assigned as an initial starting condition. The initial concentration profile and γ-layer width were chosen so as to have negligible effect on the final solution. An initial concentration profile for six grid points is shown in Figure D-1. The grid spacing, Δx, is determined by dividing the γ-layer width ($\xi_1 - \xi_2$) by n, the number of grid spacings desired. Interfacial Al concentrations, C_1 and C_{n+1} (at the oxide/γ-layer interface and $\gamma/\gamma+\beta$ interface) were assigned as the boundary conditions.

The basic operation of the model is a sequential iteration of the finite-difference calculations for successive increments of time. The equations were therefore incorporated into a computer program to facilitate the repetitive calculations. Three fundamental calculations were performed in modeling the Al diffusion during the cyclic oxidation of NiCrAl alloys. The first calculation during the i'th iteration can be divided into two steps. First, the Al concentration at the oxide/γ-layer interface (C_1) and the Al concentration at the $\gamma/\gamma+\beta$ interface (C_{n+1}) were assigned for the particular oxidation time $i\Delta t$. Second, the finite-difference form of Fick's second law operated on each concentration/grid point in the γ layer, excluding the two interface concentrations previously assigned. The first fundamental calculation

TABLE D-1

EQUATIONS USED IN NUMERICAL MODEL

Partial Differential Equation	Finite Difference Equivalent
a. Fick's Second Law	
$\frac{dC}{dt} = D \frac{d^2C}{dx^2}$	$\frac{(C_j'^{*}-C_j)}{\Delta t} = D \frac{C_{j+1}-2C_j+C_{j-1}}{\Delta x^2}$ $j=2,n$
b. Mass Balance at $\gamma/\gamma+\beta$ Interface	
$(C_0-C_{\gamma\beta}) \frac{d\xi_1}{dt} = J_1$	$(C_0-C_{\gamma\beta}) \frac{\Delta\xi_1}{\Delta t} = D \frac{C_{n+1}C_n}{\Delta x}$
c. Mass Balance at the oxide/γ layer Interface	
$\frac{d\xi_2}{dt} = \overline{V} J_2$	$\frac{\Delta\xi_2}{\Delta t} = \overline{V} D \frac{C_2-C_1}{\Delta x}$
d. Murray-Landis Transformation	
none	$C_j''^{**} = C_j + \frac{C_{j+1}-C_{j-1}}{2\Delta x} \frac{j-1}{n} \Delta\xi_1 + \frac{n-j+1}{n} \Delta\xi_2$ $j=2,n$

$^{*}C_j'$ refers to the concentration at the jth grid point at time $t+\Delta t$

$^{**}C_j''$ refers to the concentration at the jth grid point at time t after the M-L shift.

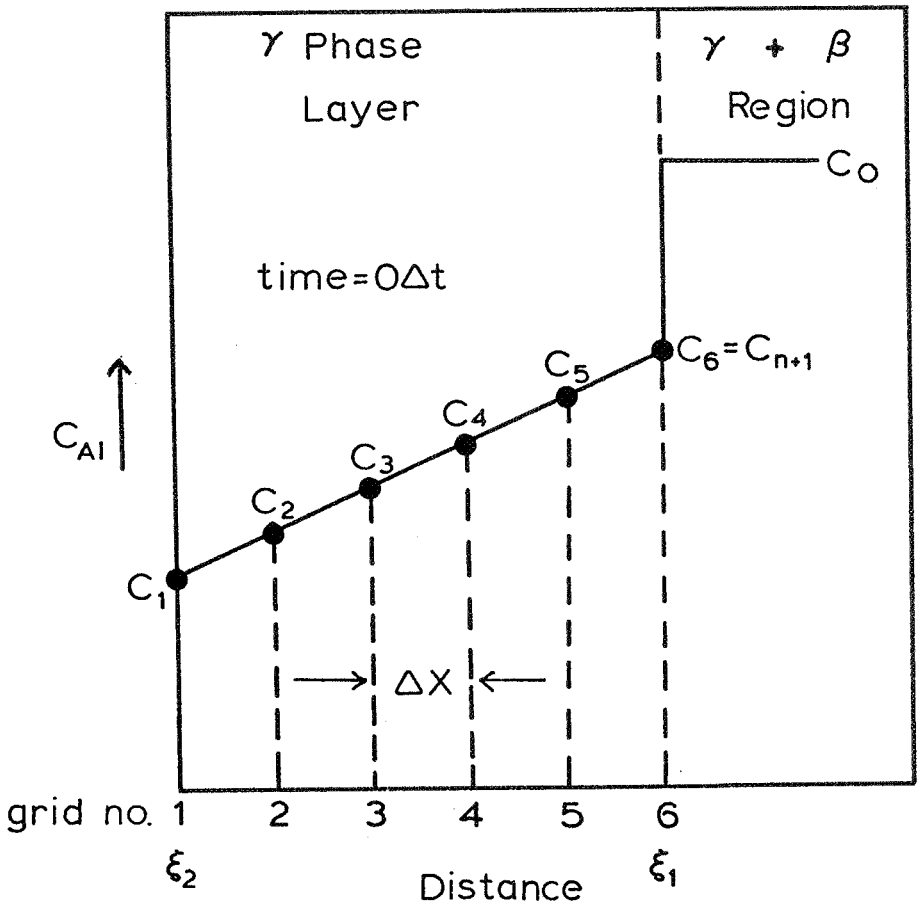

Figure D-1 Initial Concentration Profile for 6 Grid Points

n = 5

● - C_1, C_6 at time = 0

$\xi_1 \cong 0.1 - 1.0\mu m$

$\xi_2 = 0.0$

$\Delta X = (\xi_1 - \xi_2)/n = 0.02\mu m$

C_0 = bulk composition of alloy

assigning the interface concentrations and operating on each grid point at time $i\Delta t$ is shown schematically in Figure D-2a.

The second calculation during the same iteration, $i\Delta t$, can also be divided into two parts. First, the flux of Al from the $\gamma+\beta$ region into the γ layer (J_1) is calculated and the $\gamma/\gamma+\beta$ interface position (ξ_1) is increased accordingly. Second, the flux of Al passing from the γ layer to the oxide (J_2) is calculated and the oxide/γ-layer interface position (ξ_2) is increased accordingly. The second fundamental calculation is schematically shown in Figure D-2b.

The third calculation determines the new grid position based on the increased γ-layer width and adjusts the concentrations from the old to the new grid positions. This shift is sometimes referred to in the literature as the Murray-Landis (M-L) transformation (74). The third fundamental calculation is schematically shown in Figure D-2c. The finite-difference form of the M-L transformation is listed in Table D-1. Following each iteration, the time is incremented to $(i+1)\Delta t$, the Al concentration at both interfaces (C_1 and C_{n+1}) are recalculated, and the three fundamental calculations are repeated.

The total weight of Al consumed in the oxidation reaction can be determined from the flux of Al entering the oxide at the oxide/γ-layer interface. The Al consumed during each iteration can be estimated as the product of the flux (J_2) and the time interval (Δt). The total weight of Al consumed at a specific time is simply the sum of the weights of Al consumed during each iteration up to the specified time. A conversion of the units of the weight of Al consumed from that involving atomic percent to the more appropriate units of milligrams required the density of the $\gamma+\beta$ alloys. A simple rule of mixtures of the density of each pure metal weighted by the atomic fraction

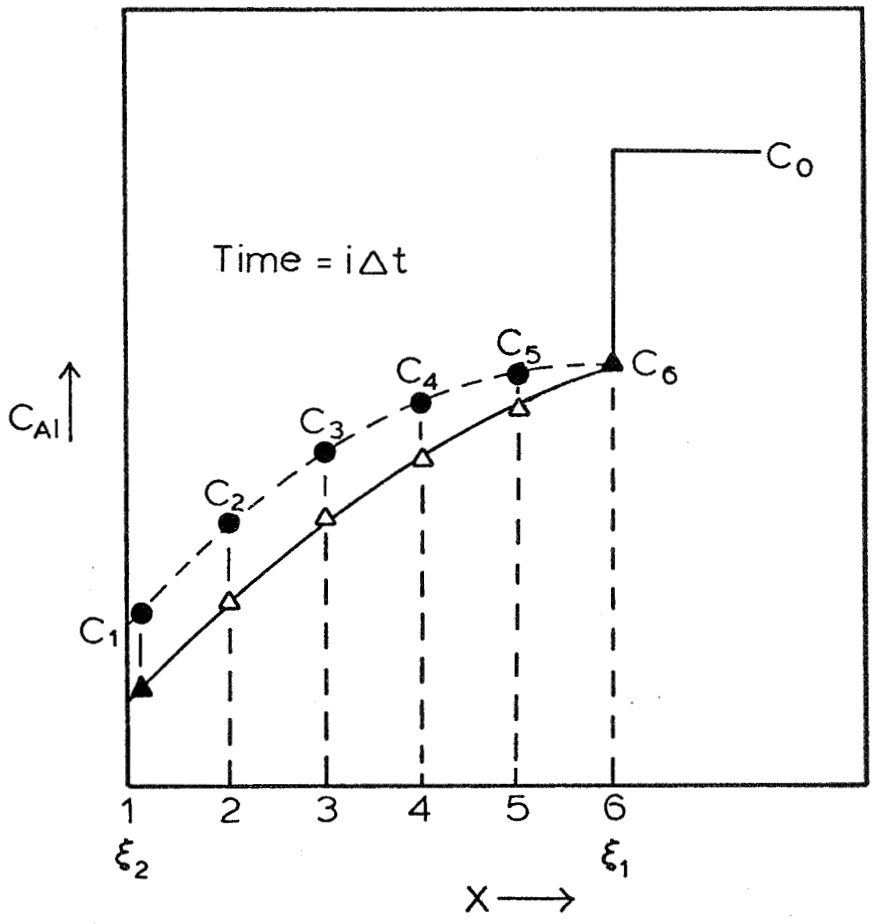

Figure D-2a Main Iteration Scheme

Operation of Fick's Second Law for the ith iteration

▲ - C_1, C_6 at time $i\Delta t$

△ - C_j concentration at grid j after calculation of Fick's Second Law

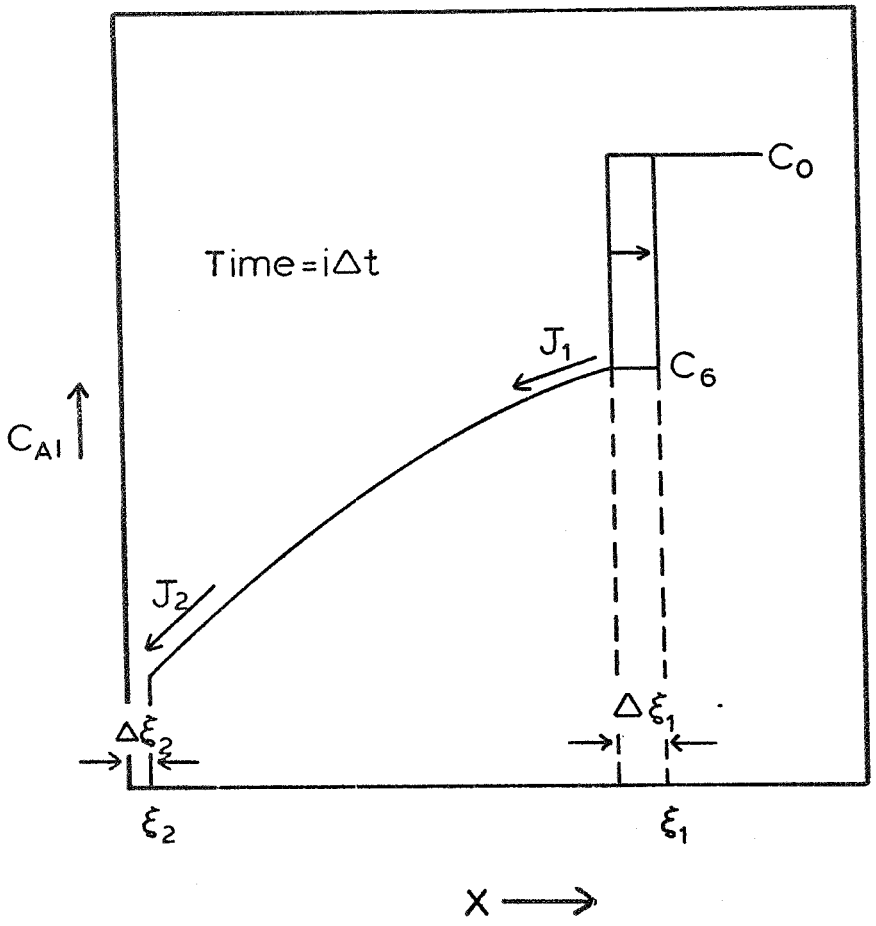

Figure D-2b Main Iteration Scheme

Interface Motion

$$\Delta\xi_1 = J_1\Delta t/(C_0 - C_6)$$
$$\Delta\xi_2 = \overline{V}_{Al}J_2\Delta t$$
$$\xi_1 = \xi_1 + \Delta\xi_1$$
$$\xi_2 = \xi_2 + \Delta\xi_2$$

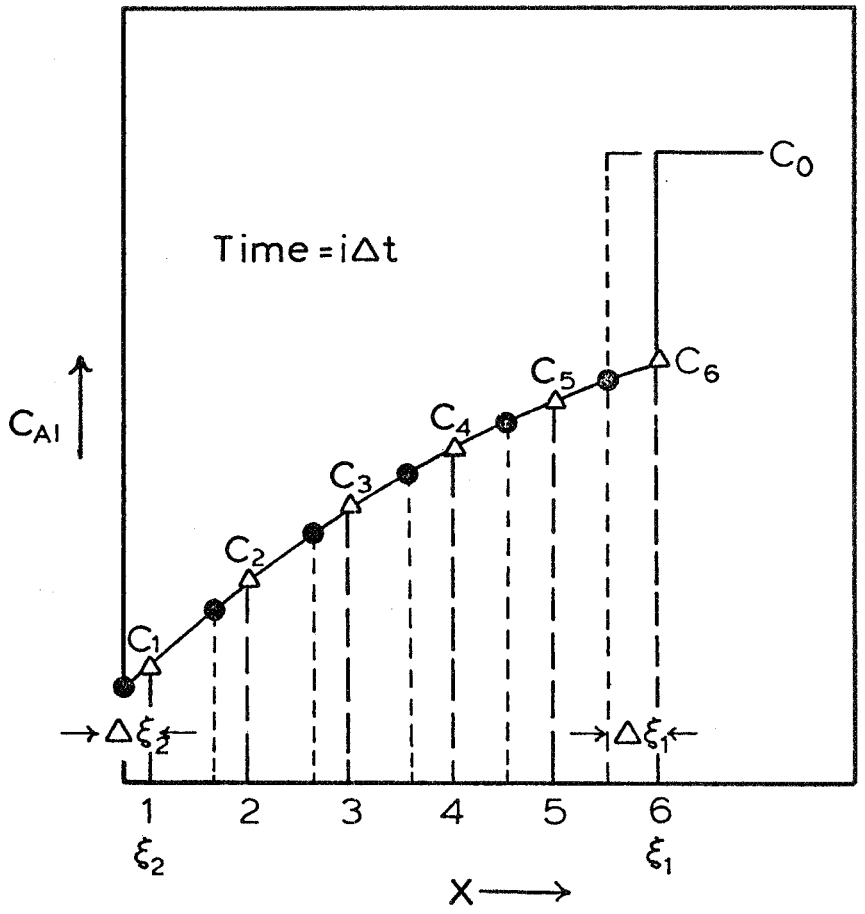

Figure D-2c Main Iteration Scheme

New Grid Position and Concentration Correction

$\Delta X = (\xi_1 - \xi_2)/n$

● - concentration/grid point before M-L shift

Δ - concentration/grid point after M-L shift

of each component in the alloy was used to estimate the density. Measured and estimated densities for some γ and $\gamma + \beta$ alloys are listed in Table D-2.

Recession of the metal surface at the oxide/metal interface is dependent on the partial molar volume of Al in the γ phase (see Table D-1c). The partial molar volume of Al is a concentration-dependent variable. To determine the motion of the oxide/metal interface, the partial molar volume of Al ($\overline{V}_{Al}$) was estimated from the lattice parameter data for a Ni-20Cr-5Al alloy (67).[†] The determined value of 7.1 cm^3/mole can be compared with the molar volumes of pure Ni, Cr, and Al of 6.6 cm^3/mole, 7.2 cm^3/mole, and 10.0 cm^3/mole, respectively. The partial molar volume was converted from units of cm^3/mole to units of inverse atomic percent to be compatible with the concentration units in the computer program. The calculation to determine the partial molar volume of Al is shown in the following section.

The partial molar volume of Al determined for a Ni-20Cr-5Al alloy was taken as an average value for the γ layer. Accounting for the motion of the oxide/metal interface results in an increase in the width of the γ layer (measured from the original metal surface) and a corresponding increase in the weight of Al consumed. The γ layer increased only 6 - 12 percent in the four alloys studied when the oxide/metal interface motion was taken into account. For a specific alloy composition, increasing or decreasing the value of $\overline{V}_{Al}$ by 50% (more than spanning the range of the pure element molar volumes) resulted in less than a 5% change in the γ-layer width. Hence, using an average value for the partial molar volume of Al in the γ layer was considered as an acceptable approximation in the present modeling study.

The validity of the finite-difference technique was verified by comparison

---

[†](wt.%)

TABLE D-2

MEASURED AND ESTIMATED DENSITIES OF SELECT NiCrAl ALLOY

Alloy (at. %)	Measured Density (gms/cc)	Estimated Density (gms/cc)
Ni-13Cr-25Al-0.05Zr	7.4	7.2
Ni-19Cr-24Al-0.04Zr	7.1	7.1
Ni-21Cr-16Al	7.4	7.5
Ni-36Cr-6Al	7.8	7.9
Ni-26Cr-10Al	7.8	7.8
Ni-26Cr-6Al	8.1	8.2
Ni-8Cr-8Al	8.4	8.4

with a closed-form analytical solution. Derivation of a closed-form solution required the same assumptions previously given for the finite-difference solution. The general form of the analytical solution is given in Reference 72. In addition, the closed-form solution also required the assumption of a time-dependent concentration at the oxide/metal interface and at the $\gamma/\gamma+\beta$ interface. As the number of grids used in the finite-difference solution was increased, the solution "converged" to the closed-form solution. The relative difference between the predicted interface position and the predicted weight of metal consumed, for both solutions, decreased as the number of grid points used in the numerical solution was increased (Figure D-3). For the case of four or more grid points, the relative difference between the closed-form and finite-difference solutions was less than 1%.

The computation time for the numerical solution increased as the number of grid points in the γ layer was increased. The time interval for each iteration (Δt) decreased as the number of grid points was increased, while the number of calculations during each iteration also increased. The number of necessary iterations for the indicated number of grid points is shown in parentheses in the lower plot in Figure D-3. Six to eight grid points were chosen as a balance between the necessary computation time and an acceptable error in the finite-difference model.

Closely associated with a proper choice of the number of grid points is an appropriate choice of the time interval (Δt) during each iteration. The conservative condition

$$\Delta t = \frac{0.25\ \Delta x^2}{D}$$

was used for most of the modeling of the four alloys in this study. Doubling the time interval resulted in less than a 1% relative difference between

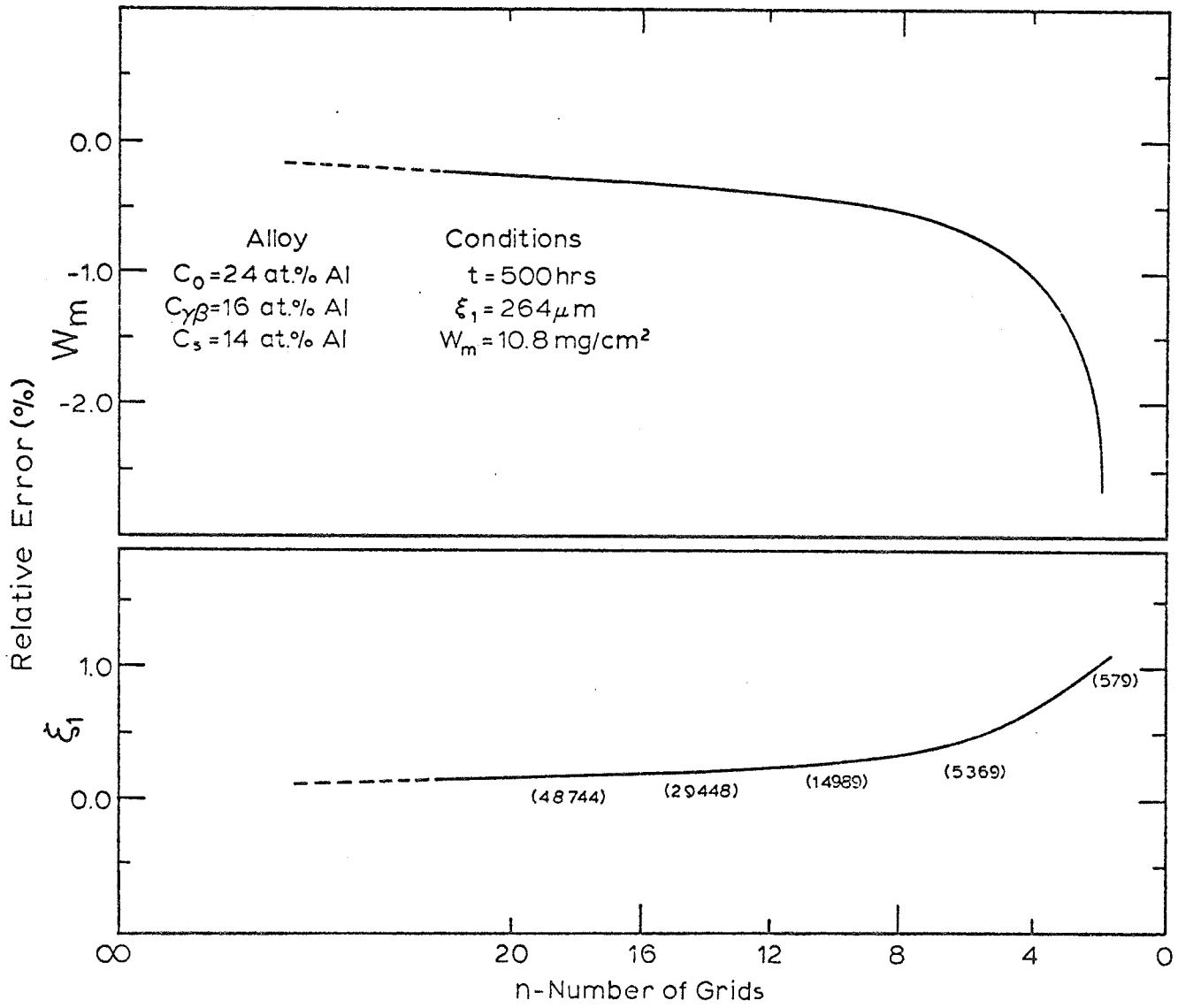

Figure D-3 Convergence of the numerical model to the analytical solution. Number in parentheses is the number of iterations for the numerical solution.

solutions, whereas tripling the time interval produced no solution (similar to the case of one grid point in the upper plot in Figure D-3).

A complete listing of the computer program incorporating the finite-difference solution is included at the end of this appendix.

Partial Molar Volume of Al

The partial molar volume of Al at the concentration Ni-20Cr-5Al (wt.%) was estimated by using a second-order Taylor series expansion. The partial molar volume of Al at the concentration Ni-20Cr-5Al is determined by projecting a plane tangent to the three-dimensional volume surface at the concentration Ni-20Cr-5Al. The intersection of the tangent plant with the pure Al axis is the partial molar volume of Al at the concentration Ni-20Cr-5Al. The appropriate form of the Taylor series expansion is:

$$\bar{V}_{Al}\Big|_{100Al} = V\Big|_{Ni\text{-}20Cr\text{-}5Al} + \frac{\Delta V}{\Delta Cr}\Big|_{Ni\text{-}20Cr\text{-}5Al}(0.0 - 0.2) + \frac{\Delta V}{\Delta Ni}\Big|_{Ni\text{-}20Cr\text{-}5Al}(0.0 - 0.75)$$

where: $\bar{V}_{Al}$ = intersection of the tangent plane with the pure Al axis; this value is the partial molar volume of Al at the concentration Ni-20Cr-5Al.

V = molar volume of a Ni-20Cr-5Al alloy.

$\frac{\Delta V}{\Delta Cr}$ = change in the molar volume with changing Cr concentration evaluated at the concentration Ni-20Cr-5Al.

$\frac{\Delta V}{\Delta Ni}$ = change in the molar volume with changing Ni concentration evaluated at the concentration Ni-20Cr-5Al.

The volume changes were estimated from the lattice parameter data of Reference 67. The partial molar volume of Al was initially determined in units of $(\text{Å})^3$/unit cell and was converted to cm^3/mole by reference to the fact of four atoms per unit cell in the face-centered cubic lattice structure and Avogadro's number of atoms in a mole of metal.

```
3052*NASA(1).THRE
      C     NASA.ALFLUX3      VERSION 3
      C     NUMERICAL SOLUTION TO THE DIFFUSIONAL TRANSPORT OF AL IN
      C     NI-CR-AL ALLOYS UNDERGOING CYCLIC OXIDATION.
      C
      C     THIS VERSION OF ALFLUX3 ALLOWS VARIABLE INPUT OF C2, THE
      C     AL CONCENTRATION AT THE OXIDE/GAMMA INTERFACE.
      C     PARABOLIC INTERFACE MOTION DOES NOT RESULT.
      C
      C     PROBLEM: AL DIFFUSING OUT OF A TWO-PHASE GAMMA+BETA
      C     REGION, THROUGH A ONE-PHASE GAMMA REGION TO FORM
      C     AN OXIDE SCALE ON THE SURFACE.  THE AL CONCENTRATION
      C     IN THE GAMMA PHASE VARIES FROM ALSURF AT THE OXIDE-GAMMA
      C     INTERFACE TO ALAB, THE SOLUBILITY LIMIT OF AL IN THE GAMMA
      C     PHASE.  A PLANAR INTERFACE IS ASSUMED WITH TWO MOVING
      C     BOUNDARIES, THE GAMMA/GAMMA+BETA (XI1) AND THE
      C     OXIDE/GAMMA (XI2) INTERFACE
      C     THIS VERSION ALLOWS VARIABLE INPUT OF OXIDATION TIMES
      C
      C     INPUT-
      C
      C        CR,AL - INITIAL CR AND AL CONCENTRATION IN THE ALLOY (AT%)
      C             FORMAT - CR AT.% (CC 1-5), AL AT.% (CC 7-11)
      C             XX.XX,XX.XX
      C        CRAB,ALAB - CR,AL SOLUBILITY IN GAMMA PHASE
      C             FORMAT - SAME AS CR,AL ABOVE
      C             XX.XX,XX.XX
      C        ALSURF - AL CONCENTRATION AT THE OXIDE/GAMMA INTERFACE
      C             FORMAT - AL AT.% (CC 1-5)
      C             XX.XX
      C        D - DIFFUSION COEFFICIENT IN GAMMA PHASE
      C             FORMAT - CM*CM/SEC   SCIENTIFIC NOTATION
      C             XXX.XXEXX      IE. 8.92E-11
      C        TEMP - OXIDATION TEMPERATURE IN DEGREES CENTIGRADE
      C             FORMAT - XXXX.  IE. 1200
      C        VBAR - PARTIAL MOLAR VOLUME OF AL IN THE GAMMA PHASE
      C             FORMAT - XX.XX  (CC/MOLE AL)
      C        NUM - THE NUMBER OF OXIDATION TIMES REQUESTED
      C             FORMAT - XX
      C        OXTIME(K) - THE SPECIFIC OXIDATION TIMES IN HOURS
      C             FORMAT - XXXXX.,XXXXX.,XXX.,XX.,XX.
      C                      'NUM' # OF FIELDS EACH SEPERATED BY COMMAS
      C     OUTPUT -
      C
      C        XI1 - INTERFACE POSITION (GAMMA/GAMMA+BETA) (CM)
      C        XI2 - INTERFACE POSITION (OXIDE/GAMMA PHASE) (CM)
      C        WM - WEIGHT OF AL FORMING OXIDE (MG/CM*CM)
      C        FLUX OF AL AT OXIDE-GAMMA INTERFACE (MG/CM*CM*SEC)
      C        AL CONCENTRATION IN THE GAMMA PHASE
      C
      C
      C     ***************************************************************
      C           SET INITIAL CONDITIONS
      C     ***************************************************************
      C
      C
      C
            IMPLICIT REAL*8(A-H,L,M,O-Z)
            DOUBLE PRECISION J1,J2,NI,NIAB,JW,JGMS
            DIMENSION C(30),CNEW(30),DIST(30),OXTIME(30),CW(30)
            READ *, CR,AL
            READ *, CRAB,ALAB
            READ *, C(1)
            READ *, D
            READ *, TEMP
            READ *, VBAR
            READ *, NUM
            READ *, (OXTIME(NN), NN=1,NUM)
            READ *, N
            DO 15 NN=1,NUM
         15 OXTIME(NN)=OXTIME(NN)*3600
            NI=100-CR-AL
            NIAB=100-CRAB-ALAB
            XI1=1D-6
            XI2=0.0
            DELT=.25*XI1*XI1/(D*N*N)
            VBAR=VBAR*7.5/(ALAB*27.+CRAB*52.+NIAB*58.7)
            DENS=(NI*8.9+CR*7.2+AL*2.7)/100
            MSSAL=0.0
            PRINT *,N
      C
      C     ***************************************************************
      C     PRINT HEADINGS AND INPUT SAMPLE
```

```
C     ****************************************************************
C
      WRITE(6,150) CR,AL
  150 FORMAT(1H1,2X,'RESULTS FOR SAMPLE NI-',F5.2,'AT% CR-',F5.2,
     1       'AT% AL')
      WRITE(6,155) CRAB,ALAB
  155 FORMAT(1HO,5X,'CR,AL CONCENTRATION AT GAMMA/GAMMA+BETA ',
     1       'INTERFACE= ',2F6.2)
      WRITE(6,157) C(1)
  157 FORMAT(6X,'AL CONCENTRATION AT THE OXIDE/GAMMA INTERFACE= ',
     1       F5.2)
      WRITE(6,160) TEMP
  160 FORMAT(1HO,5X,'OXIDATION TEMPERATURE (DEG C) = ',F5.0)
      WRITE(6,200) D
  200 FORMAT(1HO,5X,'DIFFUSION COEFFICIENT (CM*CM/SEC) =',E14.4)
      WRITE(6,210) VBAR
  210 FORMAT(1HO,5X,'PARTIAL MOLAR VOLUME (1/AT%) =',E14.4)
C
CCCC  ************************************************************
CCCC  SET INITIAL AL CONCENTRATION PROFILE
CCCC  USE LINEAR CURVE FOR INITIAL CONCENTRATION
CCCC  ************************************************************
C
      C(N+1)=ALAB
      DELX=XI1/N
      A=(ALAB-C(1))/N
      DO 20 J=2,N
   20 C(J)=C(1)+(J-1)*A
      TIME=DELT
      I=1
      K=1
C
CCCC  ************************************************************
CCCC  MAIN ITERATION LOOP FOLLOWS
CCCC  ************************************************************
CCCC
CCCC  ************************************************************
CCCC  CALCULATE THE FLUX AND THE CHANGE IN XI, DELXI
CCCC  ************************************************************
CCCC
C
   50 J1=(C(N-1)-4*C(N)+3*C(N+1))/(2*DELX)*D
      DELXI1=DELT*J1/(AL-C(N+1))
      XI1=XI1+DELXI1
      IF(TIME.GT.370000.) THEN
                C(1)=10.79-DSQRT(TIME/3600)*.012
      END IF
      J2=-ALPHA*D*(-C(3)+4.*C(2)-3.*C(1))/(2.*DELX)
      DELXI2=-VBAR*J2*DELT
      XI2=XI2+DELXI2
      DELX=(XI1-XI2)/N
      ALPHA=1./(1.-VBAR*C(1))
C
CCCC  AT.% TO GMS/CC CONVERSION
C
      DO 55 II=1,3
   55 CW(II)=C(II)*27./(C(II)*27+NIAB*58.7+(100.-NIAB-C(II))*52)
      JW=D*(-CW(3)+4.*CW(2)-3.*CW(1))/(2.*DELX)
      ALAVG=(ALAB+C(1))/2.
      CRAVG=100.-ALAVG-NIAB
      DENSG=(ALAVG*2.7+CRAVG*7.2+NIAB*8.9)/100.
      JGMS=JW*DENSG
C
CCCC  ************************************************************
CCCC  SET DELT TO PROPER INCREMENT
CCCC  ************************************************************
C
      DELT=.25*DELX*DELX/D
      TIME=TIME+DELT
C
CCCC  ************************************************************
CCCC  CALCULATE THE FLUX AND THE MASS OF ALUMINUM LEAVING THE
CCCC  SYSTEM AT THE GAMMA-OXIDE INTERFACE
CCCC  ************************************************************
C
      MGFLUX=JGMS*1000.
      MGAL=MGAL+ABS(MGFLUX)*DELT
C
CCCC  ************************************************************
C     USE THE MURRAY-LANDIS TRANSFORMATION TO SHIFT THE
C     CONCENTRATIONS BACK TO THE CALCULATED CURVE
```

```
C     ************************************************************
C
C
      DO 60 J=2,N
   60 CNEW(J)=C(J)+(C(J+1)-C(J-1))/(2*DELX)
     1         *(DELXI1*(J-1)/N+DELXI2*(N-J+1)/N)
      DO 65 J=2,N
   65 C(J)=CNEW(J)
C
C     ************************************************************
C     CALCULATE NEW CONCENTRATIONS USING FICK'S 2ND LAW
C     ************************************************************
C
      DO 70 J=2,N
   70 CNEW(J)=C(J)+(D*DELT*(C(J+1)-2*C(J)+C(J-1))/(DELX*DELX))
      DO 75 J=2,N
   75 C(J)=CNEW(J)
C
      IF(TIME.EQ.360000) THEN
      C(N+1)=0.0500*(TIME/3600)**0.5+9.58
      END IF
C     ********* MAX ITERATION CHECK ******************************
C
      IF(I.EQ.200000) THEN
                      WRITE(6,100)
  100                 FORMAT( 1X,'MAX # OF ITERATIONS EXCEEDED')
                TIME=TIME/3600
                 PRINT *,TIME,DELT,XI1
                      STOP
                END IF
      I=I+1
C
C     ******** IF TIME EQUALS OXTIME(K) **************************
C     ******** PRINT RESULTS AND STOP                 ************
C
      IF(TIME.GT.(OXTIME(K)-OXTIME(K)/200)) THEN
                      DIST(1)=XI2
                      WM=MGAL
                      TIMEH=TIME/3600
      WRITE(6,175) TIMEH
  175 FORMAT(///,5X,'OXIDATION TIME (HOURS) =',F7.1)
      WRITE(6,250)
  250 FORMAT(///,5X,'CONCENTRATION PROFILE FOR GAMMA PHASE',
     1       ///,5X,'DISTANCE (CM)',10X,'AL (AT%)',//)
      DO 90 J=2,N+1
   90 DIST(J)=(J-1)*DELX+XI2
      DO 95 J=1,N+1
   95 WRITE(6,300) DIST(J),C(J)
  300 FORMAT(8X,F9.5,12X,F6.3)
      WRITE(6,400) WM
  400 FORMAT(1HO,5X,'** WM - AL LOSS FROM SAMPLE (MG/CM*CM) =',
     1       E11.5)
      WRITE(6,350) XI1
  350 FORMAT(1HO,5X,'XI1 POSITION (CM) =',E11.5)
      WRITE(6,375) XI2
  375 FORMAT(1HO,5X,'XI2 POSITION (CM) =',E11.5)
      WRITE(6,450) MGFLUX
  450 FORMAT(1HO,5X,'FLUX AT XI2 (OXIDE/GAMMA PHASE INTERFACE (MG/'
     1'CM*CM*SEC) =',E9.3,///)
      PRINT *,I
      IF(K.GE.NUM) STOP
      K=K+1
      GO TO 50
      ELSE
      GO TO 50
      END IF
      END
```

REFERENCES

1. G. W. Goward, Source Book on Materials for Elevated Temperature Applications, pp. 369-386, ASM, 1979.

2. G. R. Wallwork and A. Z. Hed, Oxid. of Met., 3 (1971) 171.

3. G. W. Goward, J. of Metals, 22 (1970) 31.

4. S. J. Grisaffe, The Superalloys, C. T. Sims and W. C. Hagel, Editors, pp. 341-370, John Wiley and Sons, New York, 1972.

5. C. S. Giggins and F. S. Pettit, J. Electrochem. Soc., 118 (1971(1782.

6. P. Kofstad, High-Temperature Oxidation of Metals, pp. 112-146, John Wiley and Sons, New York, 1966.

7. F. S. Pettit, Trans. TMS-AIME, 239 (1967) 1296.

8. C. Wagner, J. Electrochem. Soc., 99 (1952) 369.

9. S. R. Levine, Met. Trans., 94 (1978) 1237.

10. D. P. Whittle, Acta. Met., 17 (1969) 1247.

11. J. L. Smialek and C. E. Lowell, J. Electrochem. Soc., 121 (1974) 800.

12. C. A. Barrett and C. E. Lowell, Oxid. of Met., 11 (1977) 199.

13. J. K. Tien and J. M. Davidson, Stress Effects and the Oxidation of Metals, J. V. Cathcart, Editor, pp. 200-219, TMS-AIME, New York, 1975.

14. D. L. Douglass, Oxidation of Metals and Alloys, pp. 137-156, ASM, Ohio, 1971.

15. C. S. Giggins, E. J. Felten, and F. S. Pettit, Stress Effects and the Oxidation of Metals, J. V. Cathcart, Editor, pp. 245-260, TMS-AIME, New York, 1975.

16. G. C. Wood, Oxidation of Metals and Alloys, pp. 201-234, ASM, Ohio, 1971.

17. C. A. Barrett, J. R. Johnston, and W. A. Sanders, Oxid. of Met., 12 (1978) 343.

18. F. H. Stott, G. C. Wood, and M. G. Hobby, Oxid. of Met., 3 (1971) 103.

19. C. S. Giggins and F. S. Pettit, "Oxide Scale Adherence Mechanisms," Second Annual Report, PWA-5042 (1974).

20. C. A. Barrett and C. E. Lowell, Oxid. of Met., 9 (1975) 307.

21. B. H. Kear, F. S. Pettit, D. E. Fornwalt, and L. P. Lemaire, Oxid. of Met., 3 (1971) 557.

22. F. A. Golightly, G. C. Wood, and F. H. Stott, Oxid. of Met., 14 (1980) 217.

23. I. A. Kvernes and P. Kofstad, Met. Trans., 3 (1972) 1511.

24. F. H. Stott, I. G. Wright, T. Hodgkiess, and G. C. Wood, Oxid. of Met., 11 (1977) 141.

25. A. Kumar, M. Nasrallah, and D. L. Douglass, Oxid. of Met., 8 (1974) 227.

26. F. H. Stott, G. C. Wood, and F. A. Golightly, Corros. Sci., 19 (1979) 869.

27. A. S. Kahn, C. E. Lowell, and C. A. Barrett, J. Electrochem. Soc., 127 (1980) 670.

28. J. K. Tien and F. S. Pettit, Met. Trans., 3 (1972) 1587.

29. F. A. Golightly, F. H. Stott, and G. C. Wood, Oxid. of Met., 10 (1976) 163.

30. I. A. Kvernes, Oxid. of Met., 6 (1973) 45.

31. J. D. Kuenzly and D. L. Douglass, Oxid. of Met., 8 (1974) 139.

32. H. Y. Ku, J. Appl. Phys., 35 (1964) 3391.

33. B. D. Bastow, D. P. Whittle, and G. C. Wood, Oxid. of Met., 12 (1978) 413.

34. H. E. Evans, D. A. Hilton, R. A. Holm, and S. S. Webster, Oxid. of Met., 14 (1980) 235.

35. D. P. Whittle, G. C. Wood, D. J. Evans, and D. B. Scully, Acta. Met., 15 (1967) 1747.

36. G. L. Wulf, M. B. McGirr, and G. R. Wallwork, Corros. Sci., 9 (1969) 739.

37. T. Hodgkiess, G. C. Wood, D. P. Whittle, and B. D. Bastow, Oxid. of Met., 12 (1978) 439.

38. T. Hodgkiess, G. C. Wood, D. P. Whittle, and B. D. Bastow, Oxid. of Met., 14 (1980) 263.

39. C. E. Lowell and D. L. Deadmore, "The Role of Thermal Shock in Cyclic Oxidation," NASA TM-78876 (1978).

40. D. L. Deadmore and C. E. Lowell, Oxid. of Met., 11 (1977) 91.

41. I. G. Wright and B. A. Wilcox, Oxid. of Met., 8 (1974) 283.

42. I. M. Allam, D. P. Whittle, and J. Stringer, Oxid. of Met., 12 (1978) 35.

43. I. G. Wright, B. A. Wilcox, and R. I. Jaffee, Oxid. of Met., 9 (1975) 275.

44. C. A. Barrett and C. E. Lowell, Oxid. of Met., 12 (1978) 293.

45. E. J. Felten, Oxid. of Met., 10 (1976) 23.

46. I. M. Allam, H. C. Akuezue, and D. P. Whittle, Oxid. of Met., 14 (1980) 517.

47. J. G. Fountain, F. A. Golightly, F. H. Stott, and G. C. Wood, Oxid. of Met., 10 (1976) 341.

48. C. A. Barrett, A. S. Khan, and C. E. Lowell, J. Electrochem. Soc., 128 (1981) 25.

49. T. Moroishi, H. Fujikawa, and H. Makiura, J. Electrochem. Soc., 126 (1979) 2173.

50. I. M. Allam, D. P. Whittle, and S. Stringer, Oxid. of Met., 13 (1979) 381.

51. F. H. Stott, F. A. Golightly, and G. C. Wood, Corros. Sci., 19 (1979) 889.

52. J. L. Smialek, Met. Trans., 9A (1978) 309.

53. C. E. Lowell, C. A. Barrett, R. W. Palmer, and J. L. Smialek, "Modeling of Cyclic Oxidation Damage," Presented at The Electrochemical Society Meeting, Hollywood, FL, October 1980.

54. C. A. Barrett and A. F. Presler, "COREST: A Fortran Computer Program to Analyze Paralinear Oxidation Behavior and Its Application to Chromic Oxide Forming Alloys," NASA TN D-8132 (1976).

55. D. P. Whittle, Oxid. of Met., 4 (1972) 171.

56. D. P. Whittle, D. J. Evans, D. B. Scully, and G. C. Wood, Acta. Met., 15 (1967) 1421.

57. C. A. Barrett, Private Communication, August 1981.

58. R. A. Rapp, Corrosion, 21 (1965) 382.

59. K. M. Vedula, A. W. Funkenbush, and R. W. Heckel, "A Mathematical Model for Internal Oxidation," submitted to Oxid. of Met. (1981).

60. A. J. Hickl and R. W. Heckel, Met. Trans., 6A (1975) 431.

61. J. I. Goldstein and E. Randich, Met. Trans., 8A (1977) 105.

62. E. Randich and J. I. Goldstein, Met. Trans., 6A (1975) 1553.

63. G. W. Roper and D. P. Whittle, "Multicomponent Diffusion," submitted to J. Int. Met. Rev., 1979.

64. G. W. Roper and D. P. Whittle, Met. Sci., 14 (1980) 21.

65. J. I. Goldstein, Practical Scanning Electron Microscopy, J. I. Goldstein and H. Yakowitz, Editors, pp. 49-94, Plenum Press, New York, 1975.

66. EDIT/EP Operators Manual, EDAX International, Inc., Manual #80-00503-00, 1975.

67. A. Taylor and R. W. Floyd, J. Inst. Metals, 81 (1952) 451.

68. A. Green, M. Eng. Thesis, University of Liverpool, 1975.

69. A. Zyskowski, unpublished research, Michigan Technological University, 1981.

70. M. M. P. Janssen, Met. Trans., 4 (1973) 1623.

71. T. Yamamoto, T. Takashima, and K. Nishida, Nippon Kinzoku Gakkaishi, 44 (1980) 294 and Diffusion and Defect Data, 20 (1980) 95.

72. R. F. Sekerka, C. L. Jeanfils, and R. W. Heckel, Lectures on the Theory of Phase Transformations, H. I. Aaronson, Editor, pp. 117-169, TMS-AIME, New York, 1975.

73. M. S. Seltzer and B. A. Wilcox, Met. Trans., 3 (1972) 2357.

74. D. Murray and F. Landis, Trans. ASME, Series D, 81 (1959) 106.

1. Report No.	2. Government Accession No.	3. Recipient's Catalog No.
NASA CR-165544		

4. Title and Subtitle	5. Report Date
SOLUTE TRANSPORT DURING THE CYCLIC OXIDATION OF Ni-Cr-Al ALLOYS	May 1982
	6. Performing Organization Code

7. Author(s)	8. Performing Organization Report No.
James A. Nesbitt	None
	10. Work Unit No.

9. Performing Organization Name and Address	11. Contract or Grant No.
Michigan Technological University Department of Metallurgical Engineering Houghton, Michigan	NSG-3215
	13. Type of Report and Period Covered
12. Sponsoring Agency Name and Address	Contractor Report
National Aeronautics and Space Administration Washington, D. C. 20546	14. Sponsoring Agency Code 505-33-12

15. Supplementary Notes Final report. Project Manager, Charles A. Barrett, Materials Division, NASA Lewis Research Center, Cleveland, Ohio 44135. Report was submitted as a thesis in partial fulfillment of the requirements for the degree Master of Science in Metallurgical Engineering to Michigan Technological University, Houghton, Michigan.

16. Abstract

The Al transport during the cyclic oxidation of $\gamma + \beta$ NiCrAl alloys has been studied. The concentration/distance profiles of all three components, in different alloys and after various oxidation exposures, were measured. It was observed that cyclic oxidation results in a decreasing Al concentration at the oxide/metal interface, non-parabolic growth of the near-surface γ layer, and diffusion path translation. In addition, it was observed that breakaway oxidation occurs when the Al concentration at the oxide/metal interface approaches zero. A numerical model was developed to simulate the diffusional transport of Al during the cyclic oxidation of $\gamma + \beta$ NiCrAl alloys. The numerical model was able to predict accurately the Al concentration profiles, the width of the γ layer, and the weight of Al consumed. Furthermore, the numerical model was shown to predict correctly the onset of breakaway oxidation in the highest Al-containing alloy before that in other alloys.

17. Key Words (Suggested by Author(s))	18. Distribution Statement
Ni-Cr-Al alloys; Al diffusion; Cyclic oxidation; Oxide spalling; Breakaway oxidation	Unclassified - unlimited STAR Category 17

19. Security Classif. (of this report)	20. Security Classif. (of this page)	21. No. of Pages	22. Price*
Unclassified	Unclassified	139	

* For sale by the National Technical Information Service, Springfield, Virginia 22161